

A photograph of an industrial facility at night, featuring a complex network of metal structures, pipes, and walkways. A prominent vertical stack is visible on the left side. The scene is illuminated by various lights, including a bright yellow light on the right and a green light in the background, creating a dramatic, high-contrast atmosphere.

# Novel CCU Approach Integrating $K_2CO_3$ -Based $CO_2$ Capture and Bicarbonate Electrolysis: A Techno-economic Analysis

ME55035: ME/EFPT MSc thesis  
Jonas Vos

Delft University of Technology

# Novel CCU Approach Integrating $K_2CO_3$ -Based $CO_2$ Capture and Bicarbonate Electrolysis: A Techno-economic Analysis

by

Jonas Vos

| Student Name | Student Number |
|--------------|----------------|
| Jonas Vos    | 4596404        |

Thesis supervisors: Dr. R. Kortlever, Prof. Dr. E. Goetheer, Ir. P. van den Broeke  
Daily Supervisor: Ir. I. Burgers  
Faculty: Mechanical Engineering, Process & Energy Department TU Delft

To be defended publicly on Tuesday, November 19, 2024, at 15:00.

# Preface

This thesis represents the culmination of my Master's programme in Mechanical Engineering, within the Energy Flow and Process Technology track at Delft University of Technology. It focuses on an integrated approach to Carbon Capture and Utilization (CCU), combining  $K_2CO_3$ -based carbon capture with bicarbonate electrolysis for syngas production. The research addresses industrial carbon emissions and aims to contribute to the development of sustainable technologies that support a circular carbon economy.

Working on this project has deepened my appreciation for the immense challenges in reducing the carbon footprint of the steel industry. It has also enhanced my understanding of how CCU technologies can contribute to addressing these challenges while highlighting the significant technical and economic hurdles that remain. Achieving carbon-neutral steel production will require a large, sustained research effort. I hope that this thesis, in its modest scope, provides a small but meaningful contribution toward this goal.

I would like to express my gratitude to Dr. Ruud Kortlever for supervising this project. I am confident that, under your leadership, the electrochemistry research group will continue to make significant contributions towards creating a more sustainable future.

I deeply thank Prof. Dr. Earl Goetheer for his guidance during this project. His extensive knowledge and pragmatic, no-nonsense approach helped to clarify and refine my work during critical moments. This guidance enabled me to improve my research, identify a clear direction, and draw meaningful conclusions.

I would like to thank Ir. Peter van den Broeke for his help and guidance during this project. His approachable demeanour greatly supported our collaboration, and his deep technical expertise ensured the work was relevant and impactful for the steel industry in the Netherlands.

I would also like to thank Dr. A. Somoza Tornos for her role in the thesis committee.

I would like to express my gratitude to Asvin Sajeev Kumar and Maria Naharro Vilas for their help and guidance with the ASPEN modelling software.

A special thanks goes to Ir. Iris Burgers for her guidance and mentorship. She challenged me to be more thorough, adopt a critical attitude toward previous research, strive for precision in my work and ultimately become a better academic. The skills and mindset that I have developed under her guidance will undoubtedly benefit me throughout my professional career and personal life.

And last, but most certainly not least, I would like to thank my friends and family. Thank you for always being there for me. I could not have completed this project without your support.

*Jonas Vos  
Amsterdam, November 2024*

# Summary

Rising global CO<sub>2</sub> levels underscore the urgent need for effective carbon capture and utilization (CCU) technologies to support a circular carbon economy. This study evaluates the techno-economic performance of a novel integrated CCU system that combines a K<sub>2</sub>CO<sub>3</sub>-based capture column with a bicarbonate electrolyser for syngas production, specifically targeting applications in the steel industry. An ASPEN PLUS model of the capture column was developed and integrated with a pH-dependent Faradaic Efficiency (FE) model of the electrolyser in Excel. Five cases were defined: (I) 90 wt% CO<sub>2</sub> capture, (II) syngas production with a 2:1 H<sub>2</sub>/CO ratio for the Fischer-Tropsch process, (III) electrolyser operation with FE<sub>CO</sub> > 50%, (IV) syngas composition suited as feedstock for electric arc furnaces (EAF) in the Energiron III process, and (V) an intermediate pH step. A techno-economic analysis (TEA) was conducted across worst, base, and best-case scenarios for each case.

Key findings reveal a trade-off between achieving high FE<sub>CO</sub> at low pH levels and maximizing CO<sub>2</sub> capture efficiency at high pH levels. Systems operating with large pH steps demonstrated a lower Levelized Cost of Syngas normalized to the Lower Heating Value (LCOS<sub>LHV</sub>), due to increased hydrogen output. In contrast, systems with smaller and narrower pH steps incurred higher LCOS<sub>LHV</sub> due to their output's lower LHV. The techno-economic analysis (TEA) indicates that the operational expenditure (OPEX) for the integrated CCU system is currently too high to be cost-competitive with alternative solutions. Sensitivity analysis reveals that the integrated CCU system is competitive with other electrolysis methods only under best-case conditions. Electricity costs and a low CO<sub>2</sub> utilization ratio are identified as the primary drivers of OPEX. Improvements in these areas result in the most significant reduction in LCOS<sub>LHV</sub>, making them critical enablers for the integrated CCU system. Additionally, the cost per kilogram of CO<sub>2</sub> saved is high compared to EU CO<sub>2</sub> Emission Trading System (ETS) prices.

Current bicarbonate electrolysers are more costly than gas-fed CO<sub>2</sub>RR systems in terms of Unit Capital Cost (UCC) per kilogram of CO produced, largely due to reduced performance at higher current densities (>100 mA/cm<sup>2</sup>). Achieving CAPEX parity with gas-fed CO<sub>2</sub>RR systems would require increasing current densities while maintaining high FE<sub>CO</sub> and sustaining these efficiencies at alkaline pH levels.

Future work should prioritize reducing both OPEX and CAPEX for the system, with a particular focus on improving the technical performance of the bicarbonate electrolyser. Key objectives include increasing current density while maintaining high FE<sub>CO</sub> at alkaline pH levels, improving the CO<sub>2</sub> utilization ratio, and enhancing the stability of the electrolyser.

**Keywords:** Carbon Capture and Utilization, Bicarbonate Electrolysis, K<sub>2</sub>CO<sub>3</sub>-based CO<sub>2</sub> Capture, Benfield Process, Integrated CCU System, Techno-economic Analysis

# Contents

|   |             |
|---|-------------|
| <b>Preface</b>  | <b>i</b>    |
| <b>Summary</b>  | <b>ii</b>   |
| <b>List of abbreviations</b>  | <b>viii</b> |
| <b>Symbols</b>  | <b>x</b>    |
| <b>1 Introduction</b>   | <b>1</b>    |
| 1.1 Problem statement . . . . .   | 3           |
| 1.2 Research questions . . . . .  | 4           |
| 1.3 Thesis outline . . . . .  | 4           |
| <b>2 Literature review</b>  | <b>5</b>    |
| 2.1 Electrochemistry: Fundamental equations and concepts . . . . .                                | 5           |
| 2.1.1 CO <sub>2</sub> RR . . . . .  | 7           |
| 2.2 Electrolysers . . . . .   | 8           |
| 2.2.1 Gas-fed electrolysers for CO <sub>2</sub> RR . . . . .                                      | 8           |
| 2.2.2 Bicarbonate electrolyser for CO <sub>2</sub> RR . . . . .                                   | 9           |
| 2.2.3 Design parameters and their effects on bicarbonate electrolysis . . . . .                   | 12          |
| 2.2.4 CO <sub>2</sub> RR for C <sub>2</sub> + products . . . . .                                  | 15          |
| 2.3 Carbon capture . . . . .  | 16          |
| 2.3.1 Flue gas composition . . . . .  | 16          |
| 2.3.2 Benfield process . . . . .  | 16          |
| 2.3.3 Enhancing capture rates in the Benfield process . . . . .                                   | 17          |
| 2.4 Integrating capture and conversion . . . . .  | 18          |
| 2.4.1 Role of pH . . . . .  | 18          |
| 2.4.2 Closing the loop . . . . .  | 19          |
| 2.5 Techno-economic analysis . . . . .  | 20          |
| 2.5.1 TEA for gas-fed CO <sub>2</sub> RR systems . . . . .  | 20          |
| 2.5.2 TEA for bicarbonate electrolyser systems . . . . .  | 21          |
| 2.5.3 Enablers . . . . .  | 22          |
| <b>3 Methodology</b>  | <b>25</b>   |
| 3.1 Scope of research and design cases . . . . .  | 25          |
| 3.1.1 Flue gas feed stream . . . . .  | 25          |
| 3.1.2 Operating conditions . . . . .  | 26          |
| 3.1.3 Reverse water-gas shift . . . . .   | 26          |
| 3.1.4 Cases I, II, III, IV and V . . . . .  | 27          |
| 3.2 Electrolyser model . . . . .  | 28          |
| 3.2.1 Model description . . . . .   | 28          |
| 3.2.2 pH-dependent model inputs: FE <sub>CO</sub> and CO <sub>2</sub> utilization ratio . . . . . | 29          |
| 3.2.3 pH-step dependent model input HCO <sub>3</sub> <sup>-</sup> conversion . . . . .            | 30          |
| 3.2.4 Model constants . . . . .   | 31          |
| 3.3 Rate-based model for capture column . . . . .   | 31          |
| 3.3.1 Equilibrium vs. rate-based model . . . . .  | 32          |
| 3.3.2 Capture column design parameters . . . . .  | 32          |
| 3.3.3 ASPEN model validation . . . . .  | 32          |
| 3.4 Recycle streams . . . . .   | 32          |
| 3.5 Cost estimation . . . . .   | 33          |
| 3.5.1 OPEX . . . . .  | 33          |

|          |   |           |
|----------|---|-----------|
| 3.5.2    | Levelized Cost of Syngas (LCOS) normalized to Lower Heating Value (LHV) . . . | 33        |
| 3.5.3    | CAPEX . . . . .   | 34        |
| 3.6      | CO <sub>2</sub> emissions . . . . .   | 36        |
| 3.6.1    | CO <sub>2</sub> captured by the system . . . . .                              | 36        |
| 3.6.2    | CO <sub>2</sub> emissions resulting from energy production . . . . .          | 36        |
| 3.7      | Sensitivity Analysis . . . . .  | 37        |
| <b>4</b> | <b>Results &amp; Discussion</b>   | <b>38</b> |
| 4.1      | pH steps and capture fractions . . . . .                                      | 38        |
| 4.2      | OPEX analysis . . . . .   | 39        |
| 4.2.1    | LCOS <sub>LHV</sub> comparison . . . . .                                      | 39        |
| 4.2.2    | Sankey plot for OPEX distribution . . . . .                                   | 40        |
| 4.2.3    | Bridge plot for LCOS <sub>LHV</sub> . . . . .                                 | 43        |
| 4.2.4    | Cost of CO <sub>2</sub> savings . . . . .                                     | 44        |
| 4.3      | CAPEX Analysis . . . . .  | 45        |
| 4.3.1    | UCC comparison to H <sub>2</sub> electrolyzers . . . . .                      | 45        |
| 4.3.2    | UCC comparison to CO <sub>2</sub> RR electrolyzers . . . . .                  | 46        |
| 4.3.3    | UCC for increased current density . . . . .                                   | 47        |
| <b>5</b> | <b>Conclusion &amp; Recommendations</b>                                       | <b>49</b> |
|          | <b>References</b>   | <b>52</b> |
| <b>A</b> | <b>Appendix</b>   | <b>59</b> |
| A.1      | DRI processes . . . . .   | 60        |
| A.2      | Economic analysis of product pathways . . . . .                               | 61        |
| A.3      | Overview of cases . . . . .   | 62        |
| A.4      | Electrolyser model inputs . . . . .   | 64        |
| A.4.1    | Bjerrum plot . . . . .  | 64        |
| A.4.2    | Inputs for ambient conditions (1 bar, 20°C) . . . . .                         | 65        |
| A.4.3    | Inputs for operating conditions (10 bar, 60°C) . . . . .                      | 65        |
| A.5      | Electrolyser model . . . . .  | 67        |
| A.5.1    | Model constants . . . . .   | 67        |
| A.5.2    | Formulas used in electrolyser model . . . . .                                 | 67        |
| A.6      | ASPEN Model for absorption column . . . . .                                   | 67        |
| A.6.1    | Component list . . . . .  | 68        |
| A.6.2    | Reactions and reaction constants . . . . .                                    | 68        |
| A.6.3    | Capture fractions chart for CAPSOL process . . . . .                          | 69        |
| A.6.4    | Iteration and optimization . . . . .  | 69        |
| A.7      | Formulas for estimating CAPEX . . . . .                                       | 70        |
| A.7.1    | Electrolyser CAPEX estimation . . . . .                                       | 70        |
| A.7.2    | Calculation of catalyst costs . . . . .                                       | 70        |
| A.8      | Formulas for estimating yearly OPEX . . . . .                                 | 71        |
| <b>B</b> | <b>Appendix results</b>   | <b>72</b> |
| B.1      | pH steps required for the cases . . . . .                                     | 72        |
| B.2      | Literature data for competing compounds and production methods . . . . .      | 73        |
| B.3      | Additional LCOS analysis . . . . .  | 73        |
| B.4      | Sankey plots Case I and IV . . . . .  | 74        |
| B.5      | Brigdeplots Case I, III, IV and V . . . . .                                   | 75        |
| B.6      | OPEX per kg CO <sub>2</sub> for 50%/50% solar wind mix . . . . .              | 78        |
| B.7      | CAPEX per t CO produced . . . . .   | 79        |
| B.8      | CAPEX distribution among equipment . . . . .                                  | 80        |
| <b>C</b> | <b>Python code</b>  | <b>81</b> |
| C.1      | Python code for Bjerrum plot . . . . .  | 81        |

# List of Figures

|      |  |    |
|------|--|----|
| 1.1  | Schematic overview of gas-fed CO <sub>2</sub> electrolysis vs. bicarbonate electrolysis [23]. . . . .  | 3  |
| 2.1  | Schematic view of the bicarbonate flow cell. Correction on this figure: no KOH is consumed in the anode reaction; only water in the form of OH <sup>-</sup> supplied by the BPM is consumed in the OER [21]. . . . .   | 10 |
| 2.2  | Plot of experimental results of FE <sub>CO</sub> vs. current density at pressures 1-4 atm [66]. . . . .  | 12 |
| 2.3  | Plot of experimental results of FE <sub>CO</sub> vs. KHCO <sub>3</sub> temperature [66]. . . . .   | 13 |
| 2.4  | The thermodynamic equilibrium of (bi)carbonates and CO <sub>2</sub> in aqueous media (Bjerrum plot). Mole fractions for CO <sub>2</sub> (aq), HCO <sub>3</sub> <sup>-</sup> (aq), and CO <sub>3</sub> <sup>2-</sup> (aq) as a function of pH at ambient conditions (temperature = 25 °C; pressure = 1 atm) [15]. . . . .           | 13 |
| 2.5  | pH within the bicarbonate electrolyser cathode compartment for different applied current densities [67]. . . . .   | 14 |
| 2.6  | pH profile at 0 μm (left), 64 μm (middle), and 135 μm (right) spacing at the applied current densities from 200 to 350 mA/cm <sup>2</sup> in 1,5 M K <sub>2</sub> CO <sub>3</sub> electrolyte [71]. . . . .  | 15 |
| 2.7  | Residence time vs. absorption column temperature for Benfield process [82]. . . . .  | 17 |
| 2.8  | Schematic overview of favoured pH steps in the integrated CCU process. . . . .   | 19 |
| 2.9  | Illustration of solvent circulation showing reduced capture efficiency as pH increases [89].   | 19 |
| 2.10 | FE vs. overpotential with colour gradient indicating NPV: the black line indicates an NPV of zero [29]. . . . .  | 21 |
| 2.11 | Levelized production of syngas for rWGS, Gas-E and Carb-E [93]. . . . .  | 22 |
| 2.12 | Bridge plot indicating the effects of improved performance and economic factors on production costs of ethylene [91]. . . . .  | 23 |
| 2.13 | Carbon footprint of the three pathways to renewable syngas from DAC in the base case (light grey) and best case scenario (dark grey)[93]. . . . .  | 24 |
| 3.1  | Schematic overview of the system: scope of thesis indicated by orange dotted line. . . . .   | 25 |
| 3.2  | Schematic overview of the electrolyser model with inputs and outputs. . . . .  | 28 |
| 3.3  | a) FE <sub>CO</sub> over time, b) CO <sub>2</sub> :CO ratio over time, c) CO <sub>2</sub> concentration in the gas compartment over time, d) CO <sub>2</sub> utilization ratio for 4 pH levels [98]. . . . .   | 29 |
| 3.4  | Bjerrum plot for ambient conditions (1 bar, 25°C) and system conditions (10 bar, 60°C). . . . .  | 31 |
| 4.1  | Visualization of pH steps and CO <sub>2</sub> capture fraction (wt%) required for achieving the base case design goals. The point on the left represents the pH of the electrolyser inflow/absorption column outflow, while the point on the right represents the pH of the electrolyser outflow/absorption column inflow. . . . . | 38 |
| 4.2  | LCOS <sub>LHV</sub> for various cases, including Power-to-Gas (P-t-G), reverse Water-Gas Shift (rWGS), gas-fed (CO <sub>2</sub> RR), bicarbonate electrolysis (Carb-E), and H <sub>2</sub> electrolysis powered by either grid electricity (E-Grid) or renewable electricity (E-Ren) [110, 111, 93, 112].                          | 39 |
| 4.3  | Sankey diagram showing OPEX distribution for Case II (Base Scenario): pH step 8,5 ↔ 11,3. Total OPEX \$20,5 million/year. . . . .  | 41 |
| 4.4  | Sankey diagram showing OPEX distribution for Case III (Base Scenario): pH step 8,5 ↔ 9,3. Total OPEX: \$61,8 million/year. . . . .   | 41 |
| 4.5  | Sankey diagram showing OPEX distribution for Case V (Base Scenario): pH step 9,0 ↔ 10,5. Total OPEX: \$21,0 million/year. . . . .  | 42 |
| 4.6  | Bridge plot showing LCOS <sub>LHV</sub> for Case II (base → best). . . . .   | 43 |
| 4.7  | OPEX per kg CO <sub>2</sub> not emitted (energy source: 100% wind). . . . .  | 44 |
| 4.8  | Unit Capital Cost (UCC) comparison of electrolysers: TNO [106], Berenschot & TNO [104], EU Hydrogen Observatory [107], Wood Mackenzie [108], CE Delft & TNO [109]. . . . .   | 46 |

|      |  |    |
|------|--|----|
| 4.9  | Comparison of UCC per tonne of CO with literature data on CO <sub>2</sub> RR electrolyzers. Data from Moreno et al. represents the base case, while for data from Jouny et al., the left bar represents the base case and the right bar represents the best case [93, 29]. . . . . | 47 |
| 4.10 | Effect of varying CD on UCC in the best-case scenarios for cases II and III. Data from Moreno et al. represents the base case, while for data from Jouny et al., the left bar represents the base case and the right bar represents the best case [93, 29]. . . . .                | 48 |
| A.1  | Simplified process configuration for Midrex process [27]. . . . .  | 60 |
| A.2  | Simplified process configuration for Energiron III process [27]. . . . .   | 60 |
| A.3  | Overview of products pathways for CO <sub>2</sub> RR [116]. . . . .  | 61 |
| A.4  | Schematic overview of Case I: design for 90wt% capture in the absorption column. . . . .   | 62 |
| A.5  | Schematic overview of Case II: Design for syngas fit for FT-process. . . . .   | 62 |
| A.6  | Schematic overview of Case III: design for FE > 50%. . . . .   | 63 |
| A.7  | schematic overview of Case IV: design syngas fit for EAF. . . . .  | 63 |
| A.8  | Schematic overview of Case V: mid-pH step. . . . .   | 63 |
| A.9  | Data on CAPSOI process: Absorption column height versus CO <sub>2</sub> fraction, used for model validation. . . . .   | 69 |
| B.1  | LCOS for syngas (non-levelized for LHV). . . . .   | 73 |
| B.2  | OPEX per kg CO product . . . . .   | 74 |
| B.3  | Sankey diagram showing OPEX distribution for Case I (Base Scenario): pH step 9.0 ↔ 11.5. Total OPEX: \$18,8 million/year. . . . .  | 74 |
| B.4  | Sankey diagram showing OPEX distribution for Case IV (Base Scenario): pH step 8.5 ↔ 11.5. Total OPEX: \$21,4 million/year. . . . .   | 75 |
| B.5  | Bridge plot showing LCOS <sub>LHV</sub> for case I (base → best). . . . .  | 75 |
| B.6  | Bridge plot showing LCOS <sub>LHV</sub> for case III (base → best). . . . .  | 76 |
| B.7  | Bridge plot showing LCOS <sub>LHV</sub> for case IV (base → best). . . . .   | 76 |
| B.8  | Bridge plot showing LCOS <sub>LHV</sub> for case V (base → best). . . . .  | 77 |
| B.9  | OPEX per kg CO <sub>2</sub> not emitted (energy source: 50%/50% wind solar mix). . . . .   | 78 |
| B.10 | CAPEX per ton of CO product per year for the five cases. . . . .   | 79 |
| B.11 | CAPEX distribution among equipment presented as a 100% stacked bar chart for the base case scenario. The fraction of CAPEX allocated to the pump is negligible. . . . .  | 80 |

# List of Tables

|      |   |    |
|------|---|----|
| 2.1  | Compilation of Experimental Data of CO <sub>2</sub> Reduction to CO in gas-fed CO <sub>2</sub> electrolyzers. (N.S.: Not Specified).  | 9  |
| 2.2  | Experimental results for bicarbonate electrolyzers.   | 11 |
| 3.1  | Data for flue gas from Energiron III process stream 26 [27].  | 26 |
| 3.2  | Data for Stream 17: feed stream for EAF in Energiron III process [27].  | 28 |
| 3.3  | Multiplication factors for estimating input parameters at elevated temperatures and pressures (10 bar, 60°C).   | 30 |
| 3.4  | Syngas mole ratio H <sub>2</sub> /CO, corresponding weight ratio, and LHV.  | 34 |
| 3.5  | Comparison of UCC (USD) across different studies for H <sub>2</sub> electrolyzers (Euro converted to USD).  | 35 |
| 3.6  | Comparison data of UCC per ton of CO for bicarbonate and gas-fed electrolyzers.   | 35 |
| 3.7  | IPCC data on CO <sub>2</sub> emissions from different energy sources [29].  | 36 |
| 3.8  | Technical parameters used in sensitivity analysis.  | 37 |
| 3.9  | Economical parameters used in sensitivity analysis.   | 37 |
| A.1  | CO <sub>2</sub> RR Products Data [29]   | 61 |
| A.2  | Overview of input and output parameters with descriptions and units.  | 64 |
| A.3  | pKa values for the dissociation of carbonic acid and bicarbonate under different temperature and pressure conditions.   | 64 |
| A.4  | Mole fractions of HCO <sub>3</sub> <sup>-</sup> and CO <sub>3</sub> <sup>2-</sup> , FE <sub>CO</sub> , and CO <sub>2</sub> utilization at different pH levels.                    | 65 |
| A.5  | Model inputs ambient: Conversion of HCO <sub>3</sub> <sup>-</sup> , FE <sub>CO</sub> , and CO <sub>2</sub> utilization across different pH steps under ambient conditions.        | 65 |
| A.6  | Worst case: pH, mole fractions of HCO <sub>3</sub> <sup>-</sup> and CO <sub>3</sub> <sup>2-</sup> , FE <sub>CO</sub> , and CO <sub>2</sub> utilization percentages.               | 65 |
| A.7  | Model inputs Worst case: Steps, Conversion of HCO <sub>3</sub> <sup>-</sup> , FE <sub>CO</sub> , and CO <sub>2</sub> utilization percentages.                                     | 65 |
| A.8  | Base case: pH, mole fractions of HCO <sub>3</sub> <sup>-</sup> and CO <sub>3</sub> <sup>2-</sup> , FE <sub>CO</sub> , and CO <sub>2</sub> utilization percentages.                | 66 |
| A.9  | Model inputs Base case: Steps, Conversion of HCO <sub>3</sub> <sup>-</sup> , FE <sub>CO</sub> , and CO <sub>2</sub> utilization percentages.                                      | 66 |
| A.10 | Best case: pH, mole fractions of HCO <sub>3</sub> <sup>-</sup> and CO <sub>3</sub> <sup>2-</sup> , FE <sub>CO</sub> , and CO <sub>2</sub> utilization percentages.                | 66 |
| A.11 | Model inputs Best case: Steps, Conversion of HCO <sub>3</sub> <sup>-</sup> , FE <sub>CO</sub> , and CO <sub>2</sub> utilization percentages.                                      | 66 |
| A.12 | Table of Physical Constants and Other Values.   | 67 |
| A.13 | Formulas used in the electrolyser model.  | 67 |
| A.14 | Chemical compounds and their respective CAS numbers as used in ASPEN PLUS. Note: Ions do not have CAS numbers as they are derived from other compounds and are context-dependent. | 68 |
| A.15 | Equilibrium reactions and their corresponding parameters.   | 68 |
| A.16 | Kinetic reactions and their corresponding rate constants and activation energies.   | 68 |
| A.17 | Breakdown of CAPEX for the Electrolyser in USD.   | 70 |
| A.18 | Summary of Catalyst and Material Costs [93].  | 70 |
| A.19 | Operational Expenditure (OPEX) Parameters.  | 71 |
| B.1  | Overview of pH Ranges for Different Cases (Rounded to 1 Decimal Place).   | 72 |
| B.2  | Production costs and LCOS adjusted for LHV for various compounds and production methods.  | 73 |

# Nomenclature

| Abbreviation       | Definition                                |
|--------------------|---|
| AEA                | Aspen Economic Analyzer                   |
| BPM                | Bipolar Membrane                          |
| BoP                | Balance of Plant                          |
| CAPEX              | Capital Expenditure                       |
| CO <sub>2</sub> RR | CO <sub>2</sub> Reduction Reaction        |
| CC                 | Carbon Capture                            |
| CCS                | Carbon Capture and Storage                |
| CCU                | Carbon Capture and Utilization            |
| CD                 | Current Density                           |
| CEPCI              | Chemical Engineering Plant Cost Index     |
| Carb-E             | (Bi)Carbonate Electrolysis                |
| DAC                | Direct Air Capture                        |
| DBD                | Declining Balance Depreciation            |
| DRI                | Direct Reduction of Iron                  |
| EAF                | Electric Arc Furnace                      |
| ETS                | Emissions Trading System                  |
| EE                 | Energy Efficiency                         |
| FE                 | Faradaic Efficiency                       |
| FT                 | Fischer-Tropsch Process                   |
| G/L-ratio          | Gas-to-Liquid Ratio                       |
| Gas-E              | Gas-fed CO <sub>2</sub> Electrolysis      |
| HER                | Hydrogen Evolution Reaction               |
| HPC                | Hot Potassium Carbonate                   |
| IPCC               | Intergovernmental Panel on Climate Change |
| IR                 | Interest Rate                             |
| ISA                | International Standard Atmosphere         |
| LCOS               | Levelized Cost of Syngas                  |
| LHV                | Lower Heating Value                       |
| LCA                | Life Cycle Assessment                     |
| MEA                | Membrane Electrode Assembly               |
| NPV                | Net Present Value                         |
| OER                | Oxygen Evolution Reaction                 |
| OPEX               | Operational Expenditure                   |
| OPEX <sub>RM</sub> | Raw Material OPEX                         |
| OPEX <sub>E</sub>  | Electrolyser Electricity OPEX             |
| OPEX <sub>U</sub>  | Utility OPEX                              |
| OPEX <sub>CM</sub> | Consumable OPEX                           |
| OPEX <sub>FC</sub> | Fixed OPEX                                |
| OPEX <sub>IC</sub> | Investment-Related OPEX                   |
| PEM                | Proton Exchange Membrane                  |
| RES                | Renewable Energy Sources                  |
| Redox              | reduction-oxidation                       |
| rWGS               | Reverse Water-Gas Shift                   |
| SMR                | Steam Methane Reforming                   |
| SOEC               | Solid Oxide Electrolysis Cell             |
| TEA                | Techno-Economic Analysis                  |

---

| <b>Abbreviation</b> | <b>Definition</b>                                     |
|---------------------|---|
| UCC                 | Unit Capital Cost                                     |
| UNFCCC              | United Nations Framework Convention on Climate Change |

---

# Symbols

| Symbol                    | Name   | Unit   |
|---------------------------|--|--|
| $A$                       | Area   | $m^2$  |
| $A_{\text{electrolyser}}$ | Required electrolyser area   | $m^2$  |
| $\Delta H$                | Enthalpy change  | $\text{kJ/mol}$                                  |
| $E_{eq}$                  | Equilibrium potential  | V  |
| $e$                       | Electron charge  | C  |
| $F$                       | Faraday's constant   | $\text{A}\cdot\text{s/mol}$                      |
| $FE_{\text{CO}}$          | Faradaic efficiency for CO production                                | %  |
| $FE_{\text{H}_2}$         | Faradaic efficiency for $\text{H}_2$ production                      | %  |
| $I_{\text{tot}}$          | Total electrical current   | A  |
| $i$                       | Current  | A  |
| $i_m$                     | Yearly average rate of return if money was not invested in the plant | %  |
| $j$                       | Current density  | $\text{mA/cm}^2$                                 |
| $j_0$                     | Exchange current density   | $\text{mA/cm}^2$                                 |
| $m$                       | Number of moles of product   | mol  |
| $n$                       | Number of electrons transferred                                      | -  |
| $P$                       | Power consumption  | W  |
| $pK_a$                    | Acid dissociation constant   | -  |
| $q$                       | Total charge passed  | C  |
| $R$                       | Gas constant   | $\text{J}\cdot\text{K}^{-1}\cdot\text{mol}^{-1}$ |
| $R$                       | Resistance   | $\Omega$   |
| $T$                       | Temperature  | K or $^{\circ}\text{C}$                          |
| $V$                       | Potential difference   | V  |

| Greek Symbol | Name                        | Unit            |
|--------------|-----------------------------|-----------------|
| $\alpha$     | Charge transfer coefficient | -               |
| $\eta$       | Overpotential               | V               |
| $\rho$       | Density                     | $\text{kg/m}^3$ |

# 1

## Introduction

### Climate change, the Paris Climate Agreement and CO<sub>2</sub> emissions

In recent decades, the increase of CO<sub>2</sub> concentrations in the atmosphere has been correlated with rising global temperatures, escalating sea levels, and heightened occurrences of extreme weather events [1, 2]. This trend has sparked global efforts aimed at reducing CO<sub>2</sub> concentrations, captured notably by the Paris Climate Agreement of 2015. This agreement aims to limit the increase in global average temperature to below 2°C above pre-industrial levels by the year 2100 and to pursue efforts to limit the temperature increase even further to 1,5°C [3]. Achieving these goals requires significant reductions in greenhouse gas emissions worldwide. Specifically, the United Nations Framework Convention on Climate Change (UNFCCC) estimated that reducing global CO<sub>2</sub> emissions by 43% by the year 2030 is necessary to stay on track with the objectives set forth by the Paris Agreement [4].

Certain industries, notably the steel and chemical industry, stand out as significant contributors to CO<sub>2</sub> emissions due to their reliance on carbon-intensive processes. Aside from regulatory efforts aimed at emission reduction, the steel industry faces increasing societal pressure, given its estimated responsibility for 7% of global CO<sub>2</sub> emissions [5, 6]. In addition, the chemical sector is estimated to account for 3% of global CO<sub>2</sub> emissions, primarily due to the consumption of large amounts of energy produced with fossil fuels and fossil-based feedstocks [7]. As demand for products from the steel and chemical industries continues to rise, and carbon-neutral production methods have not yet been implemented on a large scale, reducing CO<sub>2</sub> emissions in these sectors is essential to achieving the CO<sub>2</sub> reduction goals outlined in the Paris Climate Agreement [8].

### Carbon capture, storage and utilization

Carbon capture (CC) can serve as a solution to prevent industrial CO<sub>2</sub> emissions from reaching the atmosphere. CC aims to isolate CO<sub>2</sub> from flue gases (post-combustion), with common methods including absorption, adsorption and membrane gas separation [9]. Absorption solvents, such as amines, ammonia or carbonate salts chemically bind to CO<sub>2</sub> from flue gases, while other compounds in the flue gas do not. The CO<sub>2</sub>-rich solvent is then separated from the flue gas stream, and fed into a desorption column, where the CO<sub>2</sub> is released from the solvent by heating. This yields purified gas phase CO<sub>2</sub>, and CO<sub>2</sub> lean solvent, which can be reused in the absorption column. Adsorption works similarly but instead of the CO<sub>2</sub> chemically binding to a solvent, it binds on the surface of materials such as zeolites or activated carbon. These materials selectively adsorb CO<sub>2</sub> at lower temperatures and release it at higher temperatures. Membrane gas separation uses semi-permeable membranes that allow CO<sub>2</sub> to pass through more readily than other flue gases, thus having the ability to isolate gas phase CO<sub>2</sub>. Alternative processes for CC using microalgae exist but are rarely employed in industrial processes [10].

After CC, the isolated CO<sub>2</sub> needs to be processed further. The two prevailing methods for processing captured CO<sub>2</sub> are Carbon Capture and Storage (CCS) and Carbon Capture and Utilization (CCU). CCS involves capturing CO<sub>2</sub> from flue gases and transporting them to permanent geological storage sites, such as depleted gas fields or underground cavities. This method has been proven to reduce CO<sub>2</sub> emis-

sions effectively but faces societal concerns about storage safety, site availability, and environmental impact. Additionally, CCS is an intermediate solution, aiding the transition to fully CO<sub>2</sub>-neutral energy production rather than providing a permanent fix for CO<sub>2</sub> emissions. Conversely, CCU aims to reduce industrial CO<sub>2</sub> emissions by capturing it at a point source, usually a CO<sub>2</sub>-containing flue gas stream, and then reusing it in chemical processes. One way of doing so is using electrolysis to convert CO<sub>2</sub> into in-demand feedstock, such as syngas, CO, ethylene, or ethanol, through CO<sub>2</sub> reduction reactions (CO<sub>2</sub>RR). This method offers a potentially more sustainable solution by avoiding the release of inert CO<sub>2</sub> into the atmosphere while producing chemicals that would otherwise require energy-intensive or CO<sub>2</sub>-emitting processes.

Aside from preventing CO<sub>2</sub> emissions into the atmosphere, CCU with CO<sub>2</sub>RR has additional benefits. One of them is its ability to channel the surplus energy of renewable energy sources (RES) by employing electrolysis. These sources generate electricity from sunlight or wind, with their output depending on the availability of these elements, leading to fluctuations in energy production. Consequently, this intermittency may lead to shortages during periods of low generation and surpluses during peak periods. CCU with CO<sub>2</sub>RR can address this issue by storing surplus energy from RES in stable, higher-energy compounds produced from CO<sub>2</sub> flue gases, thereby acting as a large-scale energy storage solution.

In addition, CCU with CO<sub>2</sub>RR has the potential for economic viability as its products can be used on-site by industrial CO<sub>2</sub> emitters or sold for a profit. This aspect could make it economically feasible for industry players to incorporate this technology [11]. The steel industry presents a potential starting point for the implementation of CCU with CO<sub>2</sub>RR, given the presence of large amounts of CO<sub>2</sub> from a point source, its use of CO<sub>2</sub>RR products and its substantial contribution to global CO<sub>2</sub> emissions.

#### CO<sub>2</sub>-fed processes for CCU with CO<sub>2</sub>RR

The state-of-the-art processes for CCU with CO<sub>2</sub>RR employ a gas-fed CO<sub>2</sub> electrolyser. This works in the following way: A potential is applied on the electrodes and purified CO<sub>2</sub> is reacted at the catalytic cathode producing higher-value C molecules. Simultaneously, water is oxidized at the anode compartment, producing oxygen gas. Situated between these compartments is typically a membrane that prevents the mixing of products and reactants, while allowing selective ion transport [12]. Various cell configurations exist, including H-cells, Proton Exchange Membrane (PEM) cells with Membrane Electrode Assemblies (MEA), or Solid Oxide Electrolysis Cells (SOEC) [13]. Despite their differences, these cells share a common feature: They operate using purified gaseous CO<sub>2</sub> as the feedstock.

To obtain this feedstream from industrial flue gases, CO<sub>2</sub> must be isolated, typically through absorption. CO<sub>2</sub> is captured in an absorber column where it is chemically absorbed by a solvent. Common solvents are amine-based solutions, ammonia, or carbonate salts, each with its advantages and disadvantages. Subsequently, the CO<sub>2</sub>-rich solvent is transferred to a desorption (stripper) column where it is heated, and the CO<sub>2</sub> is released from the solvent. The gas-phase CO<sub>2</sub> leaves the desorption column at low or ambient pressure, after which it must be pumped through the system, requiring a compression step. Both steps are energy-intensive: the desorption step requires significant heating of the CO<sub>2</sub>-rich solvent and the compression step also consumes energy [14, 15]. Additionally, the gaseous CO<sub>2</sub> can pass the electrolyser compartment unreacted, leaving a significant percentage of CO<sub>2</sub> unreacted [16, 17, 18]. Furthermore, a notable amount of CO<sub>2</sub> is lost due to the carbonate formation reaction, which competes with the CO<sub>2</sub>RR and decreases electrolyser performance [19].

#### Novel integrated CCU with CO<sub>2</sub>RR process

In the search for a process design that improves the performance of CO<sub>2</sub>RR, a novel process has been gaining attention in recent years. Instead of using a pure CO<sub>2</sub> gas-fed electrolyser, a bicarbonate electrolyser with a bipolar membrane (BPM) and a MEA is used. This setup is fed by a liquid phase bicarbonate (HCO<sub>3</sub><sup>-</sup>) feedstream. Through several reactions occurring on the BPM surface and in the cathode compartment, the HCO<sub>3</sub><sup>-</sup> forms aqueous CO<sub>2</sub> *in situ* (i-CO<sub>2</sub>), which is then directly supplied to the catalytic electrode. Here, carbon products are synthesized through the CO<sub>2</sub>RR reactions [20]. To achieve the HCO<sub>3</sub><sup>-</sup> feedstock, a potassium carbonate solvent (K<sub>2</sub>CO<sub>3</sub>) has to be used as solvent in the absorption column. The gaseous CO<sub>2</sub> reacts with the CO<sub>3</sub><sup>2-</sup> ions and forms HCO<sub>3</sub><sup>-</sup>, which can be fed directly into the bicarbonate electrolyser. The primary advantage is that this system can deliver significantly higher CO<sub>2</sub> concentrations near the catalyst compared to systems relying on dissolved CO<sub>2</sub> [21, 14]. Additionally, this process offers several other benefits: it bypasses the energy-intensive

CO<sub>2</sub> desorption and compression steps, as the liquid-phase feedstock can be introduced under ambient conditions. It theoretically enables a truly integrated process since the CO<sub>2</sub>-rich solvent can be fed directly to the electrolyser, and the catholyte can be recycled into the absorption column [15]. In addition, it counters the problem of CO<sub>2</sub>-loss due to carbonate formation that is inherent to gas-fed CO<sub>2</sub> electrolyzers [22]. A simplified overview of both the state-of-the-art gas-fed CO<sub>2</sub>RR system and the novel bicarbonate process, is displayed in Figure 1.1.

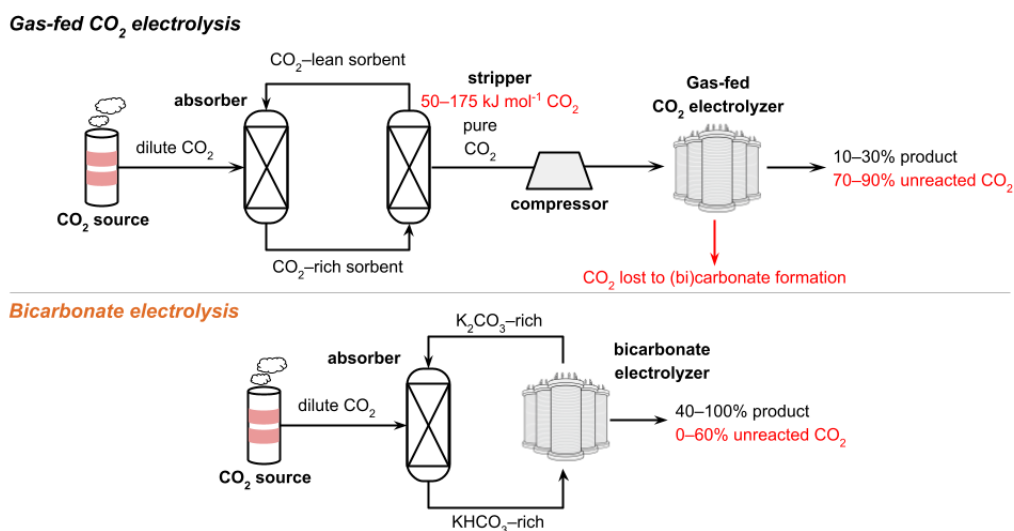


Figure 1.1: Schematic overview of gas-fed CO<sub>2</sub> electrolysis vs. bicarbonate electrolysis [23].

## 1.1. Problem statement

In recent years, the research group from the University of British Columbia led by Curtis P. Berlinguette has gained recognition for its pioneering work in CCU with CO<sub>2</sub>RR. Accordingly, the Berlinguette research group has been at the forefront of advancements in bicarbonate electrolysis technology. However, in their research, the electrolyser primarily operates as a stand-alone system and is conducted on a laboratory scale. Their work involves integrating the CO<sub>2</sub> capture process by passing a purified CO<sub>2</sub> gas stream through an absorption column fed with K<sub>2</sub>CO<sub>3</sub> solvent, but research towards scaling up and designing a flue-gas-to-product process has yet to be conducted [24]. They advocate for further research on an industrial scale and the development of models that represent the full system for integrated CCU with CO<sub>2</sub>RR, including upstream and downstream process steps. These models can be compared to the current gas-fed processes for CO<sub>2</sub>RR to assess which one shows better results. Additionally, the Berlinguette group emphasizes the need to consider techno-economic factors. To transition from laboratory to pilot scale, having positive economic projections is essential to attract investment and facilitate the implementation and commercialization of the technology. Therefore, ongoing research should focus on conducting economic analyses to investigate the feasibility and scalability of bicarbonate electrolysis technologies.

Aside from the fundamental economics of an industrial-scale process, implementation in specific cases should be considered. Barecka et al. researched retrofitting current industrial processes with gas-fed CO<sub>2</sub> electrolyzers [25]. Techno-economic analysis (TEA) of these systems resulted in significant cost reductions across a range of production plants when integrating gas-fed CO<sub>2</sub> electrolyzers, especially when carbon taxes are employed. However, research into the integration of bicarbonate electrolyzers in existing plants, as well as their economic implications, is lacking.

The need for innovative and economically feasible CO<sub>2</sub> mitigation methods, such as CCU with CO<sub>2</sub>RR, is particularly high in the steel industry. Currently, new steelmaking processes are transitioning away from coal-based methods to less carbon-intensive alternatives. Many industry players are initially adopting the Direct Reduction of Iron (DRI) process before transitioning to fully carbon-neutral steelmaking using H<sub>2</sub> as feedstock [26]. The DRI process currently operates on natural gas and still causes CO<sub>2</sub>

emissions [27]. Given the previous investments in coal-based processes and the present CO<sub>2</sub> emissions in DRI processes, it is projected that the steel industry will continue to be a significant CO<sub>2</sub> emitter in the coming decades, underscoring the need for CCU solutions [28]. Furthermore, CO<sub>2</sub>RR products, primarily syngas and oxygen, can be directly utilized at steelmaking sites. This integration not only aids in reducing CO<sub>2</sub> emissions but could also decrease the costs associated with current steel production processes. The projected CO<sub>2</sub> emissions and the potential for integration highlight why research into the implementation of CCU with CO<sub>2</sub>RR in the steelmaking industry should be prioritized.

This thesis is initiated in response to the identified research needs, aiming to explore and model an integrated CCU process capable of efficient operation at a larger scale. The research will focus on the technological and economic viability, as well as the implementation in industry, of integrated bicarbonate electrolyser systems. The findings will be tailored to the steel industry, which has significant potential for the implementation of novel CO<sub>2</sub>RR methods. The research questions, detailed in section 1.2, are designed to address these areas.

## 1.2. Research questions

This thesis aims to answer the research questions stated below.

**Research Question:** What is the techno-economic performance of an integrated CCU system with CO<sub>2</sub>RR for syngas production in the steel industry?

### Sub-questions:

1. What is the levelized cost of syngas under different relevant scenarios for the integrated CCU-CO<sub>2</sub>RR system?
2. What are the OPEX and CAPEX of the integrated CCU-CO<sub>2</sub>RR process for syngas production, and how does its techno-economic performance compare to alternative technologies?
3. What are the key factors that enable the implementation of integrated electrochemical CO<sub>2</sub> reduction in the steel industry?
4. What are the potential CO<sub>2</sub> savings for relevant cases of the integrated system, and how do these savings relate to costs?

## 1.3. Thesis outline

This thesis is structured as follows: A review of the literature on CO<sub>2</sub>RR, bicarbonate electrolysers, carbon capture, the integrated process, and recent advancements in TEA for CO<sub>2</sub>RR systems is provided in chapter 2. The methods employed in generating the results are outlined in chapter 3. The findings and their interpretations are presented in chapter 4, and chapter 5 addresses the research questions and offers recommendations for future research.

# 2

## Literature review

Chapter 2 presents a literature review that covers the fundamentals of electrochemistry, gas-fed CO<sub>2</sub> electrolyzers, novel bicarbonate electrolyser processes and architectures, carbon capture, the integrated CCU process, and recent work on TEA for CO<sub>2</sub>RR systems.

### 2.1. Electrochemistry: Fundamental equations and concepts

Electrochemistry is the study of chemical processes that involve the movement of electrons, primarily through redox (reduction-oxidation) reactions that occur at the interface between an electrode and an electrolyte. When a voltage is applied across electrodes immersed in an electrolyte, it drives electrons from the anode to the cathode, facilitating chemical reactions at each electrode. The CO<sub>2</sub>RR occurs at the cathode, while water oxidation reactions take place at the anode. In this section, the theory and fundamental equations of electrochemistry are discussed. In addition, key concepts in electrolysis are elaborated on.

#### Faradaic Efficiency

The Faradaic Efficiency (FE) is defined by equation Equation 2.1, where  $n$  represents the number of electrons consumed in the formation of the product,  $m$  is the number of moles of the product,  $F$  denotes Faraday's constant, and  $q$  is the total charge passed. In other words, the FE of a given product reflects the selectivity of the electrochemical reaction in reducing CO<sub>2</sub> to that product [29]. A high FE<sub>product</sub> indicates that a high percentage of the electrons are utilized in forming the desired product.

$$FE = \frac{mnF}{q} \times 100\% \quad (2.1)$$

#### Current density

Current density (CD) denotes the flow of electric charge per unit area in the conductor. This is defined with current  $I$  flowing through a conducting medium divided by the cross-sectional area of the conductor. Typical units are amperes per square meter ( $A m^{-2}$ ) and milliamperes per square centimeter ( $mA cm^{-2}$ ). The CD is a vital parameter because it denotes the amount of electrons that can be provided to the reaction. This can be used in estimating electrolyser sizing and electricity consumption as CD represents the overall reaction rate [30, 31].

#### Overpotential

In electrochemistry, overpotential ( $\eta$ ) denotes the difference between the theoretically determined reduction potential based on thermodynamics and the actual potential required for the reduction reaction to occur. Although overpotential can have multiple causes, it can be divided into two classes: activation overpotential and concentration overpotential. The former denotes the additional potential necessary to overcome the energy barrier for the redox reaction to occur, while the latter denotes the extra potential needed to overcome mass transfer limitations [32]. A low overpotential is required for high energy efficiency, see Equation 2.3.

### Ohmic Losses

Ohmic losses, also known as the ohmic drop, refer to the energy losses that occur due to the flow of current within an electrolyser system. These losses are a consequence of the material's resistance to the flow of electric current, following Ohm's law, depicted in Equation 2.2. Here,  $V$  denotes the potential difference across the conductor measured in volts ( $V$ ),  $i$  is the current flowing through the conductor in amperes ( $A$ ), and  $R$  represents the resistance of the conductor in ohms ( $\Omega$ ). In the context of an electrolyser, "the conductor" encompasses the entire electrical circuit, including both the electrolyser components and the electrolyte's ionic conductivity. Notably, the ohmic drop ( $iR$ ) occurring across the electrolyte and ion exchange membrane represents a direct loss of potential within the system, due to its ionic conductivity under the influence of the current flow, and is distinct from overpotential [30].

$$V = i \cdot R \quad (2.2)$$

### Energy Efficiency

Another figure of merit in electrochemical reactions is the energy efficiency (EE), which is denoted by Equation 2.3. Here,  $E_0$  represents the equilibrium potential voltage in V,  $\eta$  signifies the overpotential in V, and  $iR$  represents the ohmic losses. The EE serves as a metric for quantifying the energy utilized in forming a product relative to the total energy used. A high EE is required for an efficient and economically feasible process [33, 30].

$$EE = \frac{E_0 \times FE}{E_0 + \eta + iR} \quad (2.3)$$

### Butler-Volmer equation

The Butler-Volmer equation fundamentally characterizes the relationship between the current density at an electrode and the electrode's potential in the context of electrochemical reactions. It plays an important role in electrochemistry by quantifying how the rate of electron transfer reactions—both oxidation and reduction—is affected by the electrode potential. This relationship is important for designing and optimizing electrochemical cells, including batteries, fuel cells, and electrolysers, where controlling the reaction kinetics is essential for efficiency and stability. The equation is expressed in Equation 2.4 [34].

$$i = i_0 \left( \exp \left( \frac{\alpha_{anode} n F}{RT} (E - E_{eq}) \right) - \exp \left( - \frac{(1 - \alpha_{cathode}) n F}{RT} (E - E_{eq}) \right) \right) \quad (2.4)$$

The equation parameters are as follows:  $i$  represents the current density in  $A m^{-2}$ , indicating the rate of charge transfer per unit area of the electrode.  $i_0$ , the exchange current density in  $A m^{-2}$ , reflects the intrinsic rate of the redox reaction at the electrode/electrolyte interface in the absence of overpotential.  $\alpha$ , the charge transfer coefficient, is a dimensionless parameter that indicates the asymmetry of the energy barrier for electron transfer.  $z$  is the number of electrons transferred in the reaction, and  $F$  is the Faraday constant ( $96,485.332 C mol^{-1}$ ), representing the charge per mole of electrons.  $R$  denotes the molar gas constant ( $8.314 J K^{-1} mol^{-1}$ ),  $T$  is the absolute temperature in Kelvin ( $K$ ),  $E$  is the electrode potential in Volts ( $V$ ), and  $E_{eq}$  represents the equilibrium potential in Volts ( $V$ ), the potential at which the rates of the forward and reverse reactions are equal [35].

### Tafel equation

The Tafel equation is utilized to link the rate of electrochemical reactions with the overpotential required to achieve that rate. This equation is displayed in Equation 2.5. In this equation,  $R$  denotes the molar gas constant,  $T$  represents the temperature in Kelvin ( $K$ ),  $\alpha$  is the charge transfer coefficient,  $F$  stands for the Faraday constant,  $i$  is the current density in  $A m^{-2}$ , and  $i_0$  signifies the exchange current density in  $A m^{-2}$  [35]. The exchange current density that can be deduced from the plot's intercept, reveals reaction kinetics and catalytic properties [36]. The different products of CO<sub>2</sub>RR necessitate accurately distinguishing exchange current and Tafel slopes for these products. Using partial current density, instead of total current density, is the conventional approach for plotting the Tafel slope of a specific CO<sub>2</sub> product. Using overall current density to calculate the Tafel slope incorporates contributions from both

CO<sub>2</sub> reduction and Hydrogen Evolution Reaction (HER). [30]. The Tafel slope, derived from electrochemical measurements, helps investigate the reaction process, speeding up research and improving reaction control in electrolyzers.

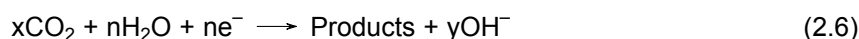
$$\eta = a + b \cdot \log(i) = 2.303 \cdot \frac{RT}{\alpha F} \log\left(\frac{i}{i_0}\right) \quad (2.5)$$

### Stability

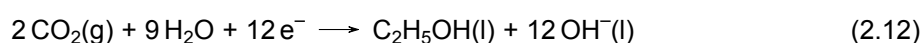
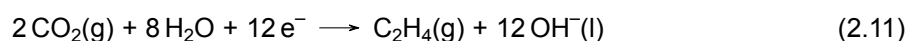
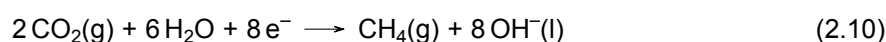
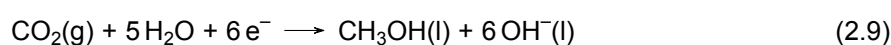
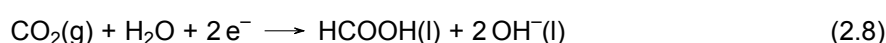
Operating stability is an important factor in electrochemical processes. A reliable system maintains a steady potential for thousands of hours and stable product selectivity for efficient reactions [37]. Stability is of the essence for an economically viable industrial-scale process, as the process needs steady reactor outputs to optimize the separation process further downstream. However, the stability and lifetime of the electrochemical cell in CO<sub>2</sub>RR, including catalyst, electrode, electrolyte, ion exchange membrane, and the cell itself, is an underexplored aspect [30]. In addition, stability can be compromised by impurities or contaminants that can cause catalyst deactivation.

#### 2.1.1. CO<sub>2</sub>RR

The fundamental aim of CO<sub>2</sub>RR is to convert a chemically inert compound CO<sub>2</sub> to higher-value compounds in an electrochemical reaction with a catalyst. The general form of the reaction equation is given by Equation 2.6 [38].



This reaction can follow multiple pathways leading to different (gas or liquid) products, depending on the amount of electrons consumed in the reaction and the used catalyst. The seven most common products, and their half-cell reactions, are listed in Equation 2.7 to Equation 2.13. If CO<sub>2</sub>RR is performed in an aqueous medium, then the HER occurs in competition with the CO<sub>2</sub>RR, listed in Equation 2.14. CO<sub>2</sub> can also react with H<sup>+</sup> ions, but since the reaction environment commonly has a high pH, the alkaline reactions, as displayed will take place [39, 40, 29, 41]. Studies have identified other possible products resulting from the CO<sub>2</sub>RR, such as glycol, acetaldehyde, and propionaldehyde. However, these products are generally considered trivial because they are either uncommon or occur only in trace amounts [29]. Therefore, they are not listed in the equations.



The reaction at the anode, commonly referred to as the Oxygen Evolution Reaction (OER), is displayed in Equation 2.15



Research by Perry et al. and Hui et al. have identified several key properties as desirable for the CO<sub>2</sub>RR [42, 38]. Firstly, the catalytic electrode surfaces (anode and cathode) must exhibit high activity for reducing CO<sub>2</sub>. This can be achieved by selecting electrode materials that are conductive, compatible with the electrolyte, and possess a high surface area to provide many active sites. Additionally, the electrodes must achieve high FE towards the desired product, favouring CO<sub>2</sub>RR over HER. Effective catalyst design also plays a part in reducing overpotentials and ohmic losses, thereby improving EE. Moreover, the pH and ionic conductivity of the electrolyte should be carefully considered; the acidity or alkalinity of the electrolyte can significantly affect the reaction pathways and products, while high ionic conductivity facilitates efficient charge transport between electrodes [19]. Furthermore, the system requires high stability, defined as stable operation for at least 8000 hours, to ensure a sufficient lifespan. Lastly, moderate costs are desired to make the technology economically feasible. Materials for catalyst surfaces and high selectivity membranes can drive up the cost of a CO<sub>2</sub>RR system.

### Catalysts

The product distribution is significantly influenced by the catalyst material and its surface's intrinsic electronic properties, as these factors determine the binding energies of intermediate species and activation barriers. The catalytic activity for CO<sub>2</sub>RR is commonly screened using an H-cell, where recent work has categorized catalysts based on the products that they yield [43, 44]. The different catalysts can be categorized in the following way: Metals such as Pt, Ni, Fe, Al, and Ga can produce CO but with low efficiency, as they tend to favour the HER. Conversely, Au, Ag, and Zn are more efficient at producing CO. Another category includes metals like Sn, Pb, In, and Hg, which primarily generate formate as their main product. Cu is distinctive, belonging to its own category, as it is among the few metals known to effectively produce C<sub>2</sub>+ products. Recent work on catalysts for CO<sub>2</sub>RR focuses on testing novel catalyst material combinations and nanoparticle structures, as it has a direct effect on electrolyser performance, both FE and EE [45, 46].

## 2.2. Electrolysers

This section discusses state-of-the-art gas-fed CO<sub>2</sub> electrolysers and provides an in-depth analysis of bicarbonate electrolysers, including their working mechanisms, the impact of design parameters, and recent experimental findings. The primary focus is on single-carbon CO<sub>2</sub>RR processes producing syngas, with additional exploration of literature on C<sub>2</sub>+ products.

### 2.2.1. Gas-fed electrolysers for CO<sub>2</sub>RR

The heart of an industrial-scale process for CO<sub>2</sub> conversion is the electrolyser. In the cell, the CO<sub>2</sub>RR take place with the help of a catalytic electrode surface and an applied potential. Up until recently, this typically happened through supplying a (aqueous or gaseous) purified feed stream to a catalytic electrode surface that facilitates the CO<sub>2</sub>RR. Simultaneously, the OER is facilitated by the anode surface, producing oxygen. As a result of the research towards optimizing CO<sub>2</sub>RR systems, a wide variety of gas-fed electrolyser configurations that can effectively yield CO<sub>2</sub>RR products have been tested. Flow cells are the category of choice for larger-scale processes, due to their controllable flow and reaction rates, which also enable higher current densities due to reduced mass transfer limitations. Examples of flow cells used for CO<sub>2</sub>RR include Proton Exchange Membrane cell (PEM), Solid Oxide Electrolyte cell (SOEC), and Membrane Electrode Assembly (MEA) cells.

#### CO<sub>2</sub> flow rate and water management

A CO<sub>2</sub>RR flow cell electrolyser needs to be designed to effectively manage different parameters to achieve high FEs. One of them is the management of the CO<sub>2</sub> flow rate. At too low a flow rate, the reaction shifts towards the HER, causing the electrons to form H<sub>2</sub> instead of the desired product [17, 18]. A higher flow rate increases product formation but decreases the single-pass conversion of the CO<sub>2</sub> [47]. Another factor that needs to be managed is the water concentration. Sufficient water is required

to achieve high FEs, but flooding the electrode will favour the HER because the CO<sub>2</sub> cannot access the electrode [48].

### Carbonate formation

During the gas CO<sub>2</sub> fed CO<sub>2</sub>RR process, hydroxide ions (OH<sup>-</sup>) are generated, which can further react with other CO<sub>2</sub> molecules present in the solution. This side reaction leads to the formation of carbonates, which can adversely affect the efficiency of the CO<sub>2</sub> conversion process because it competes with the desired electrochemical reduction of CO<sub>2</sub>. Essentially, carbonate formation reduces the availability of CO<sub>2</sub> molecules for the CO<sub>2</sub>RR, thereby decreasing the overall CO<sub>2</sub> conversion rate [19]. This emphasises the management of pH in a flow cell as too high pH is known to cause carbonate formation, while low pH has proven to shift selectivity towards HER while [16, 49]. The reaction equation for carbonate formation is listed in Equation 2.16.



### Recent advancements in gas -fed electrolysers

In Table 2.1, a compilation of recent experimental data for CO<sub>2</sub>RR to CO is presented, including details on reactor configuration, cell voltage, current density, and FE<sub>CO</sub>. Recent studies have demonstrated high FE<sub>CO</sub> values (90% and above) along with industrially relevant current densities (exceeding 100 mA/cm<sup>2</sup>). This was achieved by optimizing cell configurations, reaction conditions and catalyst performance.

| Reactor Configuration | Cell Voltage (V) | Current Density (mA/cm <sup>2</sup> ) | FE <sub>CO</sub> (%) | Reference |
|-----------------------|------------------|---------------------------------------|----------------------|-----------|
| 3-compartment GDE     | 6                | 150                                   | 52                   | [50]      |
| 3-compartment GDE     | 3,9              | 100                                   | 40                   | [51]      |
| Zero gap              | 3                | 250                                   | >90                  | [52]      |
| 3-compartment GDE     | N.S.             | 150                                   | >90                  | [53]      |
| 3-compartment GDE     | 7,5              | 300                                   | 60                   | [54]      |
| 3-compartment GDE     | 3                | 350                                   | >90                  | [55]      |
| Zero-gap              | 3,8              | 300                                   | 96                   | [56]      |
| Zero-gap              | 3,4              | 100                                   | 70                   | [57]      |
| Micro flow cell       | 2,2              | 250                                   | >95                  | [58]      |
| 3-compartment GDE     | N.S.             | 200                                   | 90                   | [59]      |
| Flow cell             | 3,0              | 885                                   | 98                   | [17]      |
| Zero-gap              | 3,5              | 350                                   | 90                   | [60]      |
| MEA                   | 2,9              | 100                                   | 99                   | [61]      |
| MEA                   | 3,3              | 600                                   | 93                   | [62]      |
| Flow cell             | 2,0              | 100                                   | 99                   | [63]      |
| Zero-gap              | 3,4              | 900                                   | 75                   | [64]      |

**Table 2.1:** Compilation of Experimental Data of CO<sub>2</sub> Reduction to CO in gas-fed CO<sub>2</sub> electrolysers. (N.S.: Not Specified).

### 2.2.2. Bicarbonate electrolyser for CO<sub>2</sub>RR

As stated in section 1.1, recent work by the Berlinguette group demonstrated a novel integrated CCU process for CO<sub>2</sub> capture and conversion using a bicarbonate electrolyser. This section discusses the bicarbonate electrolyser architecture, reaction equations, recent advancements, and key design parameters along with their effects.

#### Electrolyser layout and working principle

The bicarbonate electrolyser configuration as designed by the Berlinguette group is depicted in Figure 2.1. From left to right, the cell consists of:

1. An anode flow field plate supplies water and KOH electrolyte to the anode compartment and allows OER products to flow out of the anode compartment.
2. Nickel (Ni) mesh anode catalyzing OER.

3. BPM for splitting water, providing  $\text{H}^+$  ions for the cathode compartment and  $\text{OH}^-$  for the anode compartment.
4. MEA consisting of a silver (Ag) catalyst layer sprayed onto a porous Gas Diffusion Layer (GDL).
5. A cathode flow field plate supplying the  $\text{HCO}_3^-$  to the cathode compartment and removing  $\text{CO}_2$ RR product from the cathode compartment.

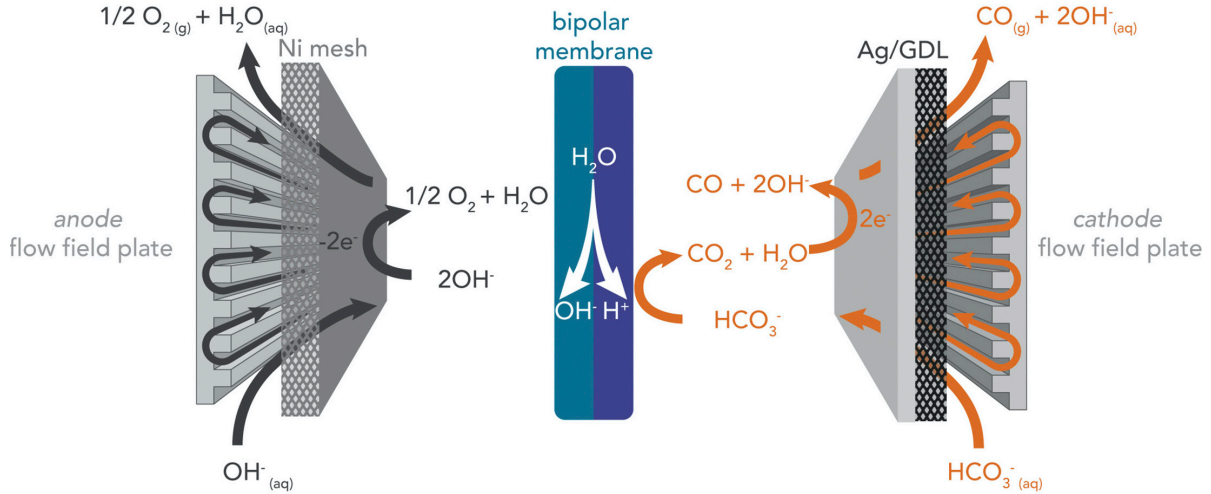


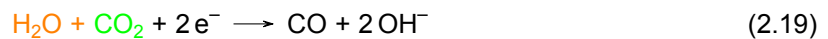
**Figure 2.1:** Schematic view of the bicarbonate flow cell. Correction on this figure: no KOH is consumed in the anode reaction; only water in the form of  $\text{OH}^-$  supplied by the BPM is consumed in the OER [21].

The operating principle is as follows:  $\text{HCO}_3^-$  enters the cathode flow plate and diffuses through the Ag/GDL layer, subsequently permeating the cathode layer. The  $\text{HCO}_3^-$  encounters  $\text{H}^+$  ions at the BPM surface provided by the bipolar membrane, shifting the acid-base equilibrium reaction (Equation 2.22) to free liberated  $\text{CO}_2$ . This reaction provides the  $\text{CO}_2$  that is required for the  $\text{CO}_2$ RR reaction. Subsequently, it gets reduced on the Ag/GDL catalyst layer to form  $\text{CO}$ , which diffuses through the Ag/GDL and leaves the electrolyser [21]. It has to be noted that the *in situ* generated  $\text{CO}_2$  (*i*- $\text{CO}_2$ ) can also react back into  $\text{HCO}_3^-$  as it forms an equilibrium in the bulk on the cathode compartment (Equation 2.20). Inevitably, the HER (Equation 2.14) is competing with the  $\text{CO}_2$ RR reaction on the cathode surface, producing aqueous hydrogen that diffuses along with the  $\text{CO}$  through the Ag/GDL. The gas compartment of the product stream contains a mixture of  $\text{CO}$ ,  $\text{H}_2$ , and unreacted  $\text{CO}_2$ , while the liquid phase product stream contains  $\text{HCO}_3^-$  that can be fed back to the cathode flow plate [15]. The dominant reactions at the BPM are displayed in Equation 2.17 and Equation 2.18 and the  $\text{CO}_2$ RR at the cathode is displayed in Equation 2.19. The most reactive  $\text{H}^+$  donors are marked orange and the electrochemically active species are marked green.

Reactions at membrane:



$\text{CO}_2$ RR at catalyst:



Equilibrium reaction in the bulk of the liquid:



#### $\text{CO}_2$ utilization ratio

An important performance metric of the bicarbonate electrolyser is its  $\text{CO}_2$  utilization ratio. This metric represents the ratio of  $\text{CO}_2$  that reacts to form  $\text{CO}_2$ RR products to the total  $\text{CO}_2$  input, indicating the percentage of *i*- $\text{CO}_2$  converted into  $\text{CO}_2$ RR products rather than diffusing unreacted into the product

stream. The CO<sub>2</sub> utilization ratio can be calculated by measuring the concentrations of products and CO<sub>2</sub> in the product stream, as shown in Equation 2.21. A high CO<sub>2</sub> utilization ratio is desirable, as it leads to a higher yield of CO<sub>2</sub>RR products and less unreacted CO<sub>2</sub> in the product stream.

$$\text{CO}_2 \text{ Utilization Ratio} = \frac{[\text{product}]}{[\text{product}] + [\text{CO}_2]_{\text{outlet}}} \times 100\% \quad (2.21)$$

### Flowplate layouts

In early setups used by the Berlinguette group, both anode and cathode flow plates use a serpentine channel layout [21, 65]. In more recent work, Lees et al. propose an interdigitated flow plate, where the flow inlet and the flow outlet are not connected [15]. This forces the HCO<sub>3</sub><sup>-</sup> to diffuse through the porous electrode, increasing the concentration of HCO<sub>3</sub><sup>-</sup> near the membrane, resulting in more i-CO<sub>2</sub>, potentially leading to a higher product yield. Additionally, the interdigitated flow plate layout prevents the HCO<sub>3</sub><sup>-</sup> from bypassing the cathode compartment, moving directly from the inlet to the product stream without participating in the desired reactions. These hypotheses are experimentally validated by Zhang et al., concluding that interdigitated flow plates result in higher FE<sub>CO</sub> than both serpentine and parallel flow plates [66]. This was done by using porous electrodes (foam). The effect on flow plate layout for GDE configurations is expected to be similar but has not been experimentally validated yet.

### Recent advancements in bicarbonate electrolyzers

Recent work from the Belinguette research group demonstrates that the bicarbonate electrolyser configuration can operate at FE<sub>CO</sub> values close to those of gas-fed CO<sub>2</sub> electrolyzers at industrially relevant current densities (>100 mA/cm<sup>2</sup>). Gas-fed CO<sub>2</sub> electrolyzers have demonstrated 90%+ FE<sub>CO</sub> (see subsection 2.2.1), where bicarbonate FE<sub>CO</sub> values are reported to reach up to 82%. An overview of recent experimental studies on bicarbonate electrolysis for syngas products is displayed in Table 2.2.

| Electrolyte             | Current Density (mA/cm <sup>2</sup> ) | FE <sub>CO</sub> (%) | Reference |
|-------------------------|---------------------------------------|----------------------|-----------|
| 3,0 M KHCO <sub>3</sub> | 25                                    | 82                   | [21]      |
| 3,0 M KHCO <sub>3</sub> | 100                                   | 39                   | [21]      |
| 3,0 M KHCO <sub>3</sub> | 300                                   | 35                   | [67]      |
| 3,0 M KHCO <sub>3</sub> | 200                                   | 40                   | [67]      |
| 3,0 M KHCO <sub>3</sub> | 100                                   | 60                   | [67]      |
| 3,0 M KHCO <sub>3</sub> | 50                                    | 69                   | [67]      |
| 3,0 M KHCO <sub>3</sub> | 200                                   | 62                   | [14]      |
| 3,0 M KHCO <sub>3</sub> | 100                                   | 82                   | [14]      |
| 3,0 M KHCO <sub>3</sub> | 100                                   | 58                   | [66]      |
| 3,0 M KHCO <sub>3</sub> | 200                                   | 35                   | [66]      |
| 3,0 M KHCO <sub>3</sub> | 300                                   | 25                   | [66]      |
| 2,0 M KHCO <sub>3</sub> | 200                                   | 48                   | [68]      |

**Table 2.2:** Experimental results for bicarbonate electrolyzers.

In addition, the bicarbonate electrolyser has been demonstrated to successfully eliminate the need for a purified CO<sub>2</sub> feed stream. Instead, it utilizes an aqueous bicarbonate solution in conjunction with a BPM to supply CO<sub>2</sub> to the electrode, facilitating the production of CO<sub>2</sub>RR product with a FE<sub>CO</sub> comparable to that of CO<sub>2</sub>-fed electrolyzers [21]. This opens up the pathway to an integrated bicarbonate electrolysis process without the desorption and compression steps that are inherent to gas-fed CCU systems.

As a result of these findings, Kim et al. have pioneered experiments with integrating capture and bicarbonate conversion [69]. They validated the fundamental working mechanism of integrated capture and conversion with a coupled carbon reactor (CCR). They fed a CO<sub>2</sub>/N<sub>2</sub> mixture (20/80 vol%) to an absorption column using a K<sub>2</sub>CO<sub>3</sub> solvent, then fed the resulting CO<sub>2</sub>-rich solvent to a bicarbonate electrolyser, and recycled its catholyte back to the absorption column. At startup, the FE<sub>CO</sub> climbed up to 37% whereafter it reached a steady state of 29%. This decline is deemed to be caused by the decrease of pH in the reactive carbon solution, which reached a steady state at a pH of 9,1. Their

results are all consistent with expected (bi)carbonate equilibria and acid-base kinetics associated with  $\text{CO}_2$  capture and electrochemical  $\text{CO}_2$  desorption [21].

### 2.2.3. Design parameters and their effects on bicarbonate electrolysis

As mentioned in subsection 2.2.2,  $\text{CO}_2$  must be liberated from the bicarbonate solution for the  $\text{CO}_2\text{RR}$  to occur at the electrode. To achieve a high  $\text{CO}_2$  utilization ratio, design parameters should be optimized to maximize the  $\text{CO}_2$  concentration at the cathode surface [68, 15, 21]. This section discusses recent findings on the effects of pressure, temperature, pH, and impurities on  $\text{FE}_{\text{CO}}$ .

#### Effect of pressure

The amount of product produced is governed by the amount of  $\text{CO}_2$  that can be provided to the cathode surface, hence the concentration of the concentration of  $\text{i-CO}_2$ . As posed by Li et al. the bicarbonate electrolyser can produce more  $\text{i-CO}_2$  than the solubility limits [21]. This results in bubbles of gas phase  $\text{CO}_2$ , thereby reducing the concentration of  $\text{CO}_2$  at the electrode. This effect can be countered by increasing pressure so that the solubility of  $\text{CO}_2$  increases, fewer bubbles occur, and a higher concentration of available  $\text{CO}_2$  at the electrode is achieved. Hence, elevated pressures would increase product formation rates by increasing the amount of  $\text{CO}_2$  reactant that can participate in the  $\text{CO}_2\text{RR}$ . Experimental studies, most notably from Zhang et al. have validated this phenomenon [66]. They constructed a pressurized bicarbonate electrolyser and applied constant current density at various pressures (1-4 bar). The  $\text{FE}_{\text{CO}}$  shows a clear dependency on electrolyser pressure, with a pressure increase from 1 atm to 4 atm leading to an  $\text{FE}_{\text{CO}}$  increase from 55% to 95% at ambient temperatures, thus significantly increasing product formation. The effect decreases at higher current densities but is still present. The results are displayed in Figure 2.2.

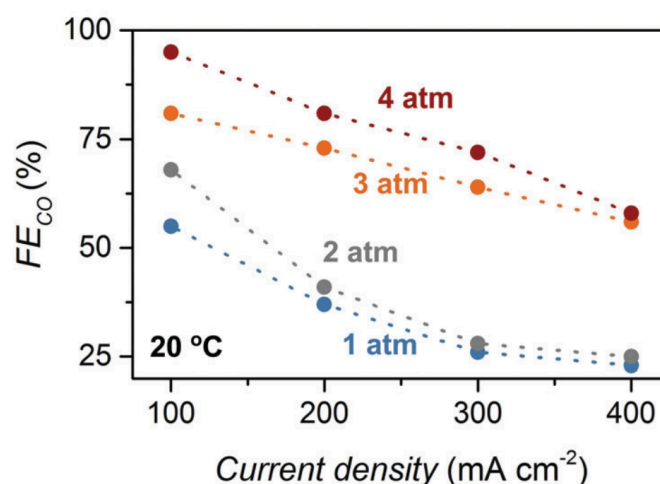
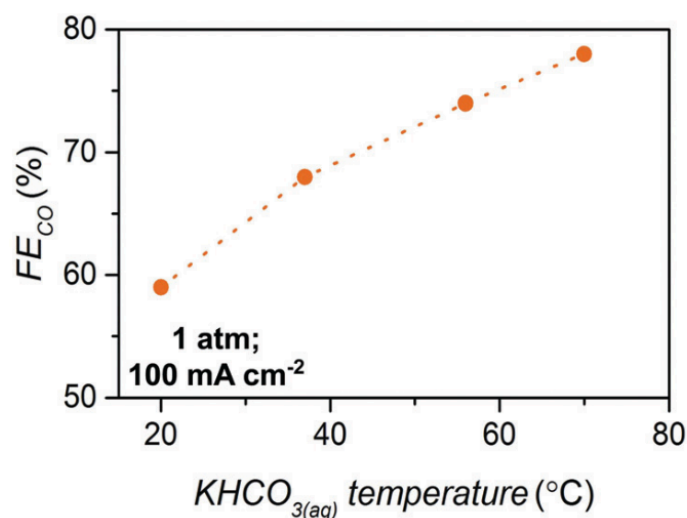


Figure 2.2: Plot of experimental results of  $\text{FE}_{\text{CO}}$  vs. current density at pressures 1-4 atm [66].

#### Effect of temperature

Zhang et al. also demonstrated that an increase in temperature increases the  $\text{FE}_{\text{CO}}$  [66]. The theory behind their findings is that an increase in temperature shifts the equilibrium towards the formation of  $\text{i-CO}_2$  in the bicarbonate dissociation reaction (displayed in Equation 2.22), increasing the  $\text{CO}_2$  concentration at the cathode surface. This reaction would also increase the pH, which would lead to the suppression of the HER. Higher temperatures could also improve the mass transfer kinetics for  $\text{HCO}_3^-$  and  $\text{CO}_2$ . These theories are in line with the gas chromatography (GC) results from Zhang et al. displayed in Figure 2.3. The  $\text{FE}_{\text{CO}}$  at ambient pressure is below 60%, but it increased to 70%, 75%, and 80% at 40°C, 60°C, and 70°C, respectively. These results show a clear dependency of  $\text{FE}_{\text{CO}}$  with an increase in temperature; however, it is difficult to experimentally resolve which mechanism is dominant in causing this. More research on the mechanism behind the increasing  $\text{FE}_{\text{CO}}$  with temperature is needed [70].



**Figure 2.3:** Plot of experimental results of  $FE_{\text{CO}}$  vs.  $\text{KHCO}_3$  temperature [66].

### Effect of pH

The  $\text{CO}_2$  for the reduction reaction is supplied by (bi)carbonate ions ( $\text{HCO}_3^-$ , and  $\text{CO}_3^{2-}$ ). The chemical equilibrium and concentrations are determined by the pH and the temperature of the solution, where the parameters are required to shift the equilibrium towards the formation of  $i\text{-CO}_2$ . The equilibrium of these compounds is plotted against its mole fractions in Figure 2.4. As the plot shows, the equilibrium between  $\text{HCO}_3^-$ ,  $\text{CO}_3^{2-}$ , and  $\text{CO}_2$  is governed by the pH of the solution [15, 23].

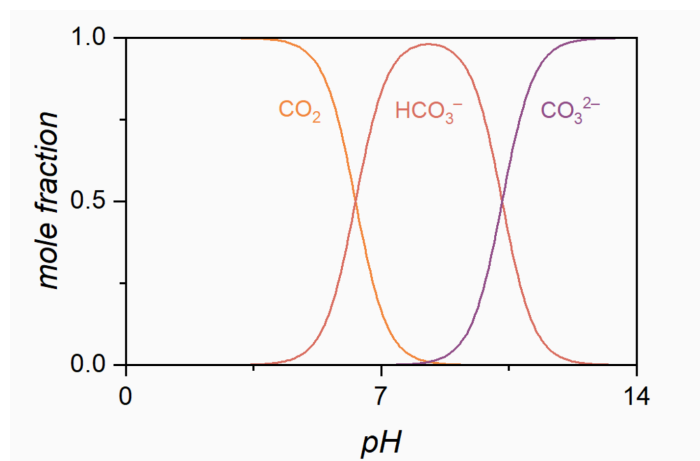


**Figure 2.4:** The thermodynamic equilibrium of (bi)carbonates and  $\text{CO}_2$  in aqueous media (Bjerrum plot). Mole fractions for  $\text{CO}_2(\text{aq})$ ,  $\text{HCO}_3^-(\text{aq})$ , and  $\text{CO}_3^{2-}(\text{aq})$  as a function of pH at ambient conditions (temperature =  $25^{\circ}\text{C}$ ; pressure = 1 atm) [15].

At lower pH levels (acidic conditions), the equilibrium shifts towards the formation of  $\text{CO}_2$ . In the bicarbonate system, the conditions at the cathode surface of the BPM are acidic, which shifts the equilibrium towards the formation of  $i\text{-CO}_2$ , thereby increasing the availability of  $\text{CO}_2$  at the electrode for the  $\text{CO}_2\text{RR}$ , which increases the yield of  $\text{CO}$  product and thus the  $FE_{\text{CO}}$  [68, 21].

While the formation of  $i\text{-CO}_2$  favours acidic conditions, the  $\text{CO}_2\text{RR}$  at the electrode requires alkaline conditions. The in-situ generated  $\text{OH}^-$  increases the bulk pH to favour  $\text{CO}_3^{2-}$  formation. Increase in pH

shifts the equilibrium towards  $\text{CO}_3^{2-}$ , as Figure 2.4 underscores. The  $\text{CO}_3^{2-}$  forms  $\text{HCO}_3^-$  at the BPM, which in turn reacts with the  $i\text{-CO}_2$  to form CO product and new  $\text{CO}_3^{2-}$  at the catalyst, as can be seen in Equation 2.18 and Equation 2.19. The aqueous CO leaves the system through the GDL and the produced  $\text{CO}_3^{2-}$  can diffuse to the BPM to start this cycle again.

The bicarbonate electrolyser facilitates both conditions. The BPM layer is acidic through the supply of  $\text{H}^+$ , while the bulk pH and pH near the electrode are alkaline due to the supply of  $\text{HCO}_3^-$  from the flow channel. This effectively establishes a pH gradient over the width of the cathode compartment. This phenomenon is experimentally validated and modelled by Lees et al., resulting in the plot displayed in Figure 2.5 [67]. With the help of this gradient, an optimal spacing between membrane and cathode can be established, facilitating acidic conditions at the BPM to enable the formation of  $i\text{-CO}_2$ , while maintaining the favourable alkaline conditions at the electrode surface and limiting mass transfer limitations [21]. In the case of Figure 2.5, a zero-gap configuration is tested. It shows that the conditions at the BPM interface (left in the plot) do not reach the desired acidic conditions (lower than 7, as Figure 2.4 indicates) for significant generation of  $i\text{-CO}_2$ .

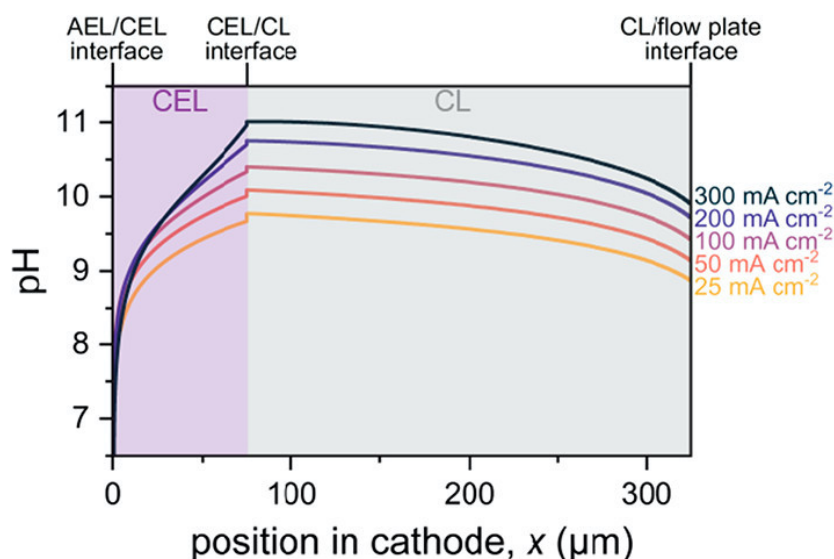


**Figure 2.5:** pH within the bicarbonate electrolyser cathode compartment for different applied current densities [67].

Lee et al. have continued experimental research on this membrane-cathode spacing, varying the space between the BPM and the electrode [71]. With a zero-gap configuration ( $0 \mu\text{m}$  spacing), they established a very small pH gradient and achieved pH levels too high for  $i\text{-CO}_2$  generation, in line with the findings of Lees et al. When spacing was increased to  $64 \mu\text{m}$  and  $135 \mu\text{m}$ , a low pH ( $\text{pH} = 3$ ) was achieved at the BPM. This caused  $\text{CO}_2$  concentrations to increase to 4 and 28 vol%  $\text{CO}_2$ , respectively, at the membrane surface (at  $300 \text{ mA/cm}^2$  with  $1.5 \text{ M K}_2\text{CO}_3$  electrolyte). The results (displayed in Figure 2.6) confirm that the spacing between the BPM and electrode can be optimized for higher formation of  $i\text{-CO}_2$ .

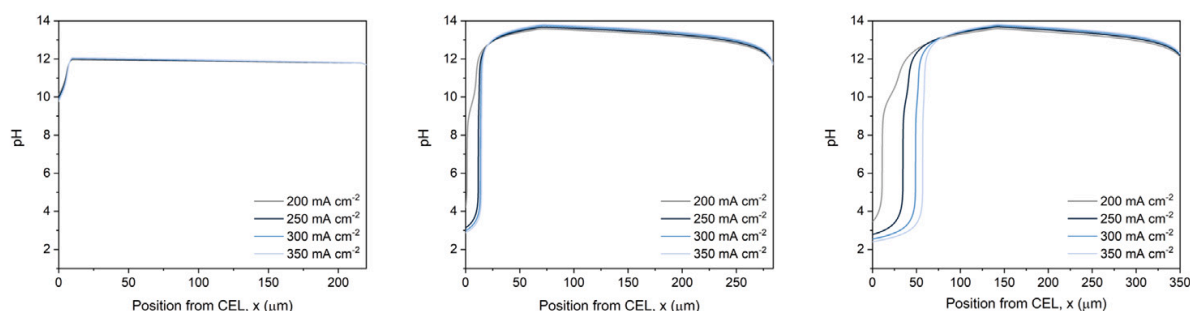


**Figure 2.6:** pH profile at  $0\mu\text{m}$  (left),  $64\mu\text{m}$  (middle), and  $135\mu\text{m}$  (right) spacing at the applied current densities from 200 to 350  $\text{mA}/\text{cm}^2$  in 1,5 M  $\text{K}_2\text{CO}_3$  electrolyte [71].

### Effect of impurities on $\text{FE}_{\text{CO}}$

Zhang et al. evaluated the resilience of the bicarbonate electrolyser against impurities by subjecting it to common impurities found in post-combustion captured flue gases over 80 hours at  $65\text{ mA}/\text{cm}^2$  [66]. They introduced 100 ppm concentrations of  $\text{SO}_4^{2-}$ ,  $\text{SO}_3^{2-}$ ,  $\text{NH}_4^+$ ,  $\text{NO}_3^-$ , and  $\text{Cl}^-$  into a 3,0 M  $\text{KHCO}_3$  solution. Their findings indicated that most impurities, except  $\text{NO}_3^-$ , had insignificant effects on the  $\text{FE}_{\text{CO}}$ . The  $\text{FE}_{\text{CO}}$  significantly decreased with the addition of  $\text{NO}_3^-$ , yet promptly recovered upon electrolyte refreshment, indicating no lasting impact on electrolyser performance. This study concluded that the bicarbonate electrolyser under examination showed greater impurity tolerance compared to gaseous  $\text{CO}_2$ -fed systems. This tolerance is advantageous, as gas-fed  $\text{CO}_2\text{RR}$  electrolysers can experience failure when exposed to flue gas contaminants in the  $\text{CO}_2$  feed [72].

### 2.2.4. $\text{CO}_2\text{RR}$ for $\text{C}_2+$ products

As discussed in subsection 2.1.1, the  $\text{CO}_2\text{RR}$  can follow pathways to higher order  $\text{C}_2+$  products, depending mainly on the catalyst material and structure, in addition to the applied potential and reaction conditions. Many experimental studies have been conducted on the direct production of  $\text{C}_2+$  products in gas-fed  $\text{CO}_2$  electrolysers. Recent advancements in these electrolysers have enabled high FE values ( $>50\%$ ) towards  $\text{C}_2\text{H}_4$  using a Cu catalyst and have shown stable operation at high currents, while also producing  $\text{C}_2+$  products other than ethylene, in smaller quantities and with lower FE values. [11, 73, 74].

#### Bicarbonate electrolysis for $\text{C}_2+$ products

As gas-fed electrolysers have demonstrated significant potential for efficient  $\text{C}_2+$  production, initial experimental work on bicarbonate electrolysers exploring this production pathway has been conducted. Lee J. et al. tested a setup with a combined Ag/Cu electrode, where the generated  $\text{i-CO}_2$  reacts to CO on the Ag catalyst, and subsequently, the CO reacts to  $\text{C}_2+$  products (mostly ethylene) on the Cu part of the same electrode [75]. They tweaked the microenvironment to achieve a high local pH and low water content, resulting in a 41% FE towards  $\text{C}_2+$  products. Additionally, Lee G. et al. achieved a FE of 47% towards  $\text{C}_2+$  products and a 34% FE towards ethylene specifically (at 4,1 V and  $300\text{ mA}/\text{cm}^2$  [71]. They used a catalyst with molecularly dispersed cobalt phthalocyanines on carbon nanotubes (CoPCs-CNTs), which sped up the process of intermediate CO formation, resulting in a product with single-C components under the detection limit of GC (0.9wt%). Subsequently, they coupled their bicarbonate electrolyser to a carbon capture unit, yielding a steady FE towards  $\text{C}_2+$  products in the range of 36% - 43% for the first 10 hours, whereafter it slowly declined. This represents the most advanced state of a production system for flue gas to  $\text{C}_2+$  products with a bicarbonate electrolyser. Experimental work towards an integrated system for  $\text{C}_2+$  products with catholyte recycling, has yet to be conducted.

The direct pathway to  $\text{C}_2+$  products from bicarbonate electrolysis has its limitations. The FE values reported are substantial, but still significantly lower than achieved FE values for single C products (see subsection 2.2.2), which is most likely due to the complexity of the intermediate reactions at the cathode. In addition, high overpotentials are required to form the C-C coupling of higher order  $\text{C}_2+$  products, which results in a lower EE [71]. More research is needed in this area.

## 2.3. Carbon capture

The goal of carbon capture is to isolate CO<sub>2</sub> from other compounds in flue gas and prevent its release into the atmosphere. This section discusses the composition and impurities of flue gases from the steel industry, and the Benfield process for carbon capture, including the use of promoters. Finally, the integrated CCU system, where the Benfield process is integrated with the bicarbonate electrolyser, is discussed, along with its limitations.

### 2.3.1. Flue gas composition

Currently, coal-fired blast furnaces are the predominant method in the steel industry. In a typical blast furnace flue gas stream, CO<sub>2</sub>, CO, H<sub>2</sub>, O<sub>2</sub>, Ar, and N<sub>2</sub> are the main components present at ambient pressure and elevated temperatures, around 160 °C [76]. A suitable solvent does not react with these other compounds, allowing CO<sub>2</sub> to be isolated from the stream to serve as feedstock for a CO<sub>2</sub>RR process. Additionally, blast furnace flue gas typically contains impurities such as H<sub>2</sub>S, COS, SO<sub>2</sub>, and NO<sub>2</sub> in ppm quantities, resulting from coal combustion. Some C<sub>2</sub>+ compounds are also present, albeit in significantly lower trace amounts [76]. These C<sub>2</sub>+ compounds are generally considered negligible due to their minimal quantities.

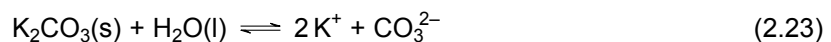
Novel steelmaking processes employing DRI methods, such as the Midrex process and the Energiron III process, utilize syngas as a feedstock instead of coal for the shaft furnace. In both processes, natural gas (CH<sub>4</sub>) is fed to a reformer where it is converted to syngas. Subsequently, the syngas is fed to the Electric Arc Furnace (EAF), and both steps result in CO<sub>2</sub> emissions. This makes the system a potential fit for an integrated CCU system, as CO<sub>2</sub> emissions can be reacted back into syngas and fed back into the EAF, enabling a circular process. Additionally, a byproduct of the bicarbonate electrolyser is O<sub>2</sub>, which can also be fed back into the EAF. An overview of both processes is displayed in section A.1. The flue gases from these processes have similar main components to those from traditional blast furnaces but contain fewer sulfur and nitrogen contaminants [27]. This difference suggests that pre-treating the flue gas for a CO<sub>2</sub>RR system could be simpler and less costly for DRI methods [77].

#### Methods for CC in the integrated process

As discussed in chapter 1, the most common methods for CC are absorption, adsorption, and membrane gas separation, with absorption being the industry standard for CCU, where many different solvents can be employed. A variety of commercially used solvents exist for CC, most notably amine-based, ammonia, and carbonate salts. It has to be assessed per case which solvent is the most suitable. In the case of an integrated CCU process, the CC unit process serves two purposes: 1) preventing CO<sub>2</sub> from being emitted into the atmosphere; 2) converting the CO<sub>2</sub> to serve as feedstock for the bicarbonate electrolyser. As the bicarbonate electrolyser requires an aqueous feed stream containing HCO<sub>3</sub><sup>-</sup>, the only solvent category that can realize this conversion is a carbonate-based solvent. The benefits of these solvents are lower regeneration energy, less corrosion, and higher durability; however, their main drawback is the low CO<sub>2</sub> absorption rate at ambient pressures and temperatures, due to slow hydration kinetics of CO<sub>2</sub> [69, 78, 79].

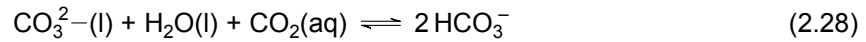
### 2.3.2. Benfield process

CC with the use of a K<sub>2</sub>CO<sub>3</sub> solvent is commonly known as the Benfield process. This process is widely used for removing CO<sub>2</sub> from large gas streams and involves the following equilibrium reactions [80]: Dissolution of K<sub>2</sub>CO<sub>3</sub> in water (Equation 2.23), ionization of water (Equation 2.24), reaction of OH<sup>-</sup> with CO<sub>2</sub> to form bicarbonate (Equation 2.25) and the formation of carbonate (Equation 2.26).





As the carbonate formation reaction is instantaneous, the overall reaction between aqueous potassium carbonate and  $\text{CO}_2$  can be represented as Equation 2.27. Given the strong electrolytic nature of potassium carbonate and bicarbonate, it is assumed that the metal exists primarily as  $\text{K}^+$  ions. Thus, Equation 2.27 can be expressed as Equation 2.28 [81].



### 2.3.3. Enhancing capture rates in the Benfield process

The Benfield process is kinetically limited under ambient pressures and temperatures, which is why it is common practice to operate the absorber column at elevated pressures. This shifts the equilibrium in Equation 2.27 towards the formation of  $\text{HCO}_3^-$ , but requires additional energy input. Recent work by Smith explored the effect of temperature on residence time in the column [82]. As shown in Figure 2.7, increasing the temperature up to  $60^\circ\text{C}$  significantly reduces residence time. However, beyond  $80^\circ\text{C}$ , the improvements become less pronounced, while the energy required to maintain these higher temperatures increases substantially.

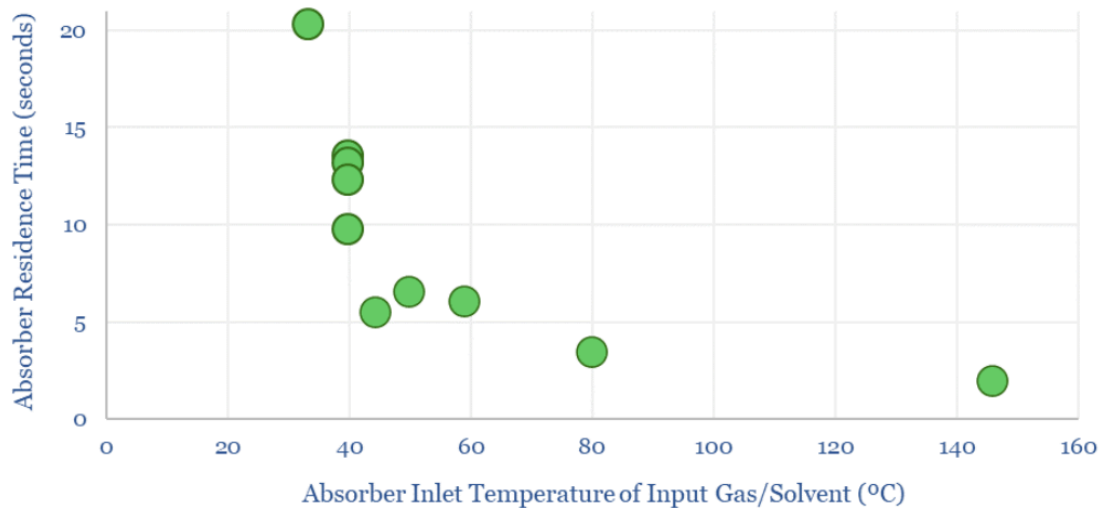


Figure 2.7: Residence time vs. absorption column temperature for Benfield process [82].

A similar principle applies to pressure. Increasing the pressure from ambient conditions significantly enhances capture kinetics; however, excessively high pressures raise energy demands for pressurization and require the system to be highly pressure-resistant. Consequently, typical operating conditions involve pressures not exceeding 10 bar and temperatures below  $100^\circ\text{C}$  [83].

#### Promotors

In addition to improving reaction rates by adjusting the conditions in the absorber column, promotors can be used to enhance reaction rates. The general reaction mechanisms of the rate promotors in the carbonate solution are shown in Equation 2.29 and Equation 2.30.



Anderson et al. have shown that, even without the addition of promoters, adjustments in these parameters can lead to CO<sub>2</sub> capture rates of up to 50% [78]. Furthermore, Behr et al. and Pachitsas et al. have introduced various promoters, demonstrating experimental capture rates of up to 90%, indicating the significant potential for efficiency improvements [84, 85]. Industry-standard promoters are piperazine and glycine and are known to improve reaction kinetics in the Benfield process by up to 500% [69]. Due to these significant improvements, these promoters are commonly used when the carbon capture unit operates standalone.

#### Amine-based promoters for CCU

The use of promoters in an integrated CCU process comes with a trade-off. The promoter itself ends up in the absorption solvent stream and enters the electrochemical reaction space, which could potentially influence the electrolyser's performance. Kim et al. experimentally tested the influence of piperazine and glycine on the FE<sub>CO</sub> of a bicarbonate electrolyser with the following results: In his setup, he achieved an FE<sub>CO</sub> of 35% for the unprompted Benfield process [69]. When he introduced glycine and piperazine, the FE<sub>CO</sub> dropped to 30% and 5% respectively. The significant reduction in FE<sub>CO</sub> deems piperazine as non-suitable for promoting the integrated CCU process. As a result, Kim et al. continued to test with glycine and found that while it reduced the FE<sub>CO</sub> slightly, it increased the i-CO<sub>2</sub>, which counters the decrease in FE<sub>CO</sub>. They found that 0,1 M glycine in combination with a 1 M K<sub>2</sub>CO<sub>3</sub> solvent yielded the highest CO<sub>2</sub> capture rate without compromising syngas product formation, thus demonstrating an optimum in the trade-off. It has to be noted that these results were obtained in a lab setting. For industrial applications, it must be ensured that the promoter does not end up in the product stream, hence a new downstream separation step may be required, influencing the optimum in the trade-off.

#### Carbonic anhydrase for CCU

Another method of enhancing capture rates in K<sub>2</sub>CO<sub>3</sub> solvents involves carbonic anhydrase. Carbonic anhydrase, a zinc metalloenzyme, efficiently catalyzes the hydration of CO<sub>2</sub> to form bicarbonate, thereby speeding up the capture process. Recent reports have demonstrated up to a 20-fold increase in captured CO<sub>2</sub> in the capture column when carbonic anhydrase was added to the capture solution [86, 87]. For the integrated process, it is essential to examine the impact of the added carbonic anhydrase on the electrolyser performance, as a consistent concentration of enzymes will circulate in both the capture column and the bicarbonate electrolyser. Fink et al. have coupled carbonic anhydrase capture with the bicarbonate electrolyser on lab-scale and observed a substantial reduction in FE<sub>CO</sub> compared to a system without the enzymes, where it dropped from 56% to 16% [88]. The measured i-CO<sub>2</sub> concentration slightly decreased when the enzymes were employed, from 30000 ppm to 27000 ppm, which is considered insignificant by Fink et al. They concluded that a trade-off exists between faster capture and lower cell performance when using carbonic anhydrase. Additionally, they successfully modified the microporous layer at the cathode to inhibit the enzymes from permeating into the cathode or anode compartment, thus presenting a pathway for integrating bicarbonate electrolysis with enzymatic CO<sub>2</sub> capture.

## 2.4. Integrating capture and conversion

Recent work on coupling the Benfield process to a bicarbonate electrolyser has primarily focused on non-circular processes, where the output from the absorption column serves as the inflow for the electrolyser, enabling a CCU system. In the integrated system proposed by the Berlinguette group, however, the catholyte outlet from the electrolyser is used as the solvent inflow for the absorption column, creating the truly integrated CCU process.

### 2.4.1. Role of pH

In the integrated CCU system, pH plays a crucial role. On the electrolyser side, maintaining a low pH is essential to sustain high FE. As discussed in Figure 2.2.3, the FE is optimal at low pH levels (pH = 7,0 - 9,0), but decreases significantly with higher pH inflows. On the other hand, CO<sub>2</sub> capture in the absorption column is enhanced by a high pH solvent inflow (pH = 11,0 - 13,0), as the solvent can uptake more CO<sub>2</sub> from the flue gas, and the reaction kinetics are faster, as noted in subsection 2.3.2 [89]. For the integrated CCU system to function effectively, the pH step in the electrolyser must be the opposite of the pH step in the absorption column. The electrolyser converts low pH HCO<sub>3</sub><sup>-</sup>-rich solvent into high

pH  $\text{CO}_3^{2-}$ -rich solvent by removing  $\text{CO}_2$  through the  $\text{CO}_2\text{RR}$ . The absorption column must then reverse this process, transforming high pH  $\text{CO}_3^{2-}$ -rich solvent into low pH  $\text{HCO}_3^-$ -rich solvent by absorbing  $\text{CO}_2$  from the flue gas [15]. A schematic overview of the integrated CCU process with favoured pH levels is displayed in Figure 2.8.

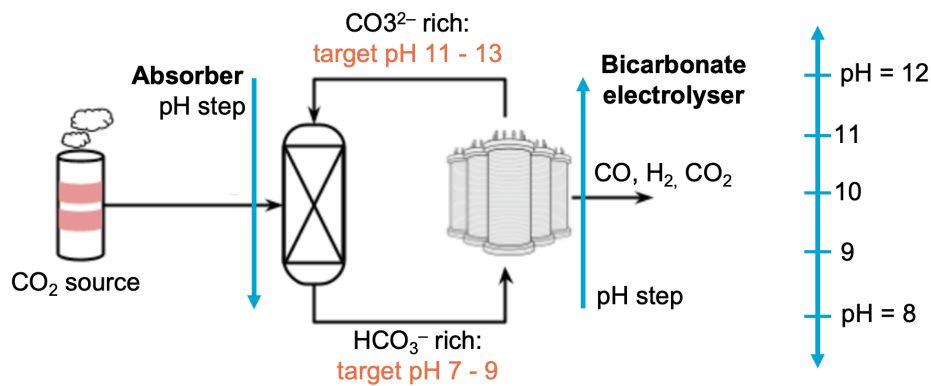


**Figure 2.8:** Schematic overview of favoured pH steps in the integrated CCU process.

### 2.4.2. Closing the loop

Recent work by Almahjed et al. investigated this integrated system and identified the pH step requirement as a potential vulnerability [89]. They demonstrated that when the necessary pH step is not achieved in either the electrolyser or the absorption column, the performance of the subsequent component is compromised. Over multiple cycles, this mismatch can lead to a gradual reduction in solvent effectiveness for  $\text{CO}_2$  capture and decreased efficiency in the electrolyser. This issue is illustrated in Figure 2.9, where each point represents a solvent cycle. The capture fraction drops to nearly zero as the catholyte outlet pH decreases to 9,3 over the first four cycles.

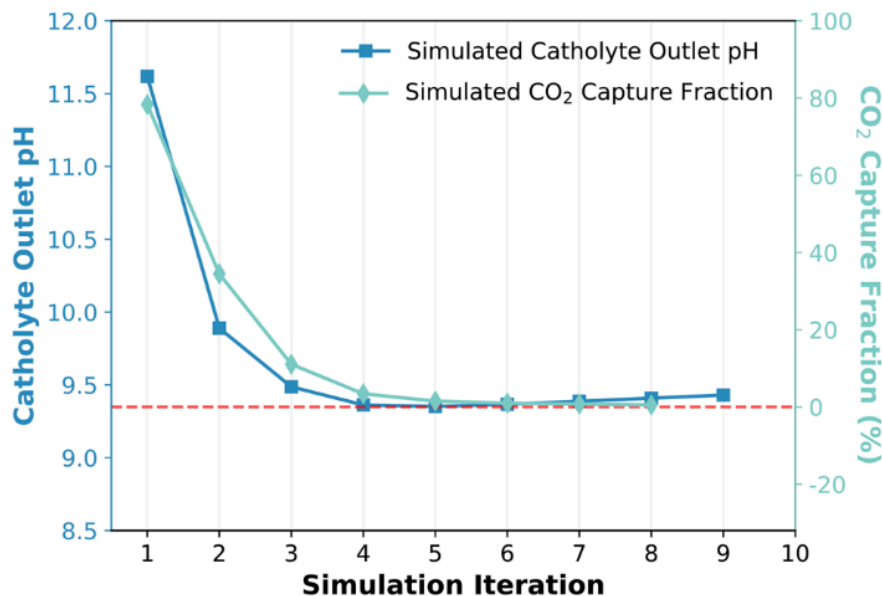


**Figure 2.9:** Illustration of solvent circulation showing reduced capture efficiency as pH increases [89].

In addition, stability is of great importance. If the electrolyser's performance declines over time, so does the conversion efficiency, resulting in the failure to achieve the required pH step. This leads to diminished system performance after only a few cycles, as Almahjed et al. proved [89].

This highlights the critical role of pH and the inherent trade-offs within the system. Achieving a high pH catholyte outflow from the bicarbonate electrolyser reduces  $FE_{CO}$ , as high pH levels negatively impact performance. Conversely, operating the electrolyser at a low pH to maintain high  $FE_{CO}$  results in less effective  $CO_2$  capture and slower reaction kinetics in the absorption column. As such, a balance must be struck between enhancing  $CO_2$  capture efficiency in the absorption column at a higher pH inlet and achieving higher conversion efficiency in the electrolyser at a lower pH inlet, depending on the specific operational priorities. Furthermore, ensuring system stability is essential, as any decline in electrolyser performance over time can disrupt the required pH step and significantly reduce overall system efficiency.

## 2.5. Techno-economic analysis

As experimental progress continues in  $CO_2$  electrolysis, the pathway to widespread adoption depends largely on its economic viability. Recently, lab-scale results have been scaled up and integrated into TEA, which estimates the economic feasibility of  $CO_2RR$  systems. This section provides an overview of recent developments in TEA for  $CO_2RR$  electrolysers, covering both gas-fed and bicarbonate electrolysers.

### 2.5.1. TEA for gas-fed $CO_2RR$ systems

In recent years, TEAs with varying levels of depth have been performed on  $CO_2RR$  electrolysers to assess their economic feasibility. Jouny et al. concluded that for gas-fed  $CO_2RR$  systems, single C products, namely CO and formic acid, are cost-competitive with current market prices and have projected positive NPVs in the current techno-economic conditions [29]. Their results are displayed in Figure 2.10. It should be noted that their study analyzed the stand-alone electrolyser, and did not include the upstream and downstream purification steps in the TEA. Verma et al.'s findings align with these results, showing CO and formic acid as the most economically viable products when separation costs are taken into account [37]. However, they did not precisely model the upstream and downstream processes but estimated the separation costs via a Sherwood plot [90]. Gao et al. conducted a TEA for CO, formic acid, ethanol, and ethylene with a more comprehensive model for the electrolyser and the upstream and downstream separation [91]. They reported that the production costs for CO and formic acid could be competitive with market prices under optimistic conditions, in line with the findings from Jouny et al. and Verma et al. [29, 37].

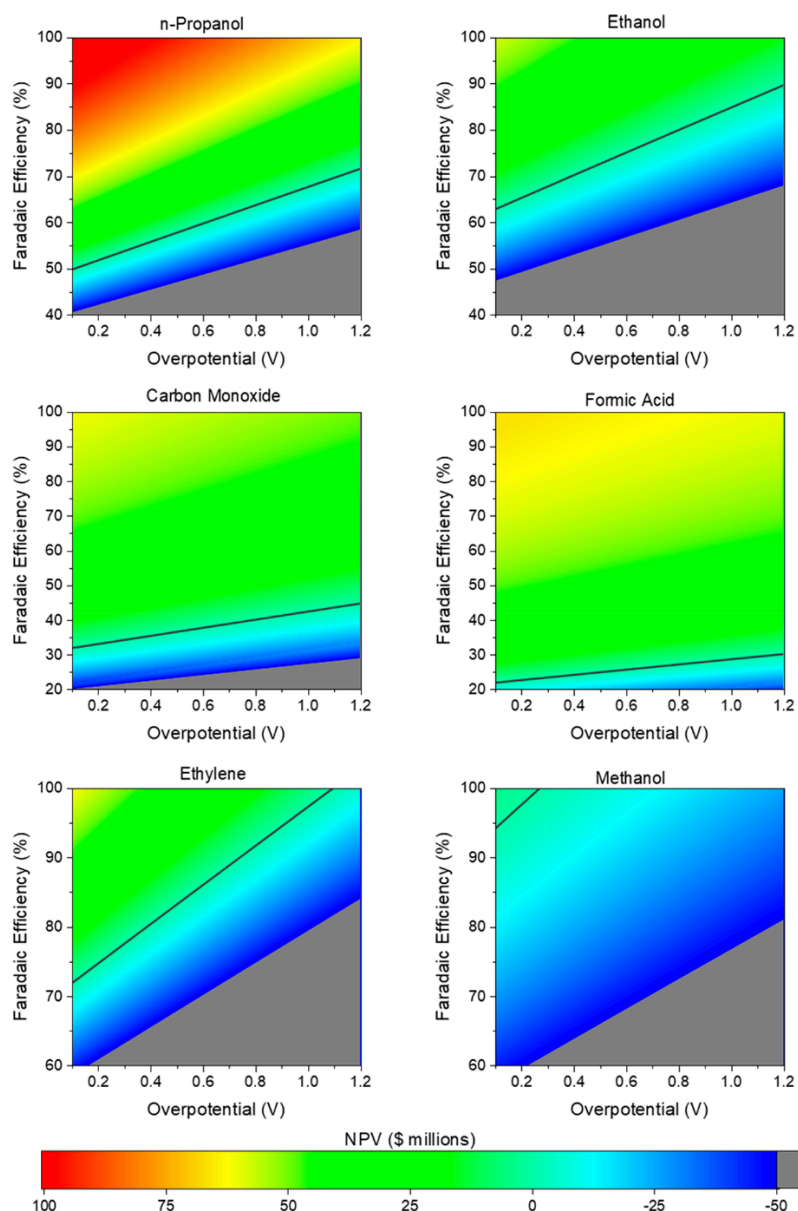


**Figure 2.10:** FE vs. overpotential with colour gradient indicating NPV: the black line indicates an NPV of zero [29].

For higher-order  $C_2+$  products, the TEAs conducted show less positive projections on NPV and economic feasibility. Results from Jouny et al., displayed in Figure 2.10, indicate that significantly higher FE and lower overpotentials are required to achieve positive NPVs for higher-order C products, namely n-propanol, ethanol, ethylene, and methanol. They concluded that economic feasibility is possible for these products, but not under the current economic and technical circumstances. Findings from Gao et al. and Verma et al. support these conclusions [91, 37]. Alerte et al. researched the direct production of  $C_2+$  products, most notably ethylene, and modelled the downstream separation steps needed to recover all the byproducts. They concluded that the benefits of large-scale production can be leveraged to make the process economically feasible for the production of ethylene, in combination with optimistic economic circumstances [92].

### 2.5.2. TEA for bicarbonate electrolyser systems

As discussed in section 1.1, full-system TEAs employing bicarbonate electrolysers are scarce, due to the novelty of the electrolyser configuration itself. Work from Moreno et al. provides insights into how

a bicarbonate system (Carb-E) compares to a reverse water gas shift (rWGS) process and a gas-fed CO<sub>2</sub> electrolyser (Gas-E) when coupled to direct air capture (DAC) for the production of syngas [93]. It showed that the bicarbonate electrolyser can only compete with rWGS and Gas-E processes under very optimistic circumstances. Figure 2.11 demonstrates that under current conditions, the production costs per kilogram for the three evaluated methods are not competitive with the market price of syngas produced using fossil fuels.

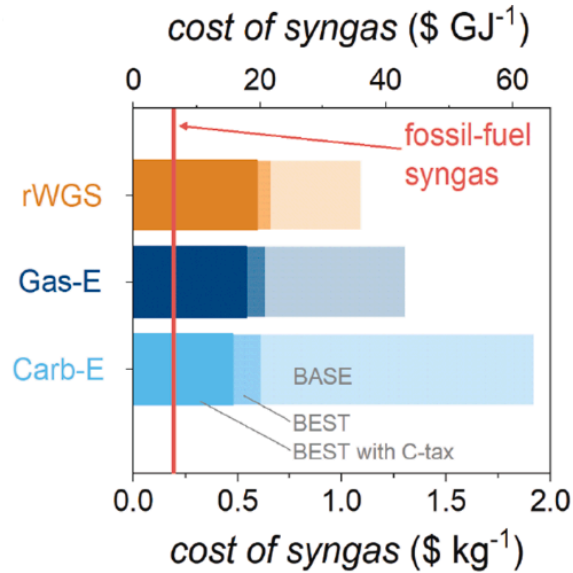
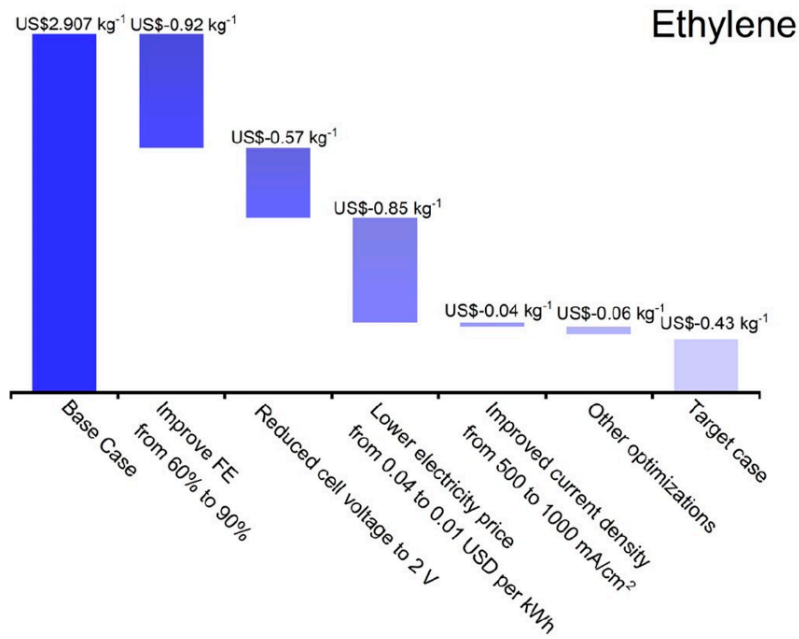


Figure 2.11: Levelized production of syngas for rWGS, Gas-E and Carb-E [93].

### 2.5.3. Enablers

TEAs conducted on gas-fed CO<sub>2</sub>RR and bicarbonate electrolyser systems suggest that economic feasibility pathways are possible, though under highly optimistic conditions. This is particularly relevant for C<sub>2</sub>+ products, which remain economically unfeasible under current conditions, as discussed in subsection 2.5.1. Recent efforts to identify enablers for these technologies have led to the development of bridge plots, which illustrate the path from current production costs to target production costs. Gao et al. constructed such a plot for ethylene using a gas-fed CO<sub>2</sub> electrolyser, shown in Figure 2.12 [91]. These parameters can be divided into cell performance-related and economic-related factors. Cell performance-related factors include improving FE<sub>CO</sub>, reducing overpotential, and minimizing other losses. Increasing current density, however, has shown limited impact on the economics of CO<sub>2</sub> electrolyzers [29, 91].



**Figure 2.12:** Bridge plot indicating the effects of improved performance and economic factors on production costs of ethylene [91].

As for economic circumstances, the most critical factor is the electricity price, as the cost of electricity accounts for the majority of the OPEX in every TEA considered. A low electricity price directly improves the economic feasibility of an electrolyser system. Additionally, the market price of the product sets the benchmark for the production costs of the process. High market prices could lead to better economic projections for CO<sub>2</sub>RR systems.

The other significant economic factor is the price of emitting CO<sub>2</sub> into the atmosphere, more specifically, the emission trading system (ETS). The ETS, a market-based approach to controlling pollution, offers economic incentives for the reduction of pollutant emissions, thereby making the emission of CO<sub>2</sub> increasingly costly for industries. By setting a price on carbon emissions, the ETS motivates industrial emitters to lower their carbon emissions. The implementation of the ETS is expected to boost the competitiveness of CO<sub>2</sub>RR technologies by elevating the costs associated with CO<sub>2</sub> emissions into the atmosphere [91, 94].

In previous work on TEA, ETS has been marked as a pathway for economic feasibility for gas-fed CO<sub>2</sub>RR systems as they have demonstrated significant reductions in CO<sub>2</sub> emissions when operated with energy from RES. In addition to TEA, Moreno et al. analyzed the net CO<sub>2</sub> emissions of a rWGS process, gas-fed CO<sub>2</sub>RR process, and a bicarbonate electrolysis process [93]. Results are displayed in Figure 2.13.

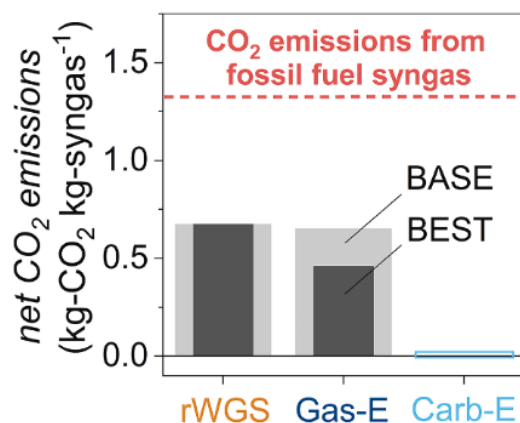


**Figure 2.13:** Carbon footprint of the three pathways to renewable syngas from DAC in the base case (light grey) and best case scenario (dark grey)[93].

This resulted in a significant reduction in CO<sub>2</sub> emissions compared to the fossil fuel-based processes. The bicarbonate electrolyser process showed a clear pathway towards a zero-emission balance but at the expense of a much higher green electricity demand than the other processes. This indicates that with the increase in CO<sub>2</sub> emission fees and greater availability of renewable energy, the bicarbonate system could have an economic advantage over other CO<sub>2</sub>RR methods.

# 3

## Methodology

This chapter presents the methodologies used to obtain the study's results. First, the research scope is defined, establishing the study's boundaries and objectives. Following this, five design cases are introduced to frame the analysis. The specifics of the models are then detailed, along with a discussion of the methods employed in the TEA for estimating OPEX and CAPEX.

### 3.1. Scope of research and design cases

The first step in the methodology is to define the research scope by establishing clear process boundaries. As outlined in section 1.1, a TEA of the integrated CCU system for syngas production is required. This scope includes both the capture column and the bicarbonate electrolyser, on which the TEA will be performed. The system is designed to operate with flue gas from the Energiron III DRI steelmaking process. Elements outside the scope of this study include potential pre-treatment of gas and liquid feed streams, waste product treatment, and downstream processing steps. The scope is visually represented by the orange dashed line in Figure 3.1.

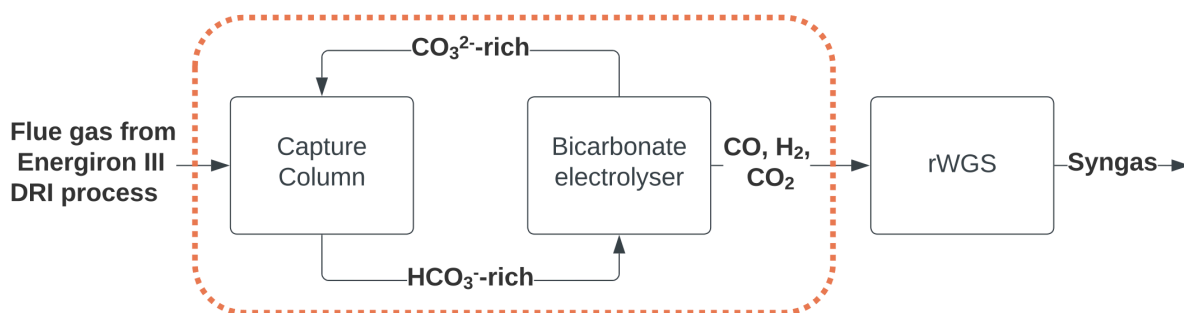


**Figure 3.1:** Schematic overview of the system: scope of thesis indicated by orange dotted line.

#### 3.1.1. Flue gas feed stream

As noted in chapter 1, steel producers in Europe are shifting away from coal-fueled processes and increasingly adopting DRI methods. For this reason, the gas feed stream in this study is based on the flue gas from an industrial-scale DRI process, specifically the Energiron III DRI process, as described by Bond et al. [27]. A portion of the total mass flow is utilized, with the selected size varying according to the process configuration. The composition of the flue gas is detailed in Table 3.1. For the purposes of this model, the mass flow rate, composition, and other properties of the flue gas are considered constant over time.

| <b>Stream Number</b>         | <b>26</b> |
|------------------------------|-----------|
| Vapour Fraction              | 1,0       |
| Temperature (°C)             | 106       |
| Pressure (kPa)               | 121       |
| Molar Flow (kgmole/h)        | 6957      |
| Mass Flow (t/h)              | 191,9     |
| <b>Species Mole Fraction</b> |           |
| H <sub>2</sub> O             | 0,2162    |
| CO <sub>2</sub>              | 0,1032    |
| O <sub>2</sub>               | 0,0201    |
| N <sub>2</sub>               | 0,6605    |

**Table 3.1:** Data for flue gas from Energiron III process stream 26 [27].

### 3.1.2. Operating conditions

For the integrated CCU system, the operating conditions play a critical role, as discussed in Figure 2.2.3 and subsection 2.3.3. These conditions significantly affect the performance of both the absorber column and the electrolyser. Elevated temperatures improve reaction kinetics in the absorption column and increase the  $FE_{CO}$  of the electrolyser. Increased pressure similarly benefits both pieces of equipment by improving gas solubility and reaction rates.

The absorption column, which utilizes  $K_2CO_3$  operates at elevated temperatures to facilitate efficient  $CO_2$  capture. These conditions improve the solubility of  $CO_2$  in the solvent and enhance the overall absorption rate. An additional advantage comes from the heat dissipated by the electrolyser, which can be used to heat the liquid flow in the absorption column, thus improving the overall system efficiency by utilizing waste heat.

Experimental data from Figure 2.7 indicate an optimal balance between residence time and temperature at 60°C, which is therefore chosen as the system's operating temperature. Additionally, commercial processes, such as the CAPSOL process, typically operate under pressures ranging from 5 to 12 bar. Pressurizing beyond 10 bar would significantly increase compression costs and necessitate more advanced, pressure-resistant equipment, driving up CAPEX [95]. Consequently, an operating pressure of 10 bar is chosen as a trade-off between system performance and economic feasibility.

### 3.1.3. Reverse water-gas shift

The electrolyser outflow contains both liquid and gas-phase compounds. The liquid phase primarily consists of the  $CO_3^{2-}$ -rich solvent, while the gas phase contains CO, produced as a result of the  $CO_2RR$ ,  $H_2$  from the HER, and a significant amount of unreacted  $CO_2$ . The high  $CO_2$  concentration renders the syngas unsuitable for immediate use, necessitating a downstream processing step. To maximize syngas yield and eliminate  $CO_2$  waste streams, the unreacted  $CO_2$  can be reacted with  $H_2$  through the reverse water-gas shift (rWGS) reaction, as shown in Equation 3.1.



In the integrated CCU system, unreacted  $CO_2$  in the product stream reacts with  $H_2$  produced by HER in the rWGS reaction. This process converts unwanted  $CO_2$  to CO, thereby increasing the syngas yield and eliminating  $CO_2$  waste streams. As  $H_2$  is consumed and CO is produced, the syngas ratio is significantly altered. To compensate for this change, the design ratio must be adjusted by increasing the  $H_2$  concentration in the feed stream to achieve the desired syngas composition after the rWGS reaction. A primary drawback of the rWGS reaction is its high-temperature requirement, typically between 700°C and 900°C, which makes it energy-intensive [96]. The design of the rWGS reactor itself is considered out of scope for this work.

### 3.1.4. Cases I, II, III, IV and V

This section defines five different cases for the production of syngas through the integrated system. A detailed schematic overview of every case can be found in Figure A.4 to Figure A.8.

The mass flow of the flue gas, as seen in subsection 3.1.1, is significantly larger compared to the capacity of current state-of-the-art electrolyzers. Therefore, for realistic sizing, the 20 MW Cummins PEM electrolyser module recently installed in Canada is used as a reference for sizing the bicarbonate electrolyser [97]. The five cases are sized to match this 20 MW capacity, meaning only a fraction of the total flue gas mass flow is used as input, depending on the case.

#### Case I: 90 wt% CO<sub>2</sub> capture

For Case I, a 90wt% capture rate of CO<sub>2</sub> is considered. This means that 90wt% of the molar flow of CO<sub>2</sub> present in the flue gas is converted to (bi)carbonate ions in the absorption column, while the remaining 10wt% is emitted through the gas outflow. A starting point of pH = 11,5 is fixed for the solvent inflow. From here, the pH step required for 90wt% capture is determined. The column is further optimized based on this pH step to meet the case requirements. The resulting HCO<sub>3</sub><sup>-</sup>-rich liquid outflow will serve as feedstock for the bicarbonate electrolyser, which is optimized to reverse the pH shift from the absorption column.

#### Case II: syngas production for the Fischer-Tropsch Process

Case II aims to optimize the system for producing syngas suitable for the Fischer-Tropsch (FT) process, a widely used method for converting syngas into diesel. The target syngas ratio for this process is 2:1 (H<sub>2</sub>:CO). The initial point is an electrolyser inflow with pH = 8,5, from which the pH step is adjusted until the desired syngas ratio is achieved. Since an rWGS reaction follows the electrolyser, the syngas ratio is increased to meet the 2:1 design specification at the rWGS reactor exit. Subsequently, the absorption column is optimized to handle the reverse pH step.

#### Case III: high Faradaic Efficiency (FE<sub>CO</sub> > 50%) operation

Case III aims to produce syngas with a low syngas ratio by operating the electrolyser at a high FE<sub>CO</sub>. At higher pH levels, the FE<sub>CO</sub> drops significantly, resulting in a higher syngas ratio due to increased H<sub>2</sub> production. To prevent this, high pH levels are avoided, and only a small pH step is applied. The starting pH is fixed at pH = 8,5, after which a Python script is used to determine the pH step where the FE<sub>CO</sub> reaches 50%. The pH step is defined as pH = 8,5 ↔ pH at 50% FE<sub>CO</sub>, and the syngas ratio is left non-fixed in this case. The absorption column is optimized accordingly.

#### Case IV: Syngas production for the Energerion III process

Case IV focuses on optimizing the system for syngas production suitable for the Energerion III process. The composition of the syngas feed stream entering the EAF, shown in Table 3.2, corresponds to a syngas ratio of 4,1:1:0,4 (H<sub>2</sub>:CO:CO<sub>2</sub>). The pH step starts at pH = 8,5 and continues until the desired syngas ratio is achieved. The goal is to achieve a gas outflow with the appropriate syngas ratio for feeding into the EAF. Note that a small amount of CO<sub>2</sub> may remain in the stream, which does not need to be removed via rWGS.

| Stream Number         | 17     |
|-----------------------|--------|
| Vapour Fraction       | 1,0    |
| Temperature (°C)      | 962    |
| Pressure (kPaa)       | 725    |
| Molar Flow (kgmole/h) | 18692  |
| Mass Flow (t/h)       | 192,7  |
| Species Mole Fraction |        |
| CH <sub>4</sub>       | 0,0831 |
| H <sub>2</sub> O      | 0,0296 |
| CO                    | 0,1619 |
| CO <sub>2</sub>       | 0,0502 |
| H <sub>2</sub>        | 0,6623 |
| N <sub>2</sub>        | 0,0129 |

**Table 3.2:** Data for Stream 17: feed stream for EAF in Energiron III process [27].

### Case V: Intermediate pH step

In Case V, the objective is to model a system with an intermediate pH step to explore optimization opportunities. The system operates within a fixed pH range of  $\text{pH} = 9,0 \leftrightarrow \text{pH} = 10,5$ , while the syngas ratio is allowed to vary. The focus is on achieving an optimal balance between improving the efficiency of the capture column and optimizing the bicarbonate electrolyser. The study aims to identify the trade-off point that results in the best overall system performance or to determine if no such point exists.

## 3.2. Electrolyser model

To estimate the costs of the integrated process, the bicarbonate electrolyser is modelled in Microsoft Excel. The model uses three types of inputs: absorption column-dependent inputs, pH-dependent inputs, and constants. A schematic view of the model is shown in Figure 3.2.

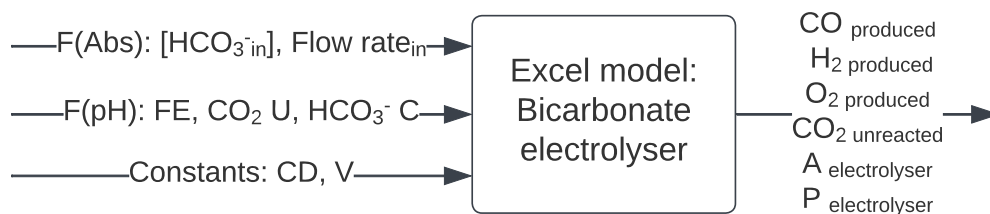


**Figure 3.2:** Schematic overview of the electrolyser model with inputs and outputs.

A more detailed overview of the input and output parameters, along with their units, is displayed in Table A.2. This section provides an in-depth explanation of the model for the integrated CCU system and discusses the input parameters used to generate the results.

### 3.2.1. Model description

The electrolyser model is constructed as follows: The number of available electrons per square meter is calculated using the current density. The amounts of H<sub>2</sub> and CO produced from the CO<sub>2</sub>RR are determined by multiplying the available electrons by their respective FE values, FE<sub>H<sub>2</sub></sub> and FE<sub>CO</sub>. Since CO<sub>2</sub> is reduced to CO in a 1:1 ratio, the amount of CO<sub>2</sub> generated at the BPM can be calculated. Using the concentration of HCO<sub>3</sub><sup>-</sup>, the required conversion can be determined. Once all parameters

are known, the required power, electrode area, and the amounts of  $O_2$ ,  $CO$ , and  $H_2$  produced can be calculated. In addition, the  $CO_2$  utilization ratio is known, so the amount of unreacted  $CO_2$  can be calculated from the amount of  $I-CO_2$ . A detailed overview of the constants and formulas used can be found in subsection A.5.1 and subsection A.5.2, respectively.

### pH steps

As discussed in subsection 2.2.3, the electrochemical performance of the bicarbonate electrolyser is strongly dependent on the pH of the liquid inflow. Recent work from Burgers has confirmed this [98]. This means that a single value for  $FE_{CO}$  and  $CO_2$  utilization ratio cannot be used. Instead, a range of data points corresponding to different pH levels must be considered, and the model must be divided into smaller pH steps, each with its own input parameters. For this model, a pH step size of 0,5 is considered. Within each pH step, the input parameters remain constant, and for larger pH variations, additional steps are added to the model, each with its own input parameters.

### 3.2.2. pH-dependent model inputs: $FE_{CO}$ and $CO_2$ utilization ratio

Next, the input parameters have to be chosen. Zhang et al. demonstrated a strong dependence between pH and electrolyser performance. Recent work by Burgers et al. further explored this relationship through laboratory experiments [98]. In these experiments,  $KHCO_3$  solutions with varying pH levels were run through a bicarbonate electrolyser at a fixed current density of  $100 \text{ mA/cm}^2$  under ambient conditions ( $20^\circ\text{C}$ , 1 bar), with interdigitated flow plates. The  $CO_2$  utilization ratio,  $FE_{CO}$ , and system stability were reported. The results are displayed in Figure 3.3.

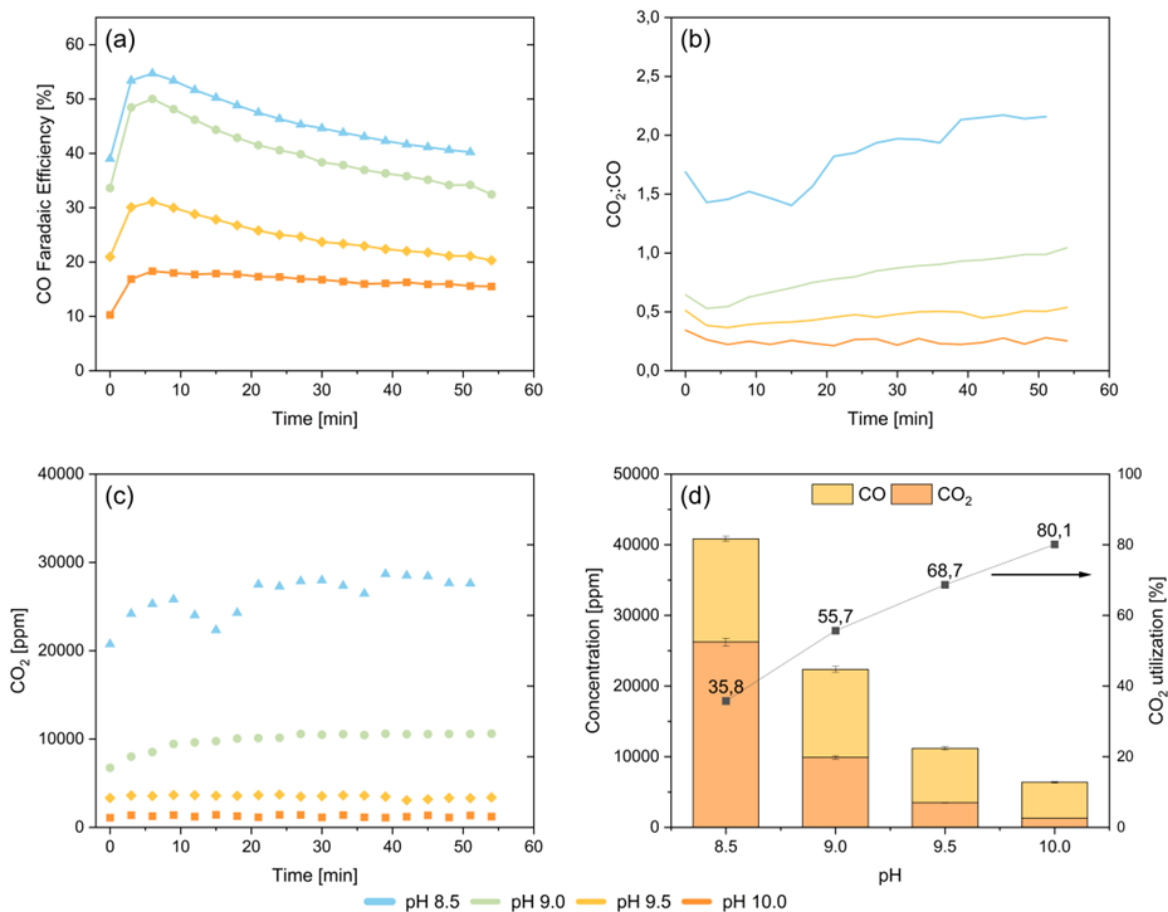


**Figure 3.3:** a)  $FE_{CO}$  over time, b)  $CO_2:CO$  ratio over time, c)  $CO_2$  concentration in the gas compartment over time, d)  $CO_2$  utilization ratio for 4 pH levels [98].

From these results, it can be concluded that  $FE_{CO}$  decreases with increasing pH, while  $CO_2$  utilization

ratio increases as the pH rises. Although this provides useful data for the input parameters of the Excel model, the results cannot be directly applied because the operating conditions in the experiments (ambient conditions) differ from those of the integrated system, which operates at elevated temperature and pressure (as discussed in Figure 3.2.2). Additionally, results for higher pH levels (pH = 10,5, 11,0, 11,5) are extrapolated from the experimental data, assuming linear behaviour.

#### Values for $FE_{CO}$ and $CO_2$ utilization on the operating conditions

As mentioned in subsection 3.2.2, the experimental data cannot be directly applied to the model because the operating conditions differ. As described in subsection 2.2.3, these parameters depend on pressure, temperature, and current density. Specifically, the  $FE_{CO}$  increases with rising pressure and temperature but decreases with increasing current density. Additionally, research has shown that as more  $i-CO_2$  is generated,  $CO_2$  utilization ratio decreases. Work by Zhang et al. demonstrated that higher temperatures and pressures result in greater  $CO_2$  liberation within the system, thus lowering overall  $CO_2$  utilization ratio, as a larger fraction of  $CO_2$  exits the electrolyser unreacted [66].

Zhang et al. employed a similar bicarbonate electrolyser setup (porous Ag cathode, Ni foam anode, and interdigitated flow plate), and operated at the same potential (3,6 V) and current density (100 mA/cm<sup>2</sup>) under ambient conditions [66]. However, their tests were performed at a fixed pH. As seen in Figure 3.3, changes in pH significantly impact system performance, influencing both the  $CO_2RR$  and the carbonate/bicarbonate equilibrium within the cell. While the specific effects of pH, temperature, and pressure still require further exploration and experimental validation, this work assumes that the experiments by Burgers et al. (at pH = 8,5, 9,0, 9,5, and 10,0) exhibit similar dependencies on temperature and pressure as those reported by Zhang et al [98]. This assumption, however, requires confirmation through experimental data.

The operating conditions of the electrolyser are 10 bar and 60°C. Since no experimental data is available for  $FE_{CO}$  and  $CO_2$  utilization ratio under these specific conditions—and conducting experiments would require a pressurized bicarbonate electrolyser setup—the input values must be estimated by applying correction factors to parameters obtained under ambient conditions. These factors are estimated based on the observed effects of pressure and temperature on  $FE_{CO}$  and  $CO_2$  utilization ratio, as discussed in subsection 2.2.3. Additionally, a sensitivity analysis is conducted, providing worst-case, base-case, and best-case scenarios. The correction factors are displayed in Table 3.3.

| Parameter                | Worst Case Factor | Base Case Factor | Best Case Factor |
|--------------------------|-------------------|------------------|------------------|
| $FE_{CO}$                | 1,1               | 1,3              | 1,5              |
| $CO_2$ utilization ratio | 0,7               | 0,8              | 0,9              |

**Table 3.3:** Multiplication factors for estimating input parameters at elevated temperatures and pressures (10 bar, 60°C).

### 3.2.3. pH-step dependent model input $HCO_3^-$ conversion

To achieve the desired pH levels, a specific percentage of the  $HCO_3^-$  molecules must be converted to  $CO_2$ . This required conversion percentage can be determined using the Bjerrum plot under the given system conditions.

#### Bjerrum plot

The conversion percentage of  $HCO_3^-$  can be determined using the Bjerrum plot, which illustrates the equilibrium mole ratios of  $CO_3^{2-}$ ,  $HCO_3^-$ , and  $CO_2$ . Figure 3.4 presents the Bjerrum plot under ambient conditions, including the  $pK_1$  and  $pK_2$  values. However, these values vary with changes in temperature and pressure, which affects the plot under elevated conditions. The values used in the model are derived from experimental data by Plummer et al. and are listed in Table A.3 [99]. The dotted line on the plot indicates the  $pK_a$  values under the system conditions (10 bar, 60°C).

To determine the required percentage conversion of  $HCO_3^-$  for each pH step, the concentration of  $HCO_3^-$  at specified pH intervals is obtained from the plot, and the percentage decrease is then calculated. This calculation is based on the formula presented in Equation 3.2. A Python script is used to extract the  $HCO_3^-$  concentrations at specific pH values. The script, which includes the formulas used to generate this plot, is available in subsection A.4.1.

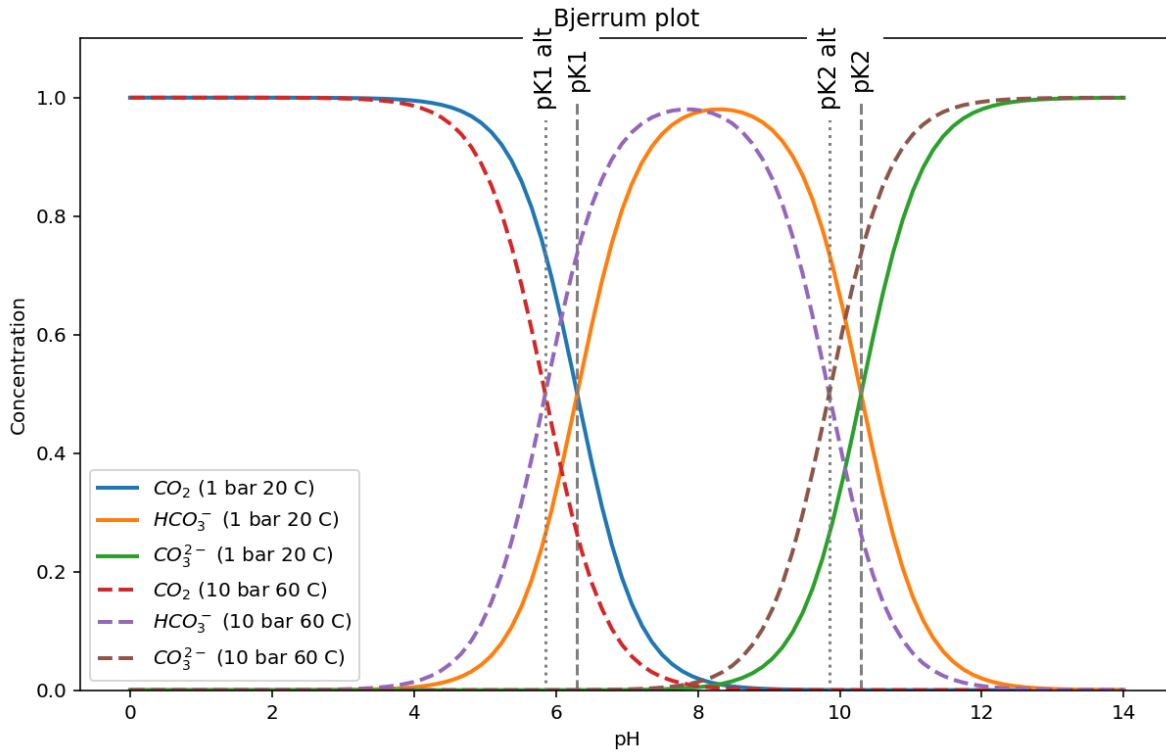


**Figure 3.4:** Bjerrum plot for ambient conditions (1 bar, 25°C) and system conditions (10 bar, 60°C).

The required percentage of  $\text{HCO}_3^-$  conversion for each pH step is determined by reading the  $\text{HCO}_3^-$  concentration at the specified pH intervals and calculating the percentage decrease. This calculation is based on the formula shown in Equation 3.2.

$$\text{Required conversion from } i \rightarrow j = \frac{\text{Mole fraction at } \text{pH}_i - \text{Mole fraction at } \text{pH}_j}{\text{Mole fraction at } \text{pH}_i} \quad (3.2)$$

### 3.2.4. Model constants

The final parameters for the Excel model are those independent of the pH step or absorption column configuration, namely the current density and applied potential.

For current density, a trade-off exists: at low current densities, the electrolyser's area must become significantly larger relative to the inflow, resulting in higher CAPEX. There is a general consensus that commercially relevant current density begins at 50 to 100 mA/cm<sup>2</sup> [100]. However, as the CD increases, the  $\text{FE}_{\text{CO}}$  decreases (discussed in subsection 2.2.3). Therefore, most experimental data is generated at a CD of 100 mA/cm<sup>2</sup>, which is also used as the basis for the pH-dependent data in the model. As a result, the current density is set at 100 mA/cm<sup>2</sup> throughout the model.

The applied potential is considered in the sensitivity analysis. A lower applied voltage reduces power consumption; however, the electrolyser must still overcome the energy barrier and the associated overpotential. Experimental results are typically obtained at potentials ranging from 3,3 V to 4,0 V. For the analysis, values of 3,3 V, 3,6 V, and 3,9 V are used to represent the worst, base, and best-case scenarios, respectively.

## 3.3. Rate-based model for capture column

For modelling the absorption column, ASPEN PLUS V11 process modeling software is employed. The thermodynamic model selected is the ELECNRTL model, which is particularly useful for systems involving electrolytes and mixed solvent-electrolyte solutions, as is the case in this application.

### 3.3.1. Equilibrium vs. rate-based model

For the capture column model a decision must be made between equilibrium-based and rate-based modeling. An equilibrium-based model calculates the maximum possible capture based on the specified equilibrium reactions and their reaction constants. With given flow rates, the interactive sizing tool can be used to estimate the column's size. The main advantages of an equilibrium-based model are its ease of implementation, speed, and ability to predict maximum performance.

In a rate-based model, the user determines the column size, and the reaction may not necessarily reach equilibrium. In smaller capture columns, some of the solvent may pass through unreacted, leading to a smaller, but more realistic, capture fraction compared to an equilibrium-based model. A rate-based model is more complex and requires a deeper understanding of the process, but it tends to provide a more realistic estimation of performance.

Given that the Benfield process is characterized by slow kinetics (see subsection 2.3.2 and subsection A.6.2), it is unlikely that equilibrium will be reached within a reasonable timeframe, or achieving it would require an impractically large capture column. An equilibrium-based model would significantly overestimate the performance since it calculates the maximum possible capture. Hence, for this reason, the rate-based model is chosen for this application.

### 3.3.2. Capture column design parameters

For this purpose, a 10-stage packed absorption column with RASiCH packing is used. To accelerate the capture process, the column operates under elevated pressure and temperature (10 bar, 60 °C). This enables faster capture and allows for a more compact column design, as discussed in subsection 3.1.2. The approach to flood is a critical design parameter: if the approach to flood is too high, the column becomes undersized and risks overflowing; if it is too low, the column is oversized relative to the flow, resulting in unnecessary costs. The column is designed with a 70% approach to flood and a  $\pm 10\%$  error margin, giving a maximum of 80% approach to flood.

The chemical reactions, reaction constants, and a detailed description of the absorption column internals can be found in Table A.15 and subsection A.6.2. Based on these reactions, the height and diameter of the column can be iterated to achieve the desired pH and outflow while staying within the approach to flood range. A larger column allows for greater CO<sub>2</sub> capture but results in higher CAPEX, while a smaller column reduces CO<sub>2</sub> capture and lowers CAPEX.

### 3.3.3. ASPEN model validation

After constructing the ASPEN model for the capture column, its performance must be validated against in-field data to ensure accuracy. In this work, two key parameters are considered: CO<sub>2</sub> capture fraction and solvent loading. The CO<sub>2</sub> capture fraction represents the weight percentage of CO<sub>2</sub> captured by the solvent. For this study, the CAPSOL Hot Potassium Carbonate (HPC) process is used as a reference, which reports capture ratios along the height of the absorption column. A capture ratio of 90wt% over a column height of 20 meters is considered realistic under operating conditions of 5–8 bar (see Figure A.9). Solvent loading is defined as the mole ratio of K<sub>2</sub>CO<sub>3</sub> inflow to reacted CO<sub>2</sub>. Smith et al. modelled Benfield process absorber performance at various temperatures in ASPEN and validated their results with experimental data from an absorption column [82]. Their findings showed a CO<sub>2</sub> loading of 40% on a molar basis, which is considered a realistic solvent loading for the absorption column in this model. The performance of the absorption column is validated using these two metrics.

## 3.4. Recycle streams

One of the primary advantages of the integrated system is the ability to recycle the K<sub>2</sub>CO<sub>3</sub> solvent multiple times, which significantly reduces the OPEX on raw materials. However, in practical scenarios, the feed stream will contain impurities, and some losses are inevitable. To maintain operational efficiency, a portion of the liquid stream must be periodically purged and replaced with fresh solvent to offset these losses.

As outlined in subsection 2.3.1, the common impurities include H<sub>2</sub>S, COS, SO<sub>2</sub>, and NO<sub>3</sub>. In the Energerion III process, these impurities are present in smaller quantities compared to coal-based steelmaking processes. Given that these impurities are predominantly in the gas phase at the operating conditions,

most will exit the system through the gas compartment of the electrolyser outflow, thereby limiting their buildup in the liquid stream [101]. However, it is reasonable to assume that a small fraction of these impurities will remain in the aqueous phase of the liquid outflow, potentially leading to accumulation over time.

To manage the recycle efficiency and minimize impurity buildup, we assume a maximum allowable impurity concentration in the liquid stream of 200 ppm for cumulative impurities. To quantify the recycle efficiency, a recycle factor  $R$  is introduced. Solving the mass balance for the integrated system with respect to  $R$  yields the following equation:

$$R < \frac{C_{\max} - (C_{\text{in}} \times \text{fraction of impurities in aqueous phase})}{C_{\max}}$$

where  $C_{\max}$  represents the maximum allowable impurities concentration, and  $C_{\text{in}}$  denotes the concentration of impurities in the solvent inflow. For estimating the OPEX related to raw materials, the following assumptions are made:

- $C_{\max} = 200$  ppm
- $C_{\text{in}} = 50$  ppm
- fraction of impurities in aqueous phase = 0, 1

Different impurity specifications may be applied to each syngas product based on specific process requirements. Note that the concentration of impurities also affects the electrolyser's performance, as discussed in Figure 2.2.3, but is not considered in this work.

## 3.5. Cost estimation

This section discusses the methodology of the TEA and includes the methods used to calculate CAPEX, OPEX, LCOS of syngas, and the cost per kg of CO produced.

### 3.5.1. OPEX

The OPEX is estimated using the methodology outlined in the recent work by Alerte et al. [11]. The annual OPEX, in USD, can be calculated using Equation 3.3.

$$\text{OPEX}_i = \text{OPEX}_{\text{RM}} + \text{OPEX}_{\text{E}} + \text{OPEX}_{\text{U}} + \text{OPEX}_{\text{CM}} + \text{OPEX}_{\text{FC}} + \text{OPEX}_{\text{IC}} \quad (3.3)$$

Where:

- $\text{OPEX}_i$  = total annual OPEX
- $\text{OPEX}_{\text{RM}}$  = raw material costs (e.g., solvent inflow, fresh electrolyte)
- $\text{OPEX}_{\text{E}}$  = electricity costs for the electrolyser
- $\text{OPEX}_{\text{U}}$  = utility costs of the system (e.g., compressor, pump, absorption column)
- $\text{OPEX}_{\text{CM}}$  = consumable costs (e.g., catalysts)
- $\text{OPEX}_{\text{FC}}$  = fixed costs (e.g., insurance, labor)
- $\text{OPEX}_{\text{IC}}$  = investment-related expenses

Start-up or system fill costs are not included in this analysis. A detailed description of this calculation and the economic assumptions can be found in Table A.19, and the Excel model for the full OPEX calculations is available in the supplementary materials.

### 3.5.2. Levelized Cost of Syngas (LCOS) normalized to Lower Heating Value (LHV)

To effectively compare different cases with one another, as well as with data from other fuels and power-to-fuel systems, a universal metric must be established. Previous studies have utilized the LCOS for this purpose, representing the cost of syngas production per kilogram. However, this LCOS does not

account for the varying syngas composition in each case. Therefore, the LCOS is normalized to the LHV of the mixture.

The LHV of a fuel is defined as the amount of heat released during the combustion of a specified quantity (initially at 25°C or another reference state) when the combustion products are cooled to 150°C [102]. LHV is typically expressed in megajoules per kilogram (MJ/kg). To calculate the LHV of a syngas mixture, the mass fractions of each component must be considered, as shown in Equation 3.4. In this equation,  $x_i$  represents the mass fraction of component  $i$ , and  $LHV_i$  is the LHV of component  $i$ . Pure CO has an LHV of 10,1 MJ/kg, pure H<sub>2</sub> has an LHV of 119,6 MJ/kg [103].

$$LHV_{\text{mix}} = \sum_{i=1}^n x_i \cdot LHV_i \quad (3.4)$$

The LCOS divided by the LHV of the syngas yields the  $LCOS_{LHV}$ , expressed in US dollars per megajoule (\$/MJ), as shown in Equation 3.5. A lower  $LCOS_{LHV}$  indicates a higher caloric output per dollar.

$$LCOS_{LHV} = \frac{LCOS}{LHV_{\text{mix}}} \quad (3.5)$$

Since H<sub>2</sub> has a higher LHV, the calculation of  $LCOS_{LHV}$  favours the production of syngas with higher H<sub>2</sub>/CO ratios, as the larger proportion of H<sub>2</sub> increases the overall caloric value. However, the molar mass of H<sub>2</sub> (2,016 g/mol) is significantly lower than that of CO (28,01 g/mol), which means that on a molar basis, the influence of H<sub>2</sub> is less pronounced in terms of mass. An overview of syngas compositions with different molar and weight ratios, along with their corresponding LHV values, is provided in Table 3.4.

| Syngas Mole Ratio H <sub>2</sub> /CO | Weight Ratio H <sub>2</sub> /CO | LHV [MJ/kg] |
|--------------------------------------|---------------------------------|-------------|
| 1:1                                  | 1:14                            | 17,5        |
| 2:1                                  | 1:7                             | 23,9        |
| 3:1                                  | 3:14                            | 29,6        |
| 4:1                                  | 2:7                             | 34,7        |
| 5:1                                  | 5:14                            | 39,2        |

**Table 3.4:** Syngas mole ratio H<sub>2</sub>/CO, corresponding weight ratio, and LHV.

Table B.2 provides an overview of production costs, LHV, and  $LCOS_{LHV}$  for various products. The closest competitors to the integrated CCU system are other electrolysis methods, such as power-to-gas, gas-fed CO<sub>2</sub>RR, and H<sub>2</sub> electrolysis. The bicarbonate electrolysis data presented is based on literature for a similar electrolyser configuration.

### 3.5.3. CAPEX

This section discussed the methodology for CAPEX estimation for the key equipment involved in the process, including the electrolyser, absorption column, flue gas compressor, and solvent pump.

#### electrolyser CAPEX

To estimate the CAPEX of the electrolyser, the cost per square meter of the membranes is first calculated. The electrolyser comprises the MEA, the applied catalyst, and the BPM. The cost per  $m^2$  is then multiplied by the required electrolyser area, which is determined from the electrolyser model. A Balance of Plant (BoP) factor is applied to account for additional equipment costs, including piping, flow plates, frameworks, and other components associated with the electrolyser.

According to recent work by Verboon et al., the electrolyser system accounts for approximately 30% of the unit capital cost (UCC), while the balance of plant (BoP) comprises another 30% [104]. The remaining 40% is attributed to owner's costs, indirect costs, and contingency, which are factored in through the UCC factor. These ratios were used as guidelines in selecting the BoP and UCC factors

for the CAPEX estimation. Equation 3.6 shows the formula used for the UCC calculation. A more detailed overview of the calculation can be found in Table A.17.

$$\text{UCC} = \left( \text{Area} \times \frac{\text{stack cost}}{\text{m}^2} \right) \times \text{BoP factor} \times \text{UCC factor} \quad (3.6)$$

The costs for the catalyst are calculated separately, as shown in Table A.18, and are then incorporated into the overall CAPEX calculation, as detailed in Table A.17. The values used are based on the work of Moreno et al. [93]. These results stem from 2024, so they are not adjusted with a CEPCI index.

#### Comparison of electrolyser CAPEX

The bicarbonate electrolyser's main competitors are gas-fed electrolysers for CO<sub>2</sub>RR and electrolysers used for green H<sub>2</sub> production. To facilitate a fair comparison between the CAPEX of the bicarbonate electrolyser and H<sub>2</sub> electrolysers, the CAPEX is normalized to the rated power and expressed in US-D/kW. The data provided represent UCC, which accounts for the entire electrolyser unit, including the core system, balance of plant, peripheral equipment and other non-material CAPEX factors.

The table below presents data on H<sub>2</sub> electrolyser units along with their respective costs per kWh. These figures were drawn from the recent work of Verboon et al. [104]. It is important to note that no distinction was made between alkaline and PEM electrolysers in this study, and SOEC electrolysers were not included. Furthermore, it should be highlighted that alkaline electrolysers generally have lower costs compared to PEM electrolysers, due to the more expensive membranes and catalysts required in PEM systems [105].

| Source                         | Ref. year | UCC [\$/kW] | References |
|--------------------------------|-----------|-------------|------------|
| TNO (2024)                     | 2024      | 3203        | [104]      |
| Berenschot & TNO (2023)        | 2023      | 2310        | [106]      |
| EU Hydrogen Observatory (2024) | 2022      | 1313        | [107]      |
| Wood Mackenzie (2023)          | 2023      | 1911        | [108]      |
| CE Delft & TNO (2023)          | 2030      | 1796        | [109]      |

**Table 3.5:** Comparison of UCC (USD) across different studies for H<sub>2</sub> electrolysers (Euro converted to USD).

#### CAPEX normalized to CO production

When comparing electrolysers for CO<sub>2</sub>RR, it is important to use a metric that accounts for both H<sub>2</sub> and CO products generated and their respective production ratios. A commonly used metric is the CAPEX per ton of CO produced, expressed as \$/t CO. To make a fair comparison, the same components of the electrolyser have to be considered. For this reason, the UCC is used, normalized by the CO production in tonnes. The comparison data have been adjusted using the same factors as in Table A.17 to ensure consistency. Table 3.6 provides data from the literature on CO<sub>2</sub>RR systems.

| Source | Case         | UCC/t CO [\$/t CO] | Reference |
|--------|--------------|--------------------|-----------|
| Moreno | Carb-E base  | 2004               | [93]      |
| Moreno | Gas-fed base | 603                | [93]      |
| Jouny  | Gas-fed base | 405                | [29]      |
| Jouny  | Gas-fed best | 203                | [29]      |

**Table 3.6:** Comparison data of UCC per ton of CO for bicarbonate and gas-fed electrolysers.

#### Absorption column, compressor, and pump CAPEX

CAPEX estimation for the designed process was conducted using Aspen Economic Analyzer (AEA) version 11.0, a widely recognized tool for integrating process simulation and cost analysis. Process data, including equipment sizes and flow rates, were directly imported from Aspen Plus simulations. The AEA calculated CAPEX based on both direct costs (e.g., equipment purchase and installation) and indirect costs (e.g., engineering and construction overheads).

The cost extracted from AEA was based on economic data from its 2022 database. To reflect current pricing, the values were adjusted using the Chemical Engineering Plant Cost Index (CEPCI) for 2024. CEPCI values were sourced from ChemEngOnline [103]. The final price considered in the TEA represents the installed cost of the equipment.

## 3.6. CO<sub>2</sub> emissions

This section outlines the methodology for the CO<sub>2</sub> emissions analysis, aimed at providing insight into the CO<sub>2</sub> emissions savings of the integrated CCU system.

### 3.6.1. CO<sub>2</sub> captured by the system

The CCU system is designed to reduce CO<sub>2</sub> emissions by capturing and converting CO<sub>2</sub> into syngas, thus preventing its release into the atmosphere. However, this conversion process requires energy, which can lead to new CO<sub>2</sub> emissions depending on the energy source used. The net CO<sub>2</sub> savings of the system can be calculated using Equation 3.7, with kg/year as unit.

$$\text{CO}_2 \text{ saved} = \text{CO}_2 \text{ converted} - \text{CO}_2 \text{ new emissions} \quad (3.7)$$

In this equation, CO<sub>2</sub> converted refers to the amount of CO<sub>2</sub> captured and converted into syngas, while CO<sub>2</sub> new emissions accounts for the emissions associated with the energy consumed by the CCU system. The overall CO<sub>2</sub> reduction efficiency depends on both the conversion process efficiency and the carbon intensity of the energy source used. Notably, this analysis only considers emissions within the scope of the project and excludes potential CO<sub>2</sub> emissions from the subsequent combustion of the syngas or the rWGS reaction.

### 3.6.2. CO<sub>2</sub> emissions resulting from energy production

The CO<sub>2</sub> emissions generated by the energy consumption of the system are calculated as follows. First, the total energy usage of the system is determined using Equation 3.8:

$$E_{\text{total}} = E_{\text{electrolyser}} + E_{\text{flue gas compressor}} + E_{\text{pump}} + E_{\text{absorber column}} \quad (3.8)$$

where energy values are expressed in megawatt-hours per year (MWh/year). The amount of CO<sub>2</sub> emitted depends on the energy source used. Table 3.7 lists various energy sources along with their corresponding CO<sub>2</sub> emissions in kilograms of CO<sub>2</sub> per megawatt-hour (kg CO<sub>2</sub>/MWh). Preliminary estimations show that using energy from fossil fuel sources results in more CO<sub>2</sub> emissions than are saved, thus only renewable energy sources are considered in this analysis. Specifically, a 100% wind energy source and a 50%/50% mix of solar and wind are evaluated. An overview of energy sources and their respective CO<sub>2</sub> emissions per MWh is displayed in Table 3.7.

| Energy Source                     | kg CO <sub>2</sub> /MWh |
|-----------------------------------|-------------------------|
| Coal                              | 820                     |
| Nuclear                           | 12                      |
| Wind                              | 12                      |
| Solar                             | 41                      |
| Coal with CCS                     | 200                     |
| Gas                               | 490                     |
| Solar and Wind Combined (50%/50%) | 26,5                    |

**Table 3.7:** IPCC data on CO<sub>2</sub> emissions from different energy sources [29].

Although wind and solar energy are classified as renewable, they still result in some CO<sub>2</sub> emissions due to factors such as maintenance, material production, and infrastructure construction [29]. The total CO<sub>2</sub> emissions resulting from the system's energy consumption can be calculated using Equation 3.9.

$$\text{CO}_2 \text{ emissions from energy production} = E_{\text{total}} \times \frac{\text{CO}_2 \text{ emissions}}{\text{MWh}} \quad (3.9)$$

### 3.7. Sensitivity Analysis

A sensitivity analysis is subsequently conducted to evaluate how the TEA outcomes vary under worst-case, base-case, and best-case scenarios. This analysis considers both economic and technical parameters. The base case is designed to reflect state-of-the-art conditions.

#### Technical parameters

First, the potential is varied. This depends on the specific setup and the amount of overpotential required, which directly influences the system's power consumption. Next, the correction factors, as discussed in Figure 3.2.2, are applied. These factors estimate the increase in  $FE_{\text{CO}}$  and the decrease in  $\text{CO}_2$  utilization ratio under the operational conditions (60°C, 10 bar), compared to the ambient conditions (20°C, 1 bar) where the original values were obtained. Lastly, the durability of the catalyst layer is varied. This refers to the operational time before the catalyst layer becomes non-functional and requires replacement. Since the layer degrades over time, it is considered a consumable. The values for durability are derived from Moreno et al., and the technical parameters are displayed in Table 3.8 [93].

| Technical parameter                    | Worst | Base | Best  | Unit |
|--|-------|------|-------|------|
| Cell potential                         | 3,9   | 3,6  | 3,3   | V    |
| $FE_{\text{CO}}$ factor                | 1,1   | 1,3  | 1,5   | [-]  |
| $\text{CO}_2$ utilization ratio factor | 0,7   | 0,8  | 0,9   | [-]  |
| Durability of catalyst layer           | 4000  | 8000 | 16000 | hr   |

**Table 3.8:** Technical parameters used in sensitivity analysis.

#### Economic parameters

As seen in section 2.5, the electricity price greatly influences the economic performance of a  $\text{CO}_2\text{RR}$  system. This parameter is accounted for in the sensitivity analysis. Additionally, the price of raw materials, including the solvent and KOH electrolyte, is considered, as these are expected to constitute a significant portion of OPEX. A lifetime of 20 years and an interest rate of 10% are also assumed, along with a runtime of 8000 hours per year, accounting for approximately 10% downtime. These parameters are displayed in Table 3.9.

| Economical Parameters            | Worst | Base | Best | Unit               |
|----------------------------------|-------|------|------|--------------------|
| Electricity Price                | 90    | 60   | 30   | \$/MWh             |
| Price of $\text{K}_2\text{CO}_3$ | 1,8   | 1,4  | 1,0  | \$/kg              |
| Price of KOH                     | 0,2   | 0,15 | 0,1  | \$/L (1M solution) |
| OPEX FC Factor                   | 0,11  | 0,09 | 0,07 | -                  |
| Peripheral Equipment Factor      | 2,4   | 2,0  | 1,6  | -                  |
| UCC Factor                       | 1,4   | 1,65 | 1,9  | -                  |
| Lifetime                         | 20    | 20   | 20   | years              |
| Interest Rate                    | 10    | 10   | 10   | %                  |
| Runtime                          | 8000  | 8000 | 8000 | hrs/year           |

**Table 3.9:** Economical parameters used in sensitivity analysis.

# 4

## Results & Discussion

This section presents the results following from the methodology outlined in chapter 3. A techno-economic analysis was conducted using an Excel model of the bicarbonate electrolyser, coupled with an ASPEN PLUS model of the absorption column. The system was optimized across various case scenarios. Additionally, a sensitivity analysis was performed to evaluate the system's performance under worst-case, base-case, and best-case conditions.

### 4.1. pH steps and capture fractions

The first step in addressing the research questions is determining the pH required to meet the case-specific design goals. Figure 4.1 illustrates the pH steps required for the five base cases outlined in subsection 3.1.4. The lower pH value (on the left) represents the pH of the inflow to the electrolyser, while the higher pH value (on the right) represents the inflow to the solvent in the absorption column. The figure illustrates the pH steps and their CO<sub>2</sub> capture fractions ( $C_f$  (wt%)) for the base cases. In the worst case, the pH is slightly lower than in the base case, while in the best case, the pH is slightly higher. Specific pH values for each case are listed in Table B.1.

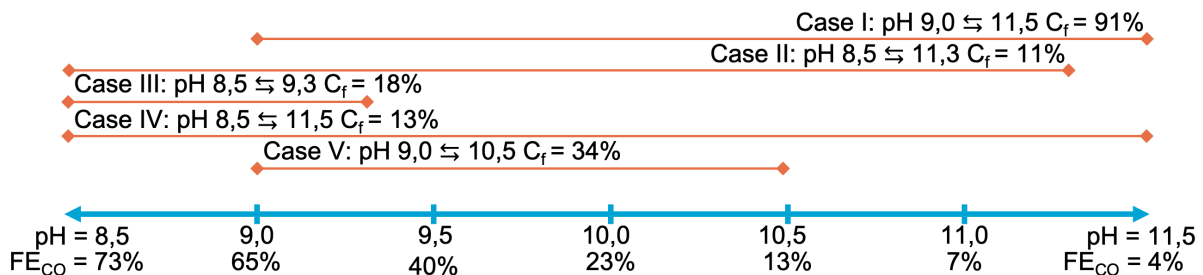


**Figure 4.1:** Visualization of pH steps and CO<sub>2</sub> capture fraction (wt%) required for achieving the base case design goals. The point on the left represents the pH of the electrolyser inflow/absorption column outflow, while the point on the right represents the pH of the electrolyser outflow/absorption column inflow.

Case I operates at a high pH level to ensure efficient capture in the absorption column, which benefits from a high pH inflow. Cases II and IV exhibit similar pH steps, as both produce a 4:1 molar ratio of syngas to meet the design goals. The key difference is that Case II employs an rWGS reaction to achieve a 2:1 ratio, while in Case IV, the syngas can be used as-is. Case III requires a narrow pH step at a low pH to maintain high FE<sub>CO<sub>2</sub></sub>, while Case V features a mid-range pH step, as specified in the design requirements.

In Case I, a high  $C_f$  is achieved by reducing the gas-to-liquid (G/L) ratio, which increases the solvent-to-flue gas ratio and maximizes  $C_f$ . Additionally, the capture column in Case I is deliberately oversized relative to inflow rates to improve capture efficiency, accomplished by reducing the design specification

from a 70% approach to flood to 14%. The design also avoids low pH levels (below 9,0) where capture efficiency declines. Case I stands out as it is specifically optimized for capture, yielding a substantially higher  $C_f$  than in other cases.

In Cases II, III, IV, and V,  $C_f$  is notably lower because the pH step is governed by the electrolyser. In these cases, the pH step is determined first, and the column is subsequently designed to achieve this pH requirement rather than to optimize for a specific capture fraction. Operating at a pH = 8,5, which is less efficient for solvent capture, inherently limits the capture fraction. However, in Case V, where low solvent pH levels are avoided, the capture fraction improves significantly. Additionally, the columns in these cases are designed to handle up to  $70\% \pm 10\%$  of the flow, with a maximum approach to flooding of 80%, further limiting the achievable capture fraction.

These results highlight the trade-off between optimizing the pH level for the electrolyser to achieve a low pH, which is conducive to a high  $FE_{CO_2}$ , and maintaining higher pH levels (above 9,0) to enhance capture efficiency in the solvent. High  $C_f$  values can be achieved by optimizing the size of the absorption column, adjusting the G/L ratio, and feeding a high pH solvent.

## 4.2. OPEX analysis

This section presents the results of the OPEX analysis, which includes an  $LCOS_{LHV}$  comparison, an OPEX distribution analysis, a bridge plot highlighting key cost enablers, and an evaluation of the cost per kg of  $CO_2$  saved. These indicators reflect the system's techno-economic performance and directly contribute to addressing the research questions.

### 4.2.1. $LCOS_{LHV}$ comparison

The  $LCOS_{LHV}$  metric is used to assess the economic performance of the system in comparison to literature data on various compounds and production methods (see Table B.2 for literature data). The  $LCOS_{LHV}$  comparison is illustrated in Figure 4.2.

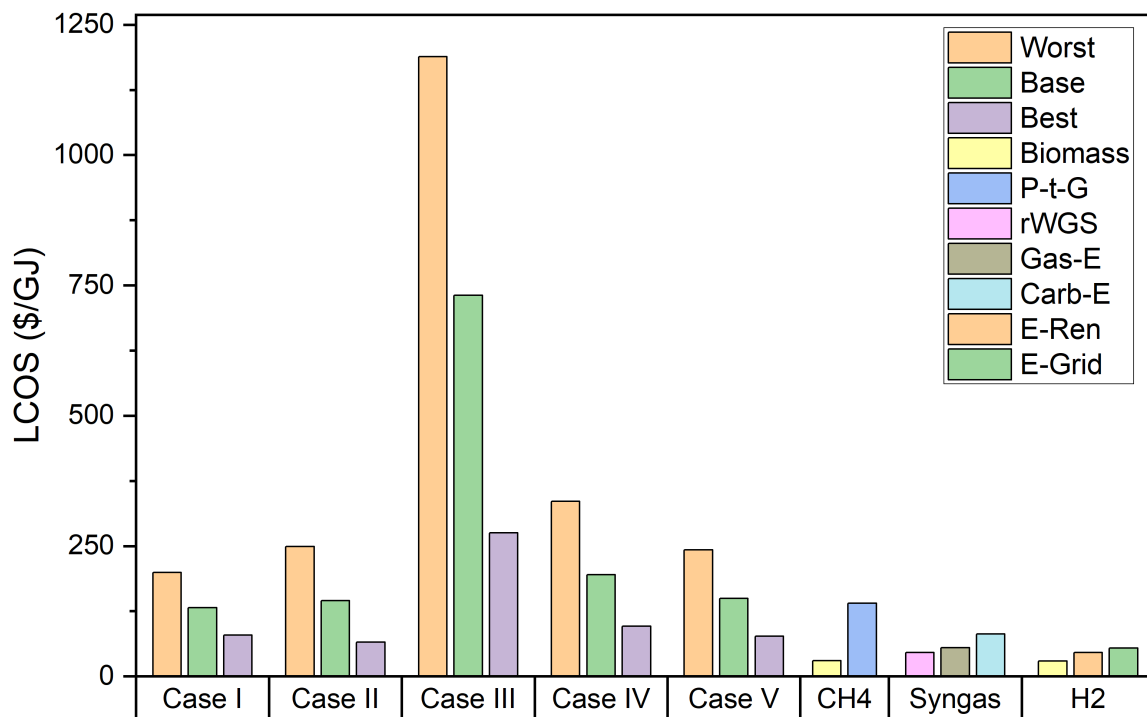


**Figure 4.2:**  $LCOS_{LHV}$  for various cases, including Power-to-Gas (P-t-G), reverse Water-Gas Shift (rWGS), gas-fed ( $CO_2RR$ ), bicarbonate electrolysis (Carb-E), and  $H_2$  electrolysis powered by either grid electricity (E-Grid) or renewable electricity (E-Ren) [110, 111, 93, 112].

The plot shows a clear gradient across the worst, base, and best scenarios: the worst case consis-

tently achieves a higher  $LCOS_{LHV}$  than the base case, and the base case  $LCOS_{LHV}$  is higher than the best case. Cases I, II, IV, and V follow similar trends with minor variations, while Case III displays a significantly higher  $LCOS_{LHV}$  compared to the others. This deviation in Case III is attributed to the system operating primarily at high  $FE_{CO}$ , which leads to a greater production of low-LHV CO relative to high-LHV  $H_2$ . Additionally, some  $CO_2$  remains in the product stream due to insufficient  $H_2$  production to fully react all  $CO_2$  in the rWGS reaction. This unreacted  $CO_2$  further reduces the LHV of the product, resulting in a higher  $LCOS_{LHV}$ .

When compared with other compounds—specifically  $CH_4$ , syngas, and  $H_2$ —the integrated system in Cases I, II, IV, and V demonstrates competitiveness with electricity-to-chemical pathways for  $CH_4$ , syngas, and  $H_2$  production, though only under the best-case scenario. However, biomass-based production methods still achieve a lower  $LCOS_{LHV}$  than these cases. Notably, Case III demonstrates limited competitiveness when normalised for LHV, primarily due to its reduced efficiency in generating high-LHV compounds.

The  $LCOS_{LHV}$  favours  $H_2$  production due to its higher LHV compared to CO, resulting in lower  $LCOS_{LHV}$  values for systems operating at higher pH and lower  $FE_{CO}$ . When interpreting these results, it is essential to consider the desired product. If CO is the preferred product, operating with smaller pH steps is beneficial to maintain higher  $FE_{CO}$ , although this will increase  $LCOS_{LHV}$ . Conversely, if higher energy density is required, operating with larger pH steps, which favour  $H_2$  production, will yield lower  $LCOS_{LHV}$  values. For completeness, results for OPEX per kg of CO and not normalized LCOS data for syngas are presented in Figure B.2 and Figure B.1. This shows that normalizing to CO production significantly reduces the LCOS for Case III, bringing it in line with Cases I, II, IV, and V.

A potentially more efficient approach to achieving a high-LHV syngas product involves producing syngas with a high CO content by operating at a small, low pH step to achieve high  $FE_{CO}$ , and then combining the CO with  $H_2$  generated via water electrolysis. Water electrolysis can be conducted at significantly lower potentials (1.6–2.0 V), making a CCU process with small pH steps, coupled with a  $H_2$  electrolyser, potentially more favourable than a CCU system with larger pH steps when a high-LHV product is desired.

#### 4.2.2. Sankey plot for OPEX distribution

As identified in subsection 4.2.1, the overall system OPEX has been established; this section focuses on the distribution of these costs. Using Sankey plots, the OPEX is allocated between the absorption column and the electrolyser. On the left, the overall OPEX shares are displayed, while on the right, these costs are specifically allocated to either the absorption column or the electrolyser. Raw material costs are shown as a separate category, as they cannot be directly attributed to either component. Fixed and investment costs, driven by CAPEX, are allocated in proportion to their respective CAPEX shares. Utility costs include electricity for the electrolyser, the flue gas compressor, liquid pump, and absorption column. Consumables costs include catalyst replacement expenses, which are specifically attributed to the electrolyser.

For visualization, base cases II, III, and V are highlighted as they represent different pH step sizes: a large step (8.5 ↔ 11.3), a small step (8.5 ↔ 9.3), and an intermediate step (9.0 ↔ 10.5), respectively. The corresponding visualizations are provided in Figure 4.3, Figure 4.4, and Figure 4.5. Sankey plots for Case I and IV can be found in Figure B.3 and Figure B.4

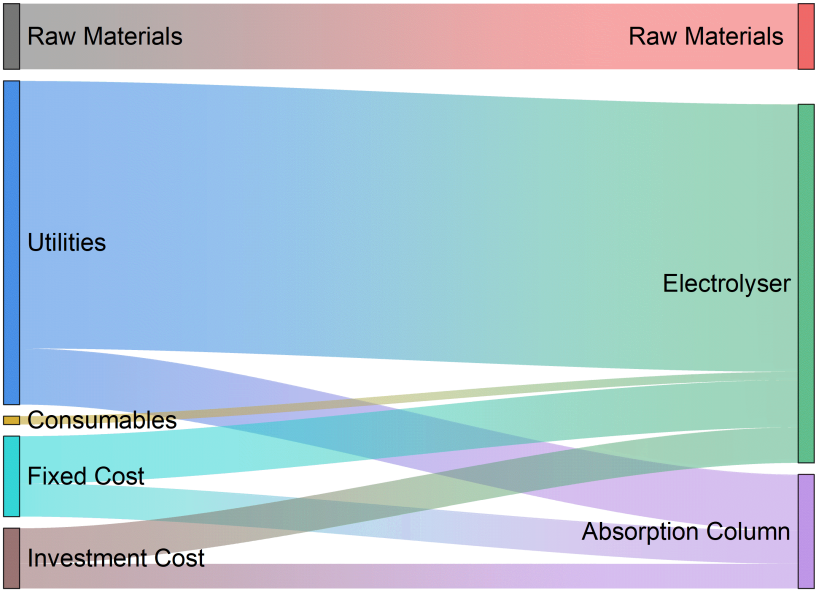


Figure 4.3: Sankey diagram showing OPEX distribution for Case II (Base Scenario): pH step 8,5 ↔ 11,3. Total OPEX \$20,5 million/year.

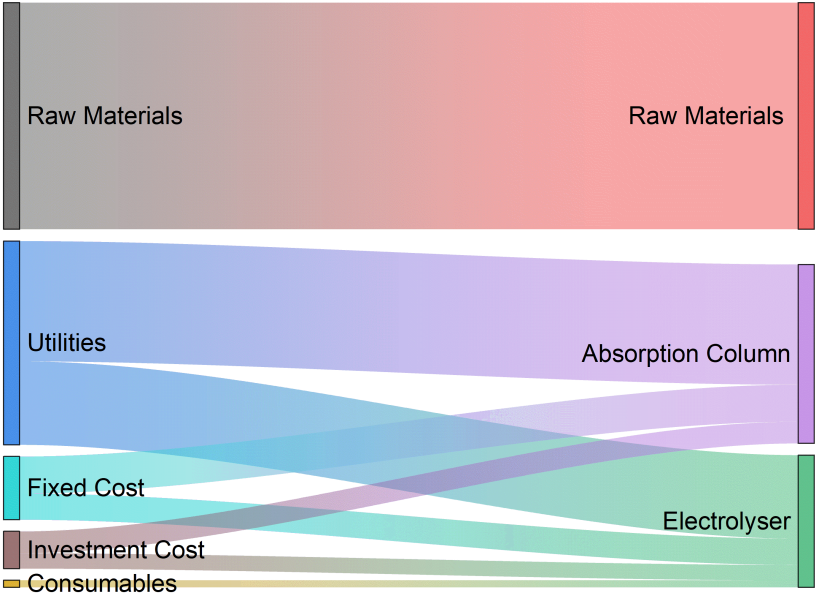
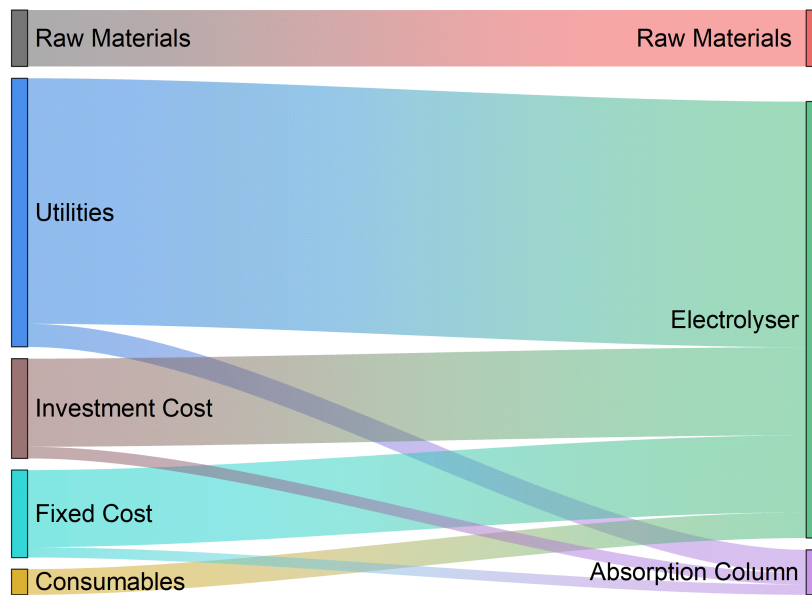


Figure 4.4: Sankey diagram showing OPEX distribution for Case III (Base Scenario): pH step 8,5 ↔ 9,3. Total OPEX: \$61,8 million/year.



**Figure 4.5:** Sankey diagram showing OPEX distribution for Case V (Base Scenario): pH step 9,0 ↔ 10,5. Total OPEX: \$21,0 million/year.

Figure 4.3 illustrates the OPEX distribution for Case II, where the electricity consumption of the electrolyser constitutes the largest share of OPEX, while the absorption column's OPEX remains relatively small due to efficient operation at a high pH inflow.

In Figure 4.4, the OPEX for Case III is primarily driven by raw material and utility costs, due to the system's larger size compared to Cases I, II, IV and V. The required  $\text{HCO}_3^-$  conversion for the pH adjustment is minimal: approximately 10% for a pH change from 8,5 to 9,0 and 8% for a shift from 9,0 to 9,3. This low conversion rate results from the Bjerrum plot being less steep at these points. Furthermore, because only minimal conversion is required while the system retains a 20 MW power rating, the inflow volume must be significantly larger than in other cases.

This high inflow volume results in increased raw material costs and substantial flue gas compression costs, which contribute to the overall utility costs. Additionally, the large inflows necessitate a relatively large absorption column compared to the electrolyser. Operating with a solvent at a lower pH of 9,3 reduces capture efficiency, further raising the OPEX for the absorption column.

Figure 4.5 demonstrates that for an intermediate pH step, the electrolyser's electricity consumption is the largest contributor to OPEX. Here, the electrolyser accounts for the majority of total OPEX, while the absorption column's OPEX remains relatively small due to the smaller system size required for this pH step. Although the electrolyser size is unchanged, it operates with a significantly smaller absorption column because of the reduced pH step. This configuration avoids low  $\text{FE}_{\text{CO}}$  electrolyser operation at low pH levels (below 9,0).

Notably, the absorption column's OPEX in Case II is higher than in Case V. The absorption column is most efficient at high pH levels, so the initial portion of the pH step in Case II is more effective. However, the smaller pH step in Case V avoids inefficient electrolyser operation below pH 9,0, making the absorption column a smaller portion of OPEX compared to Case II.

These results highlight a trade-off between achieving a large pH step with a small mass flow versus a small pH step with a large inflow. In systems with large pH steps, electricity costs dominate, while in systems with small pH steps, raw material and utility costs (primarily flue gas compression) are the main cost drivers. Additionally, the influence of pH on solvent inflow to the absorption column is evident: the absorption column's share of OPEX is minimized when operated with a high-pH solvent (above pH 10,0) and increases significantly at lower, less efficient pH levels (below 9,0).

### 4.2.3. Bridge plot for $LCOS_{LHV}$

As shown in subsection 4.2.1, the integrated CCU process can only achieve competitive  $LCOS_{LHV}$  under the best-case scenario. This section focuses on exploring parameter dependencies and identifying potential enablers for the integrated CCU system.

The impact of varying technical and economic model parameters is visualized through a series of bridge plots. Starting with the base scenario from the sensitivity analysis, each bridge plot incrementally adjusts individual parameters to illustrate their effects on  $LCOS_{LHV}$ . The progression culminates in the best-case scenario, where all parameters are optimized to achieve the lowest possible  $LCOS_{LHV}$  for the system.

The system size varies with changes in  $FE_{CO}$  when transitioning from the worst-case to the best-case scenario. This variation impacts the system's sizing, as reflected in the rightmost bar of the bridge plot. Depending on the specific adjustments made during these changes, the  $LCOS_{LHV}$  can either increase or decrease. The bridge plot for Case II is shown in Figure 4.6, while the results for Cases I, III, IV, and V are provided in section B.3 and illustrated in Figure B.5, Figure B.6, Figure B.7, and Figure B.8, respectively.

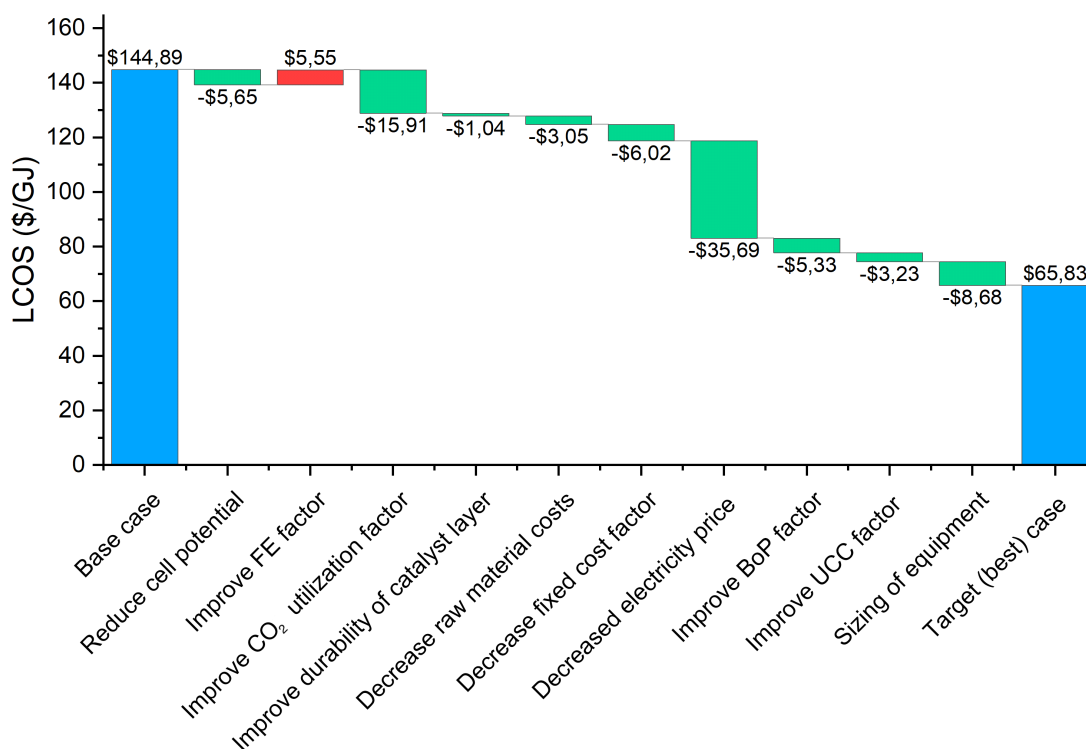


Figure 4.6: Bridge plot showing  $LCOS_{LHV}$  for Case II (base → best).

A similar pattern can be observed for Cases I, II, IV and V where the reduction in electricity cost causes the largest drop in  $LCOS_{LHV}$ . This is in line with literature on gas-fed  $CO_2RR$  electrolyzers, as seen in subsection 2.5.1, where the OPEX for electricity comprises the largest portion of the overall costs. Notably, as the  $FE_{CO}$  increases, the  $LCOS_{LHV}$  decreases slightly. This is due to the production of more low-LHV CO compared to high-LHV  $H_2$ . The increase in  $CO_2$  utilization ratio results in a lower concentration of  $CO_2$  in the electrolyser outlet stream, which in turn reduces  $H_2$  consumption in the subsequent rWGS reaction. This produces a higher LHV product, leading to a significant decrease in  $LCOS_{LHV}$ . This effect is more significant than the decrease in  $LCOS_{LHV}$  resulting from the increased CO production due to a higher  $CO_2$  utilization ratio. The effects of other improved system parameters are comparatively minor.

In subsection 4.2.2, it is evident that raw material costs play a larger role due to the higher solvent flow rates in Case III. This makes the impact of reduced raw material prices more significant compared to

Cases I, II, IV, and V. Furthermore, the pH step is more sensitive to changes in  $FE_{CO}$ , which strongly influences system size. Consequently, system sizing has a greater impact on  $LCOS_{LHV}$ , as shown in Figure B.6.

These results highlight that the most significant enabler for reducing costs in all five cases is lowering electricity prices. This aligns with the findings from subsection 4.2.2, which show that electricity and utility costs constitute the largest portion of OPEX. However, the system's heavy reliance on electricity prices also presents a vulnerability, as fluctuations in economic conditions can significantly impact the system's economic viability, potentially discouraging investment decisions.

In the sensitivity analysis, the base case was assumed to reflect current operating conditions. As shown in subsection 4.2.1, the systems are competitive with other electrolysis methods only under the best-case scenarios. However, achieving these optimal conditions requires all parameters to improve from their base values to their best values for the reduction in  $LCOS_{LHV}$ , as demonstrated in the bridge chart, to be realized.

#### 4.2.4. Cost of CO<sub>2</sub> savings

To relate the CO<sub>2</sub> savings to OPEX, the cost per kg of CO<sub>2</sub> saved by the system is visualized in Figure 4.7. This metric is derived by calculating the total OPEX and dividing it by the annual CO<sub>2</sub> savings, assuming 100% wind energy as the power source. The annual CO<sub>2</sub> savings are calculated using the methods outlined in section 3.6.

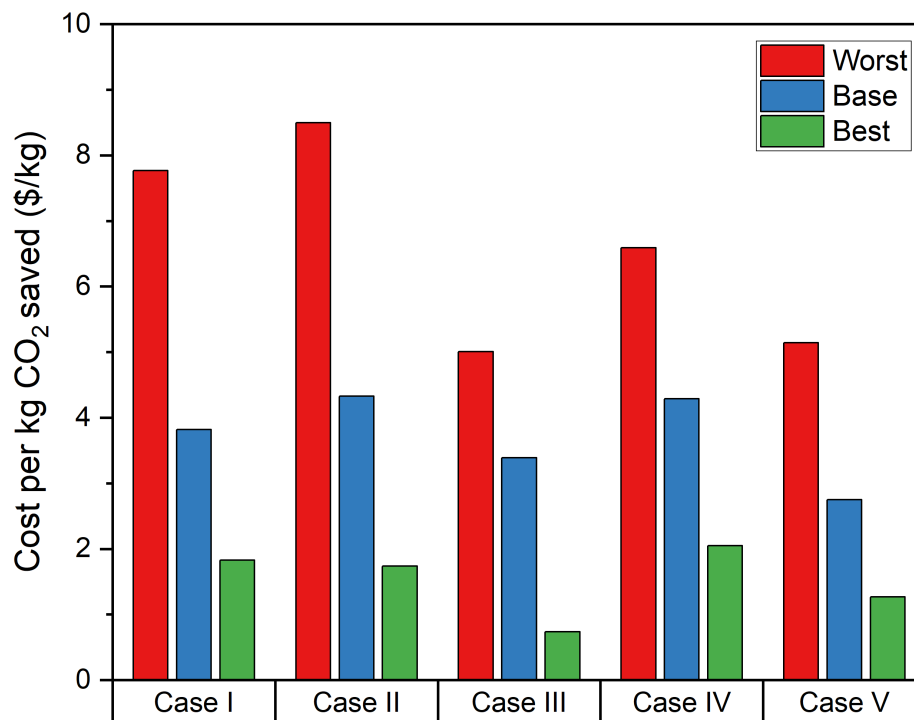


Figure 4.7: OPEX per kg CO<sub>2</sub> not emitted (energy source: 100% wind).

A consistent trend is observed across all cases, where the sensitivity analysis reveals significant cost reductions per kilogram of CO<sub>2</sub> saved under more optimistic scenarios. Case III achieves a slightly lower cost per kilogram of CO<sub>2</sub> saved due to its operation at high  $FE_{CO}$ , resulting in greater CO<sub>2</sub> conversion relative to H<sub>2</sub> compared to Cases I, II, IV, and V. It is important to note that this analysis does not account for the additional benefits of oxygen production.

Figure B.9 shows the same metric, but for an energy source mix of 50/50% wind and solar. This energy mix has higher CO<sub>2</sub> emissions per MWh compared to 100% wind (see Table 3.7, resulting in an amplification of the outcomes: the worst cases become significantly worse, while the best cases are less affected. For scenarios with already minimal CO<sub>2</sub> savings, the net benefit becomes even smaller,

making the cost per kilogram of CO<sub>2</sub> saved more costly. The impact on the base and best cases is still noticeable, though to a lesser extent. These results highlight the necessity of using low-CO<sub>2</sub>-emitting energy sources for powering the integrated CCU system.

Furthermore, the cost of CO<sub>2</sub> carbon credits within the EU ETS system is currently approximately 0,10 \$/kg [113]. The results from Figure 4.7 demonstrate that, at present, the cost of saving CO<sub>2</sub> per kilogram significantly exceeds the cost of emitting CO<sub>2</sub> and paying the corresponding carbon tax. However, projections indicate that the cost of EU ETS carbon credits will increase in the future, potentially enhancing the cost-competitiveness of the integrated CCU system as a viable decarbonisation strategy [114].

To account for the added benefit of the produced syngas, the cost of the integrated system could be compared to the costs of producing syngas and oxygen through traditional methods. Additionally, in scenarios where the integrated CCU system is not employed, the EU ETS must be paid for the CO<sub>2</sub> that is not captured but instead emitted. However, this scenario is considered beyond the scope of this thesis, as it would require a full model of the DRI steelmaking process with the CCU system integrated, whereas this work focuses solely on the CCU system itself.

### 4.3. CAPEX Analysis

This section evaluates the CAPEX of the integrated CCU system. The total system CAPEX includes the capital expenditures for the components within the scope of this study: the electrolyser UCC, absorption column, flue gas compressor, and liquid pump.

The total system CAPEX, normalised to CO production, is assessed across the five cases, with results presented in Figure B.10. The data indicate that cases operating at a low pH step and thus higher FE<sub>CO</sub> step have a lower cost per tonne of CO product. Conversely, systems with pH steps reaching higher pH levels show reduced CO production relative to their CAPEX, due to the diminished FE<sub>CO</sub> of the bicarbonate electrolyser at alkaline pH levels. In addition, the distribution of CAPEX among equipment is shown in Figure B.11, demonstrating that for larger systems, compression costs become more significant relative to electrolyser costs. The CAPEX contributions from the absorption column and pump are relatively small in comparison.

The remainder of the analysis focuses on the bicarbonate electrolyser unit, comparing it to its primary competitors: H<sub>2</sub> electrolysers and gas-fed CO<sub>2</sub>RR electrolysers, which serve as alternative solutions for large-scale renewable energy storage. To facilitate a direct comparison, the UCC of these technologies is calculated as outlined in subsection 3.5.3.

#### 4.3.1. UCC comparison to H<sub>2</sub> electrolysers

To compare the UCC calculated in this work with values from the literature on H<sub>2</sub> electrolysers, the model data is visualized in a bar chart alongside the literature data in Figure 4.8.

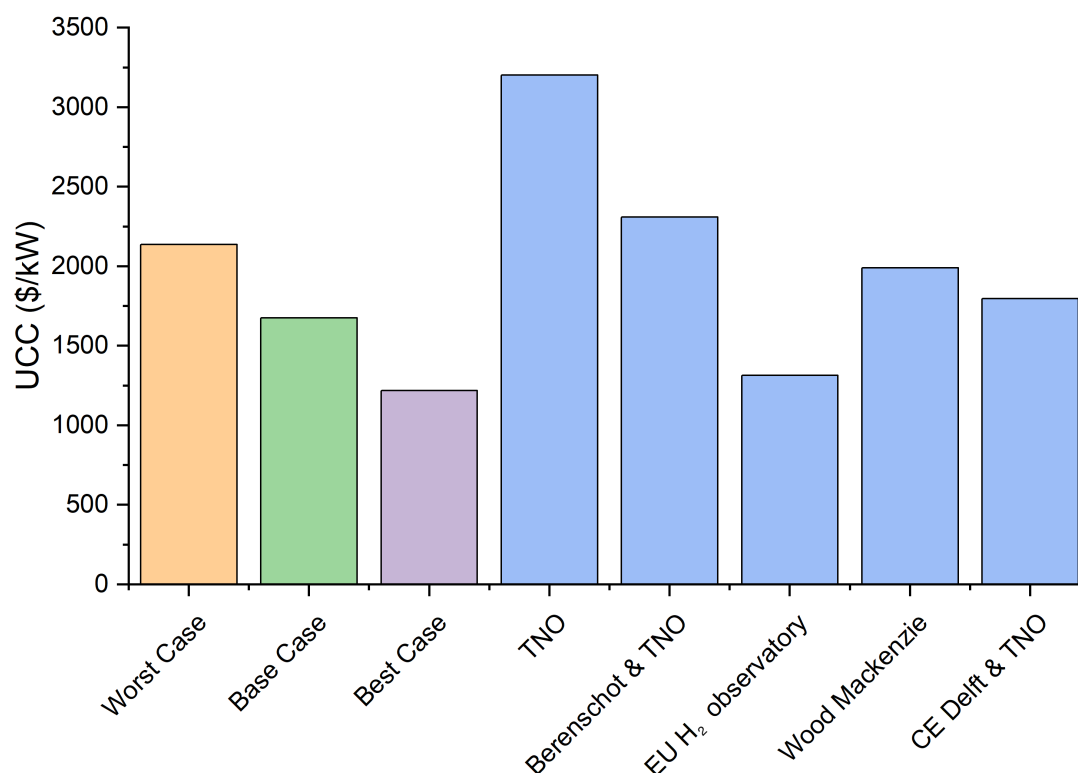


**Figure 4.8:** Unit Capital Cost (UCC) comparison of electrolyzers: TNO [106], Berenschot & TNO [104], EU Hydrogen Observatory [107], Wood Mackenzie [108], CE Delft & TNO [109].

Since both the CD and power input ( $100 \text{ mA/cm}^2$  and  $20 \text{ MW}$ , respectively) are fixed, the cost per kWh should remain consistent across the worst-case, base-case, and best-case scenarios for the five cases. The results confirm this, observing a similar pattern. Due to the overlapping data, the bars are comprised into one for worst, base, and best.

Compared to recent  $\text{H}_2$  electrolyser studies in the literature, the bicarbonate electrolyser exhibits competitive performance in terms of cost per kilowatt (USD/kW). Notably, the membrane cost accounts for only a small portion of the total cost when BoP, indirect costs, owner's costs, and contingency costs are factored in. Moreover, unlike  $\text{H}_2$ , the syngas product does not require the same degree of compression within the unit, simplifying the process and reducing associated expenses. A study by TNO reports significantly higher costs compared to other studies and the findings of this work. Their results suggest that older studies have substantially underestimated the cost per kilowatt of  $\text{H}_2$  electrolyzers [104].

In terms of UCC per kW, the electrolyzers perform similarly; however, the key difference lies in their products and the bicarbonate electrolyser's capability to convert  $\text{CO}_2$ , which would otherwise be emitted, into CO. Different applications require different types of electrolyzers, and the choice should be guided by specific product and conversion requirements. If  $\text{H}_2$  is the desired product,  $\text{H}_2$  electrolyzers can achieve this at a lower potential compared to bicarbonate electrolyzers. Nonetheless, the  $\text{H}_2$  produced by bicarbonate electrolyzers holds value as part of the syngas and can also react with unreacted  $\text{CO}_2$  in the downstream rWGS step, maximizing CO production and eliminating  $\text{CO}_2$  waste streams.

#### 4.3.2. UCC comparison to $\text{CO}_2\text{RR}$ electrolyzers

In the comparison with gas-fed  $\text{CO}_2$  electrolyzers, the UCC is normalized to CO production, measured in USD per ton of CO product. Data from Moreno et al. represents both bicarbonate and gas-fed  $\text{CO}_2$  electrolyzers in the base case, while data from Jouny et al. provides results for a gas-fed  $\text{CO}_2$  electrolyser unit, showing both base and best-case scenarios. The results are visualized in Figure 4.9.

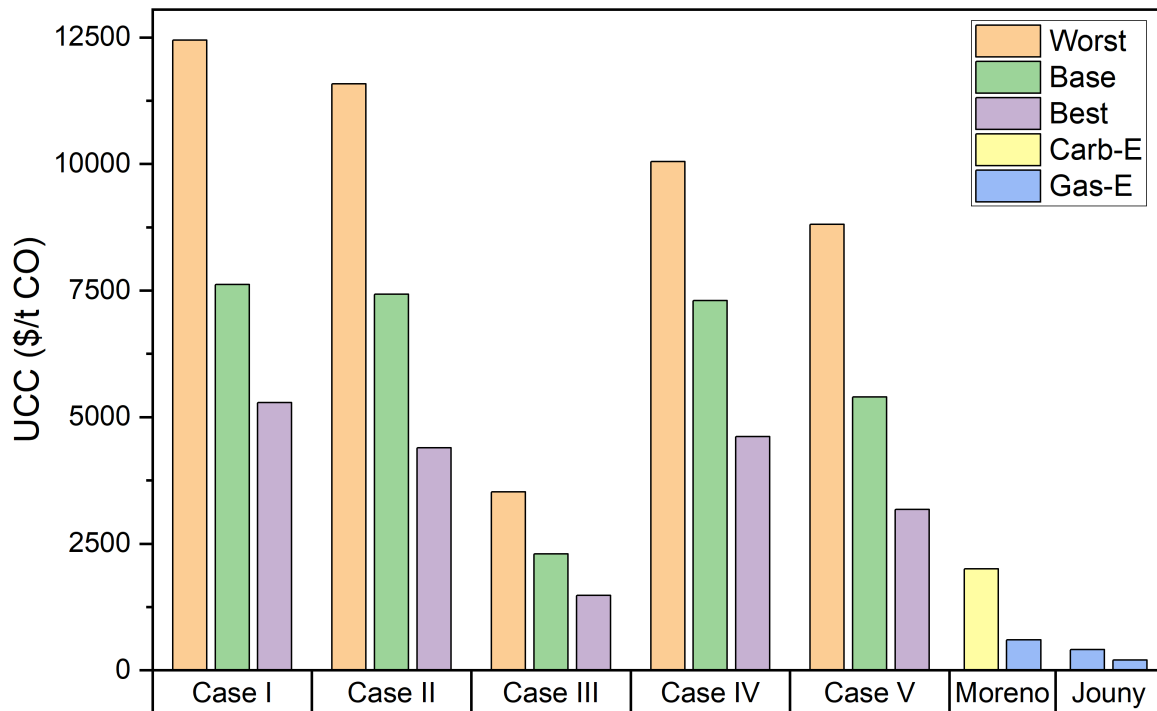


**Figure 4.9:** Comparison of UCC per tonne of CO with literature data on CO<sub>2</sub>RR electrolyzers. Data from Moreno et al. represents the base case, while for data from Jouny et al., the left bar represents the base case and the right bar represents the best case [93, 29].

A clear difference in UCC per tonne of CO is observed, with the gas-fed CO<sub>2</sub>RR electrolyser significantly outperforming the bicarbonate electrolyser. The state-of-the-art bicarbonate electrolyser suffers a substantial drop in FE<sub>CO</sub> as the current density increases (see Figure 2.2), requiring a larger surface area to produce the same amount of CO. In contrast, gas-fed CO<sub>2</sub> electrolyzers can operate at much higher current densities while maintaining high FE<sub>CO</sub> (see Table 2.1). As a result, the current density for the bicarbonate electrolyser is fixed at 100 mA/cm<sup>2</sup>. The higher operating current densities of gas-fed electrolyzers reduce the electrode area required for CO production, leading to a lower CAPEX for the same production capacity.

Literature data from Moreno et al. on Carb-E aligns with the base scenario results of Case III. Their analysis reports an average FE of 29% at 200 mA/cm<sup>2</sup>, though it does not specify the pH step. The lower FE<sub>CO</sub> observed in their study leads to reduced CO production compared to the higher FE<sub>CO</sub> achieved in Case III. However, this is offset by the higher current density in their system, resulting in comparable overall performance between the base scenario of Case III and the findings of Moreno et al.

#### 4.3.3. UCC for increased current density

The five cases show a significantly higher UCC compared to literature data on gas-fed CO<sub>2</sub> electrolyzers, primarily due to differences in current density and the corresponding FE<sub>CO</sub>. While the bicarbonate electrolyser can operate at higher current densities, this typically results in reduced FE<sub>CO</sub>. To identify the current density at which the bicarbonate electrolyser becomes competitive, a hypothetical scenario was explored where the current density was incrementally increased in 10 steps of 100 mA/cm<sup>2</sup>. This analysis was conducted using the same pH-dependent model inputs for FE<sub>CO</sub> as at 100 mA/cm<sup>2</sup> (displayed in Table A.10). Since this analysis examines an optimistic scenario, best-case data were applied. The results are presented in Figure 4.10.

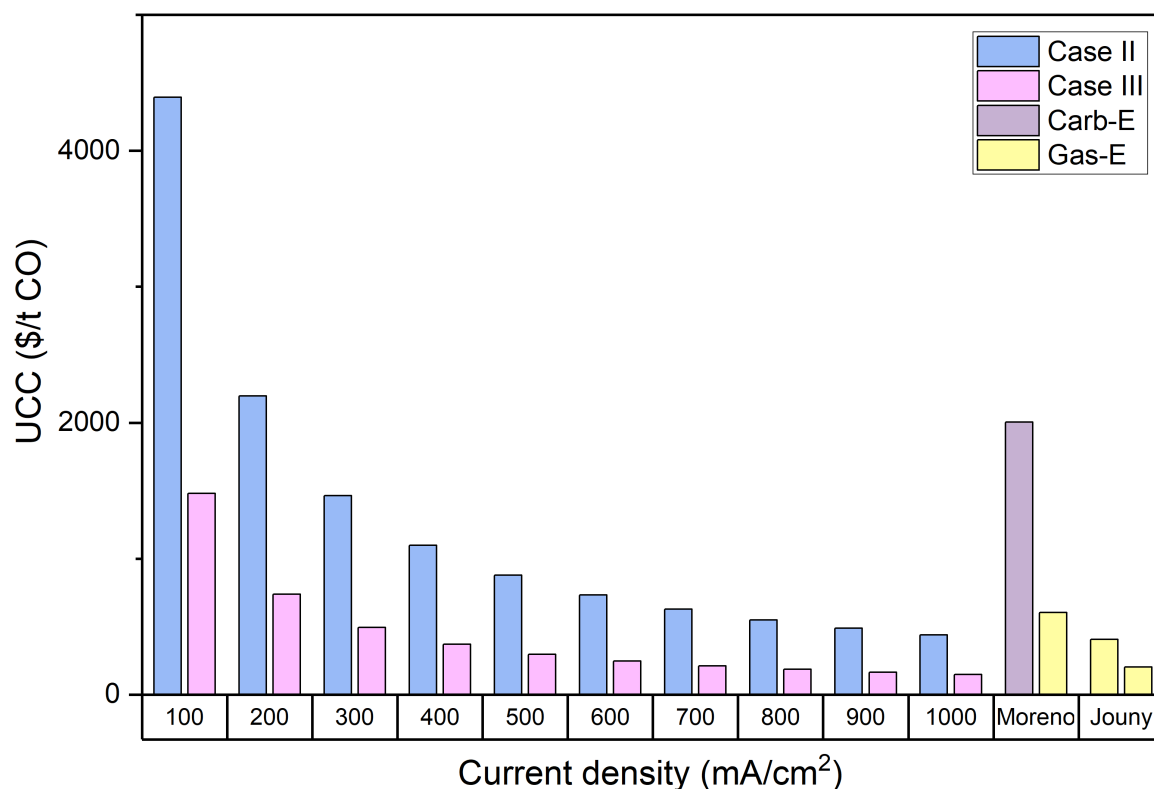


**Figure 4.10:** Effect of varying CD on UCC in the best-case scenarios for cases II and III. Data from Moreno et al. represents the base case, while for data from Jouny et al., the left bar represents the base case and the right bar represents the best case [93, 29].

Increasing the CD reduces the required electrolyser area, as more electrons can be transferred per square meter. Consequently, this leads to a lower UCC, as shown in Figure 4.10. Case II (best) becomes competitive with gas-fed CO<sub>2</sub> electrolysers at around 600 mA/cm<sup>2</sup>, while Case III (best) achieves competitiveness at approximately 300 mA/cm<sup>2</sup>. Therefore, for bicarbonate electrolysers to compete with gas-fed CO<sub>2</sub>RR systems, significant improvements are necessary to enable operation at much higher current densities while sustaining the same FE<sub>CO</sub> as at 100 mA/cm<sup>2</sup> in the best-case scenario (see Table A.11). Currently, bicarbonate electrolysers have yet to reach this level of performance, as highlighted in Table 2.2.

Additionally, the FE<sub>CO</sub> is reduced not only by an increase in current density but also by an increase in pH. The combined effects of elevated current density and pH remain to be explored; however, these factors may reinforce one another, potentially making it more challenging for the UCC system to achieve competitiveness with gas-fed CO<sub>2</sub> electrolysers.

# 5

## Conclusion & Recommendations

This study explored the techno-economic feasibility of an integrated CCU system coupling the  $K_2CO_3$ -based capture to a bicarbonate electrolyser for  $CO_2$ RR for syngas production, specifically designed for applications within the steel industry. The following conclusions can be drawn through the analysis of various operational cases:

The pH step and  $CO_2$  capture fraction results reveal a clear trade-off between optimizing for high  $FE_{CO}$  by achieving a low pH inflow and maintaining a high solvent pH for efficient  $CO_2$  capture.

A large pH step was found to be advantageous in reducing  $LCOS_{LHV}$ , as higher pH values favour increased HER and lower  $FE_{CO}$ . Since  $H_2$  has a higher LHV than  $CO$ , more  $H_2$  in the product results in a lower  $LCOS_{LHV}$ . However, it needs to be assessed on a case-by-case basis whether a higher LHV output or higher  $CO$  production is more desirable.

All cases exhibited a higher  $LCOS_{LHV}$  compared to other methods reported in the literature. However, sensitivity analysis revealed that systems with a large pH step could be competitive with other electrolysis methods in terms of  $LCOS_{LHV}$ , but only in the best-case scenario. In contrast, the narrow, low pH step systems, which produce a lower LHV compound due to operating at high  $FE_{CO}$ , were unable to compete effectively. This is primarily because of their predominantly  $CO$  output, which results in a lower overall LHV and a higher  $LCOS_{LHV}$ .

The OPEX distribution results revealed that in scenarios with large pH steps, the electricity consumption of the electrolyser is the dominant cost component. However, as the pH transition narrows, the system size increases, leading to higher raw material and flue gas compression costs. The results from this work highlight the trade-off between the electrolyser and the absorption column: optimizing the electrolyser at low pH steps (close to  $pH = 8,5 - 9,0$ ) increases  $FE_{CO}$ , but incurs higher CAPEX and OPEX in the absorption column, as the absorption process favours a high pH solvent inflow. Conversely, if a large pH step (from  $pH = 8,5 - 9,0$  to  $10,0+$ ) is achieved through large  $HCO_3^-$  conversion in the electrolyser, it must partly operate at high pH levels, which significantly decreases  $FE_{CO}$  and reduces the amount of  $CO_2$  converted.

Bridge plot analysis showed the impact of changing technical and economic parameters on  $LCOS_{LHV}$ . The integrated CCU system exhibits high sensitivity to electricity prices, as these strongly influence both the electrolyser electricity cost and the utility cost. These are significant portions of OPEX, confirmed by subsection 4.2.2. In systems with a small pH step at low pH levels, raw material costs also become a significant factor, further affecting economic performance. Additionally, enhancements in the  $CO_2$  utilization ratio result in significant economic improvements by lowering the  $CO_2$  content in the outlet stream, which subsequently produces a higher LHV product after the rWGS reaction. In conclusion, the largest enabler for reducing  $LCOS_{LHV}$  is a reduction in electricity cost, followed by improvements in electrolyser performance, namely in  $CO_2$  utilization ratio. Other parameters have a comparatively less significant impact on  $LCOS_{LHV}$ .

The cost per kilogram of  $CO_2$  saved was analysed for systems powered by a 100% wind energy mix

and a 50% wind / 50% solar energy mix. This limited-scope analysis revealed a high cost per kilogram of CO<sub>2</sub> saved for all systems when compared to the cost of emitting the CO<sub>2</sub> under the EU ETS. However, this metric does not account for the additional benefits of syngas and oxygen production, which contribute further value to the system and could help offset the overall cost. Furthermore, the results underscore the importance of operating the integrated CCU system using energy sources with minimal CO<sub>2</sub> emissions to reduce the cost per kilogram of CO<sub>2</sub> saved.

The comparison of UCC demonstrated that the integrated CCU system is competitive with H<sub>2</sub> electrolysis in terms of UCC per installed kilowatt. However, when comparing UCC per kg of CO produced, the integrated CCU system shows significantly higher costs compared to the literature on competing gas-fed CO<sub>2</sub> electrolyzers. This is primarily due to the bicarbonate electrolyser's inability to operate at high current densities and alkaline pH while maintaining high FE<sub>CO</sub>.

Subsequently, a hypothetical scenario is explored in which the bicarbonate electrolyser competes with gas-fed electrolyzers in terms of UCC per kg of CO. The analysis indicates that current state-of-the-art bicarbonate electrolyzers either operate at insufficient current densities or experience a significant drop in FE<sub>CO</sub> at higher current densities. To achieve competitiveness, bicarbonate electrolyzers would require a substantial increase in current density while maintaining the FE<sub>CO</sub> observed at around 100 mA/cm<sup>2</sup> in the best-case scenario.

In conclusion, the TEA indicates that both the OPEX and CAPEX for the integrated CCU system are currently too high to be cost-competitive with alternative solutions. To improve the OPEX, technical and economic conditions would need to align with an optimistic scenario. Furthermore, achieving cost parity with gas-fed CO<sub>2</sub>RR systems would require a significant increase in current density while maintaining high FE<sub>CO</sub>, as well as sustaining these efficiencies at elevated pH levels.

The first recommendation is to experimentally establish the pH-dependent model inputs at various pH values and under operating conditions. The bicarbonate electrolyser should operate at a current density of 100 mA/cm<sup>2</sup>, with voltages of 3,3, 3,6, and 3,9 V, at a temperature of 60°C, and a pressure of 10 bar. Subsequently, inflows of HCO<sub>3</sub><sup>-</sup> with pH values starting from 8,5, in increments of 0,5, should be fed to the electrolyser, and the FE<sub>CO</sub> and CO<sub>2</sub> utilization ratio should be reported. These values can be used directly as model input, eliminating the need for a correction factor from ambient temperatures.

In a similar experiment, the model inputs can be adapted for C<sub>2</sub>+ products. The same experimental setup can be used, but the catalyst on the cathode side should be replaced with a Cu catalyst capable of producing C<sub>2</sub>+ compounds at reasonable FE<sub>CO</sub>. The FE<sub>CO</sub> and CO<sub>2</sub> utilization ratio at various pH levels can then be measured and used as inputs for the model. Subsequently, the Excel model can be adjusted to simulate the production of ethylene, ethanol, and methanol. For this system, additional downstream processes will be necessary to separate the gaseous and liquid products from the outflow streams.

The results indicate that state-of-the-art current densities, given the FE<sub>CO</sub> achieved, are insufficient to competitively match gas-fed CO<sub>2</sub>RR systems in terms of UCC. Furthermore, the effect of rising pH as a result of CO<sub>2</sub> conversion further reduces FE<sub>CO</sub>. Future work should focus on enhancing electrolyser design and improving catalyst performance to enable stable, high FE<sub>CO</sub> operation at current densities of 300+ mA/cm<sup>2</sup> under alkaline pH conditions (pH 9,0+).

The stability of the bicarbonate electrolyser must be significantly enhanced for industrial applications. Li et al. demonstrated stable operation for 145 hours at a fixed pH, while results from Burgers et al. (as shown in Figure 3.3) indicated a decline in stability after an initial performance peak within the first hour of operation [115]. As discussed in section 2.4, stability plays a crucial role in maintaining the performance of the integrated CCU system. If the required pH steps are not achieved in both the electrolyser and the absorption column, system performance deteriorates. For industrial implementation, bicarbonate electrolyzers must maintain stable operation for significantly longer durations—ideally 8000 hours or more. Further research should focus on catalyst degradation and the development of new catalyst materials to ensure extended stable operation.

Currently, the bicarbonate electrolyser exists only at the lab scale. The electrolyser architecture must be further developed and tested for a pilot-scale unit. In the proposed system, the electrolyser will be utilised to adjust the pH of the bicarbonate inflow, making it suitable for capture once again. This

can be achieved through various electrolyser architectures. One potential approach is to employ a single electrolyser with a large electrode, where the pH gradually changes along the electrode's length, resulting in corresponding variations in  $FE_{CO}$  and  $CO_2$  utilisation ratio. Alternatively, a modular design could be implemented, consisting of a series of smaller electrolyser compartments, each with its own operating conditions and pH step. This compartmentalised approach could provide greater control and optimisation of each step in the process.

Implementing this system in the steel industry, particularly in advanced DRI processes such as Ener-giron III and Midrex, requires further investigation. This study evaluates the intrinsic techno-economic performance of the integrated CCU system using flue gas from DRI processes. However, in practice, the system will not operate in isolation. When applied to steelmaking, the syngas product can be utilised in the EAF, along with the oxygen produced at the anode. In this context, further research is required to investigate process intensification, heat recovery, and overall system optimisation, as well as the impact of impurities in the process and potential upstream and downstream steps.

When an assessment of the costs of the full integrated CCU system implemented in the DRI steelmaking process is conducted, it can be compared to a scenario where the system is not implemented. In such a scenario, the syngas and oxygen would need to be produced separately or purchased from external suppliers. Additionally, the EU ETS tax would have to be paid for the  $CO_2$  that is not captured. Subsequently, the OPEX can be compared between the scenarios with and without the integrated CCU system.

This study presents a limited analysis of the  $CO_2$  emissions reductions achieved by this system. To fully assess its environmental impact, a comprehensive Life Cycle Assessment (LCA) is necessary. The LCA should account for emissions across the entire process when the integrated system is implemented in the DRI steelmaking process, including syngas utilization after the CCU process, the rWGS reactor, and both upstream and downstream stages. Such a holistic assessment will provide a more complete and accurate understanding of the system's overall environmental footprint.

# References

- [1] Sonia I. Seneviratne et al. *Allowable CO<sub>2</sub> emissions based on regional and impact-related climate targets*. Jan. 2016. DOI: 10.1038/nature16542.
- [2] BY R A Pielkejr et al. "HURRICANES AND GLOBAL WARMING". In: (). DOI: 10.1175/BAMS-86-II-1571.
- [3] Carl Friedrich Schleussner et al. *Science and policy characteristics of the Paris Agreement temperature goal*. Aug. 2016. DOI: 10.1038/nclimate3096.
- [4] Robert M. DeConto et al. "The Paris Climate Agreement and future sea-level rise from Antarctica". In: *Nature* 593.7857 (May 2021), pp. 83–89. ISSN: 14764687. DOI: 10.1038/s41586-021-03427-0.
- [5] Taylor Kuykendall and J Holzman. *Steel industry under rising pressure to produce greener product*. Mar. 2021.
- [6] Yeonbae Kim and Ernst Worrell. *International comparison of CO<sub>2</sub> emission trends in the iron and steel industry*. Tech. rep. 2002, pp. 827–838.
- [7] Gabriel Lopez et al. "From fossil to green chemicals: sustainable pathways and new carbon feedstocks for the global chemical industry". In: *Energy and Environmental Science* 16.7 (May 2023), pp. 2879–2909. ISSN: 17545706. DOI: 10.1039/d3ee00478c.
- [8] Edwin Basson. "2022 World Steel in Figures". In: (Apr. 2022). URL: <https://worldsteel.org/data/world-steel-in-figures-2022/#:~:text=However%2C%20we%20have%20forecasted%20that,Safety%20remains%20our%20top%20priority..>
- [9] Ahmed I. Osman et al. *Recent advances in carbon capture storage and utilisation technologies: a review*. Apr. 2021. DOI: 10.1007/s10311-020-01133-3.
- [10] Toby Lockwood. "A Compararitive Review of Next-generation Carbon Capture Technologies for Coal-fired Power Plant". In: *Energy Procedia*. Vol. 114. Elsevier Ltd, 2017, pp. 2658–2670. DOI: 10.1016/j.egypro.2017.03.1850.
- [11] Théo Alerte et al. "Downstream of the CO<sub>2</sub>Electrolyzer: Assessing the Energy Intensity of Product Separation". In: *ACS Energy Letters* 6.12 (Dec. 2021), pp. 4405–4412. ISSN: 23808195. DOI: 10.1021/acsenergylett.1c02263.
- [12] Eric W. Lees et al. *Gas diffusion electrodes and membranes for CO<sub>2</sub> reduction electrolyzers*. Jan. 2022. DOI: 10.1038/s41578-021-00356-2.
- [13] Chi Chen, Juliet F. Khosrowabadi Kotyk, and Stafford W. Sheehan. *Progress toward Commercial Application of Electrochemical Carbon Dioxide Reduction*. Nov. 2018. DOI: 10.1016/j.chempr.2018.08.019.
- [14] Eric W. Lees et al. "Electrodes Designed for Converting Bicarbonate into CO". In: *ACS Energy Letters* 5.7 (July 2020), pp. 2165–2173. ISSN: 23808195. DOI: 10.1021/acsenergylett.0c00898.
- [15] Eric William Lees. *ELECTROCHEMICAL CONVERSION OF BICARBONATE-RICH CO<sub>2</sub> CAPTURE SOLUTIONS INTO CARBON MONOXIDE*. Tech. rep. 2018.
- [16] Joshua A. Rabinowitz and Matthew W. Kanan. *The future of low-temperature carbon dioxide electrolysis depends on solving one basic problem*. Dec. 2020. DOI: 10.1038/s41467-020-19135-8.
- [17] Saket S. Bhargava et al. "System Design Rules for Intensifying the Electrochemical Reduction of CO<sub>2</sub> to CO on Ag Nanoparticles". In: *ChemElectroChem* 7.9 (May 2020), pp. 2001–2011. ISSN: 21960216. DOI: 10.1002/ce1c.202000089.

- [18] Donald S. Ripatti, Thomas R. Veltman, and Matthew W. Kanan. "Carbon Monoxide Gas Diffusion Electrolysis that Produces Concentrated C<sub>2</sub> Products with High Single-Pass Conversion". In: *Joule* 3.1 (Jan. 2019), pp. 240–256. ISSN: 25424351. DOI: 10.1016/j.joule.2018.10.007.
- [19] Giulia Marcandalli et al. "Electrolyte Effects on CO<sub>2</sub> Electrochemical Reduction to CO". In: *Accounts of Chemical Research* 55.14 (July 2022), pp. 1900–1911. ISSN: 15204898. DOI: 10.1021/acs.accounts.2c00080.
- [20] Alex J. Welch et al. *Bicarbonate or Carbonate Processes for Coupling Carbon Dioxide Capture and Electrochemical Conversion*. Mar. 2020. DOI: 10.1021/acsenergylett.0c00234.
- [21] Tengfei Li et al. "Electrolytic Conversion of Bicarbonate into CO in a Flow Cell". In: *Joule* 3.6 (June 2019), pp. 1487–1497. ISSN: 25424351. DOI: 10.1016/j.joule.2019.05.021.
- [22] Peng Zhu et al. "Direct and continuous generation of pure acetic acid solutions via electrocatalytic carbon monoxide reduction". In: (). DOI: 10.1073/pnas.2010868118/-/DCSupplemental. URL: <https://doi.org/10.1073/pnas.2010868118>.
- [23] Eric W Lees et al. *Supporting Information Electrodes Designed for Converting Bicarbonate into CO*. Tech. rep.
- [24] Yongwook Kim et al. "Electrochemical capture and conversion of CO<sub>2</sub> into syngas-0001-6875-849X Content not peer-reviewed by ChemRxiv. License: CC BY-NC-ND 4.0". In: (). DOI: 10.26434/chemrxiv-2023-hvjxn. URL: <https://doi.org/10.26434/chemrxiv-2023-hvjxn> ORCID: <https://orcid.org/0000>.
- [25] Magda H. Barecka, Joel W. Ager, and Alexei A. Lapkin. "Carbon neutral manufacturing via on-site CO<sub>2</sub> recycling". In: *iScience* 24.6 (June 2021). ISSN: 25890042. DOI: 10.1016/j.isci.2021.102514.
- [26] Hasan Muslemani et al. "Opportunities and challenges for decarbonizing steel production by creating markets for 'green steel' products". In: *Journal of Cleaner Production* 315 (Sept. 2021). ISSN: 09596526. DOI: 10.1016/j.jclepro.2021.128127.
- [27] Nicole Bond, Robert Symonds, and Robin Hughes. "Pressurized Chemical Looping for Direct Reduced Iron Production: Carbon Neutral Process Configuration and Performance". In: *Energies* 15.14 (July 2022). ISSN: 19961073. DOI: 10.3390/en15145219.
- [28] Gabriel Lopez, Javier Farfan, and Christian Breyer. "Trends in the global steel industry: Evolutionary projections and defossilisation pathways through power-to-steel". In: *Journal of Cleaner Production* 375 (Nov. 2022). ISSN: 09596526. DOI: 10.1016/j.jclepro.2022.134182.
- [29] Matthew Jouny, Wesley Luc, and Feng Jiao. "General Techno-Economic Analysis of CO<sub>2</sub> Electrolysis Systems". In: *Industrial and Engineering Chemistry Research* 57.6 (Feb. 2018), pp. 2165–2177. ISSN: 15205045. DOI: 10.1021/acs.iecr.7b03514.
- [30] M. S. Sajna et al. "Electrochemical system design for CO<sub>2</sub> conversion: A comprehensive review". In: *Journal of Environmental Chemical Engineering* 11.5 (Oct. 2023). ISSN: 22133437. DOI: 10.1016/j.jece.2023.110467.
- [31] Devin T. Whipple and Paul J.A. Kenis. "Prospects of CO<sub>2</sub> utilization via direct heterogeneous electrochemical reduction". In: *Journal of Physical Chemistry Letters* 1.24 (Dec. 2010), pp. 3451–3458. ISSN: 19487185. DOI: 10.1021/jz1012627.
- [32] Allen Bard and Larry Faulkner. *Electrochemical Methods: Fundamentals and Applications, 2nd Edition*. 2nd edition. 2000, pp. 222–234.
- [33] Ramato Ashu Tufa et al. "Towards highly efficient electrochemical CO<sub>2</sub> reduction: Cell designs, membranes and electrocatalysts". In: *Applied Energy* 277 (Nov. 2020). ISSN: 03062619. DOI: 10.1016/j.apenergy.2020.115557.
- [34] Edmund J.F. Dickinson and Andrew J. Wain. "The Butler-Volmer equation in electrochemical theory: Origins, value, and practical application". In: *Journal of Electroanalytical Chemistry* 872 (Sept. 2020). ISSN: 15726657. DOI: 10.1016/j.jelechem.2020.114145.
- [35] E Richard Cohen and Barry N Taylor. *The 1986 adjustment of the fundamental physical constants' prepared by*. Tech. rep. 1987.

- [36] Tatsuya Shinagawa, Angel T. Garcia-Esparza, and Kazuhiro Takanabe. "Insight on Tafel slopes from a microkinetic analysis of aqueous electrocatalysis for energy conversion". In: *Scientific Reports* 5 (Sept. 2015). ISSN: 20452322. DOI: 10.1038/srep13801.
- [37] Sumit Verma et al. "A gross-margin model for defining techno-economic benchmarks in the electroreduction of CO<sub>2</sub>". In: *ChemSusChem* 9.15 (Aug. 2016), pp. 1972–1979. ISSN: 1864564X. DOI: 10.1002/cssc.201600394.
- [38] Shiqiang Hui et al. *Three-dimensional cathodes for electrochemical reduction of CO<sub>2</sub>: From macro-to nano-engineering*. Sept. 2020. DOI: 10.3390/nano10091884.
- [39] Kendra P. Kuhl et al. "New insights into the electrochemical reduction of carbon dioxide on metallic copper surfaces". In: *Energy and Environmental Science* 5.5 (May 2012), pp. 7050–7059. ISSN: 17545692. DOI: 10.1039/c2ee21234j.
- [40] Kendra P. Kuhl et al. "Electrocatalytic conversion of carbon dioxide to methane and methanol on transition metal surfaces". In: *Journal of the American Chemical Society* 136.40 (Oct. 2014), pp. 14107–14113. ISSN: 15205126. DOI: 10.1021/ja505791r.
- [41] Zhenyu Sun et al. *Fundamentals and Challenges of Electrochemical CO<sub>2</sub> Reduction Using Two-Dimensional Materials*. Oct. 2017. DOI: 10.1016/j.chempr.2017.09.009.
- [42] Samuel C. Perry et al. *Developments on carbon dioxide reduction: Their promise, achievements, and challenges*. Apr. 2020. DOI: 10.1016/j.coelc.2020.04.014.
- [43] Bijandra Kumar et al. "New trends in the development of heterogeneous catalysts for electrochemical CO<sub>2</sub> reduction". In: *Catalysis Today* 270 (July 2016), pp. 19–30. ISSN: 09205861. DOI: 10.1016/j.cattod.2016.02.006.
- [44] Yuanyuan Xue et al. *Catalyst Design for Electrochemical Reduction of CO<sub>2</sub> to Multicarbon Products*. Oct. 2021. DOI: 10.1002/smt.202100736.
- [45] Geng Li et al. *Development of catalysts and electrolyzers toward industrial-scale CO<sub>2</sub> electroreduction*. May 2022. DOI: 10.1039/d2ta02086f.
- [46] Jiayi Lin et al. *CO<sub>2</sub> electrolysis: Advances and challenges in electrocatalyst engineering and reactor design*. May 2023. DOI: 10.1016/j.matre.2023.100194.
- [47] Emily Jeng and Feng Jiao. "Investigation of CO<sub>2</sub> single-pass conversion in a flow electrolyzer". In: *Reaction Chemistry and Engineering* 5.9 (Sept. 2020), pp. 1768–1775. ISSN: 20589883. DOI: 10.1039/d0re00261e.
- [48] Angelica Reyes et al. "Managing Hydration at the Cathode Enables Efficient CO<sub>2</sub> Electrolysis at Commercially Relevant Current Densities". In: *ACS Energy Letters* 5.5 (May 2020), pp. 1612–1618. ISSN: 23808195. DOI: 10.1021/acsenenergylett.0c00637.
- [49] Ana Sofia Varela. *The importance of pH in controlling the selectivity of the electrochemical CO<sub>2</sub> reduction*. Dec. 2020. DOI: 10.1016/j.cogsc.2020.100371.
- [50] Philippe Jeanty et al. "Upscaling and continuous operation of electrochemical CO<sub>2</sub> to CO conversion in aqueous solutions on silver gas diffusion electrodes". In: *Journal of CO<sub>2</sub> Utilization* 24 (Mar. 2018), pp. 454–462. ISSN: 22129820. DOI: 10.1016/j.jcou.2018.01.011.
- [51] Miguel Duarte et al. "Electrochemical Reduction of CO<sub>2</sub>: Effect of Convective CO<sub>2</sub> Supply in Gas Diffusion Electrodes". In: *ChemElectroChem* 6.22 (Nov. 2019), pp. 5596–5602. ISSN: 21960216. DOI: 10.1002/ce1c.201901454.
- [52] B. Endrődi et al. *Continuous-flow electroreduction of carbon dioxide*. 2017. DOI: 10.1016/j.pecs.2017.05.005.
- [53] Cao Thang Dinh et al. "High rate, selective, and stable electroreduction of CO<sub>2</sub> to CO in basic and neutral media". In: *ACS Energy Letters* 3.11 (Nov. 2018), pp. 2835–2840. ISSN: 23808195. DOI: 10.1021/acsenenergylett.8b01734.
- [54] Thomas Haas et al. "Technical photosynthesis involving CO<sub>2</sub> electrolysis and fermentation". In: *Nature Catalysis* 1.1 (Jan. 2018), pp. 32–39. ISSN: 25201158. DOI: 10.1038/s41929-017-0005-1.

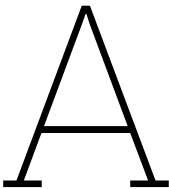
- [55] Sichao Ma et al. "Carbon nanotube containing Ag catalyst layers for efficient and selective reduction of carbon dioxide". In: *Journal of Materials Chemistry A* 4.22 (2016), pp. 8573–8578. ISSN: 20507496. DOI: 10.1039/c6ta00427j.
- [56] Riming Wang et al. "Maximizing Ag Utilization in High-Rate CO<sub>2</sub> Electrochemical Reduction with a Coordination Polymer-Mediated Gas Diffusion Electrode". In: *ACS Energy Letters* 4.8 (Aug. 2019), pp. 2024–2031. ISSN: 23808195. DOI: 10.1021/acseenergylett.9b01509.
- [57] Danielle A. Salvatore et al. "Electrolysis of Gaseous CO<sub>2</sub> to CO in a Flow Cell with a Bipolar Membrane". In: *ACS Energy Letters* 3.1 (Jan. 2018), pp. 149–154. ISSN: 23808195. DOI: 10.1021/acseenergylett.7b01017.
- [58] Jonathan P. Edwards et al. "Efficient electrocatalytic conversion of carbon dioxide in a low-resistance pressurized alkaline electrolyzer". In: *Applied Energy* 261 (Mar. 2020). ISSN: 03062619. DOI: 10.1016/j.apenergy.2019.114305.
- [59] David Reinisch et al. "Various CO<sub>2</sub>-to-CO Electrolyzer Cell and Operation Mode Designs to avoid CO<sub>2</sub>-Crossover from Cathode to Anode". In: *Zeitschrift für Physikalische Chemie* 234.6 (June 2020), pp. 1115–1131. ISSN: 09429352. DOI: 10.1515/zpch-2019-1480.
- [60] Woong Hee Lee et al. "Highly selective and scalable CO<sub>2</sub> to CO - Electrolysis using coral-nanostructured Ag catalysts in zero-gap configuration". In: *Nano Energy* 76 (Oct. 2020). ISSN: 22112855. DOI: 10.1016/j.nanoen.2020.105030.
- [61] Jerry J. Kaczur et al. "Carbon dioxide and water electrolysis using new alkaline stable anion membranes". In: *Frontiers in Chemistry* 6.JUL (2018). ISSN: 22962646. DOI: 10.3389/fchem.2018.00263.
- [62] Zengcai Liu et al. "CO<sub>2</sub> Electrolysis to CO and O<sub>2</sub> at High Selectivity, Stability and Efficiency Using Sustainion Membranes". In: *Journal of The Electrochemical Society* 165.15 (2018), J3371–J3377. ISSN: 0013-4651. DOI: 10.1149/2.0501815jes.
- [63] Sumit Verma et al. "Insights into the Low Overpotential Electroreduction of CO<sub>2</sub> to CO on a Supported Gold Catalyst in an Alkaline Flow Electrolyzer". In: *ACS Energy Letters* 3.1 (Jan. 2018), pp. 193–198. ISSN: 23808195. DOI: 10.1021/acseenergylett.7b01096.
- [64] B. Endrudi et al. "High carbonate ion conductance of a robust PiperION membrane allows industrial current density and conversion in a zero-gap carbon dioxide electrolyzer cell". In: *Energy and Environmental Science* 13.11 (Nov. 2020), pp. 4098–4105. ISSN: 17545706. DOI: 10.1039/d0ee02589e.
- [65] Tengfei Li et al. "Conversion of Bicarbonate to Formate in an Electrochemical Flow Reactor". In: *ACS Energy Letters* 5.8 (Aug. 2020), pp. 2624–2630. ISSN: 23808195. DOI: 10.1021/acseenergylett.0c01291.
- [66] Zishuai Zhang et al. "Porous metal electrodes enable efficient electrolysis of carbon capture solutions". In: *Energy and Environmental Science* 15.2 (Feb. 2022), pp. 705–713. ISSN: 17545706. DOI: 10.1039/d1ee02608a.
- [67] Eric W. Lees et al. "Continuum Model to Define the Chemistry and Mass Transfer in a Bicarbonate Electrolyzer". In: *ACS Energy Letters* 7.2 (Feb. 2022), pp. 834–842. ISSN: 23808195. DOI: 10.1021/acseenergylett.1c02522.
- [68] Carlos Larrea et al. "Multi-parameter study of CO<sub>2</sub> electrochemical reduction from concentrated bicarbonate feed". In: *Journal of CO<sub>2</sub> Utilization* 57 (Mar. 2022). ISSN: 22129820. DOI: 10.1016/j.jcou.2021.101878.
- [69] Eric Yongwook Kim, Lees and Chaitanya Donde. "2023 Kim - Electrochemical capture and conversion of CO<sub>2</sub> into syngas". In: (2023).
- [70] Peter Lobaccaro et al. "Effects of temperature and gas-liquid mass transfer on the operation of small electrochemical cells for the quantitative evaluation of CO<sub>2</sub> reduction electrocatalysts". In: *Physical Chemistry Chemical Physics* 18.38 (2016), pp. 26777–26785. ISSN: 14639076. DOI: 10.1039/c6cp05287h.
- [71] Geonhui Lee et al. "CO<sub>2</sub> electroreduction to multicarbon products from carbonate capture liquid". In: *Joule* 7.6 (June 2023), pp. 1277–1288. ISSN: 25424351. DOI: 10.1016/j.joule.2023.05.003.

- [72] Wesley Luc et al. "SO<sub>2</sub>-Induced Selectivity Change in CO<sub>2</sub> Electroreduction". In: *Journal of the American Chemical Society* (June 2019). ISSN: 15205126. DOI: 10.1021/jacs.9b03215.
- [73] Adnan Ozden et al. "High-rate and efficient ethylene electrosynthesis using a catalyst/promoter-/transport layer". In: *ACS Energy Letters* 5.9 (Sept. 2020), pp. 2811–2818. ISSN: 23808195. DOI: 10.1021/acsenergylett.0c01266.
- [74] Abebe Reda Woldu et al. *Electrochemical CO<sub>2</sub> reduction (CO<sub>2</sub>RR) to multi-carbon products over copper-based catalysts*. Mar. 2022. DOI: 10.1016/j.ccr.2021.214340.
- [75] Jungkuk Lee, Hengzhou Liu, and Wenzhen Li. "Bicarbonate Electroreduction to Multicarbon Products Enabled by Cu/Ag Bilayer Electrodes and Tailored Microenvironments". In: *ChemSusChem* 15.22 (Nov. 2022). ISSN: 1864564X. DOI: 10.1002/cssc.202201329.
- [76] Álvaro A. Ramírez-Santos, Christophe Castel, and Eric Favre. "Utilization of blast furnace flue gas: Opportunities and challenges for polymeric membrane gas separation processes". In: *Journal of Membrane Science* 526 (2017), pp. 191–204. ISSN: 18733123. DOI: 10.1016/j.memsci.2016.12.033.
- [77] Pablo E Duarte et al. *Achieving Carbon Free Emissions via the ENERGIRON DR Process*. Tech. rep.
- [78] Clare Anderson et al. "Developments in the CO<sub>2</sub>CRC UNO MK 3 process: A multi-component solvent process for large scale CO<sub>2</sub> capture". In: *Energy Procedia*. Vol. 37. Elsevier Ltd, 2013, pp. 225–232. DOI: 10.1016/j.egypro.2013.05.106.
- [79] Zheng Zhang et al. *Membrane Electrode Assembly for Electrocatalytic CO<sub>2</sub> Reduction: Principle and Application*. July 2023. DOI: 10.1002/anie.202302789.
- [80] Dipayan Sanyav, Neeraj Vasishtha, and Deoki N Saraf. *Modeling of Carbon Dioxide Absorber Using Hot Carbonate Process*. Tech. rep. 1988, pp. 2149–2156. URL: <https://pubs.acs.org/sharingguidelines>.
- [81] Kathryn A. Mumford et al. "Post-combustion capture of CO<sub>2</sub>: Results from the solvent absorption capture plant at hazelwood power station using potassium carbonate solvent". In: *Energy and Fuels*. Vol. 26. 1. American Chemical Society, Jan. 2012, pp. 138–146. DOI: 10.1021/ef201192n.
- [82] Kathryn H. Smith et al. "Pre-combustion capture of CO<sub>2</sub>-Results from solvent absorption pilot plant trials using 30wt% potassium carbonate and boric acid promoted potassium carbonate solvent". In: *International Journal of Greenhouse Gas Control* 10 (2012), pp. 64–73. ISSN: 17505836. DOI: 10.1016/j.ijggc.2012.05.018.
- [83] M. R. Bohloul et al. "Experimental and analytical study of solubility of carbon dioxide in aqueous solutions of potassium carbonate". In: *International Journal of Greenhouse Gas Control* 29 (2014), pp. 169–175. ISSN: 17505836. DOI: 10.1016/j.ijggc.2014.08.009.
- [84] P. Behr et al. "Kinetic study on promoted potassium carbonate solutions for CO<sub>2</sub> capture from flue gas". In: *Energy Procedia*. Vol. 4. Elsevier Ltd, 2011, pp. 85–92. DOI: 10.1016/j.egypro.2011.01.027.
- [85] Stylianos Pachitsas and Davide Bonalumi. "Parametric investigation of CO<sub>2</sub> capture from industrial flue gases using aqueous mixtures of ammonia (NH<sub>3</sub>) and potassium carbonate (K<sub>2</sub>CO<sub>3</sub>)". In: *International Journal of Greenhouse Gas Control* 114 (Feb. 2022). ISSN: 17505836. DOI: 10.1016/j.ijggc.2021.103567.
- [86] Ajam Yakub Shekh et al. *Recent advancements in carbonic anhydrase-driven processes for CO<sub>2</sub> sequestration: Minireview*. July 2012. DOI: 10.1080/10643389.2011.556884.
- [87] Louis Fradette, Sylvain Lefebvre, and Jonathan Carley. "Demonstration Results of Enzyme-Accelerated CO<sub>2</sub> Capture". In: *Energy Procedia*. Vol. 114. Elsevier Ltd, 2017, pp. 1100–1109. DOI: 10.1016/j.egypro.2017.03.1263.
- [88] Arthur G. Fink et al. "Electrolytic conversion of carbon capture solutions containing carbonic anhydrase". In: *Journal of Inorganic Biochemistry* 231 (June 2022). ISSN: 18733344. DOI: 10.1016/j.jinorgbio.2022.111782.

- [89] Hussain M. Almajed et al. "Closing the Loop: Unexamined Performance Trade-Offs of Integrating Direct Air Capture with (Bi)carbonate Electrolysis". In: *ACS Energy Letters* (May 2024), pp. 2472–2483. ISSN: 2380-8195. DOI: 10.1021/acsenerylett.4c00807. URL: <https://pubs.acs.org/doi/10.1021/acsenerylett.4c00807>.
- [90] Kurt Zenz House et al. "Economic and energetic analysis of capturing CO<sub>2</sub> from ambient air". In: (1998). DOI: 10.1073/pnas.1012253108/-/DCSupplemental. URL: [www.pnas.org/lookup/suppl/](http://www.pnas.org/lookup/suppl/).
- [91] Tianqi Gao et al. "Techno-economic Analysis and Carbon Footprint Accounting for Industrial CO<sub>2</sub> Electrolysis Systems". In: *Energy and Fuels* 37.23 (Dec. 2023), pp. 17997–18008. ISSN: 15205029. DOI: 10.1021/acs.energyfuels.3c01581.
- [92] Théo Alerte et al. "Scale-Dependent Techno-Economic Analysis of CO<sub>2</sub> Capture and Electroreduction to Ethylene". In: *ACS Sustainable Chemistry and Engineering* 11.43 (Oct. 2023), pp. 15651–15662. ISSN: 21680485. DOI: 10.1021/acssuschemeng.3c04373.
- [93] Marta Moreno-Gonzalez et al. "Carbon-neutral fuels and chemicals: Economic analysis of renewable syngas pathways via CO<sub>2</sub> electrolysis". In: *Energy Conversion and Management* 244 (Sept. 2021). ISSN: 01968904. DOI: 10.1016/j.enconman.2021.114452.
- [94] Xuping Li et al. "Greenhouse Gas Emissions, Energy Efficiency, and Cost of Synthetic Fuel Production Using Electrochemical CO<sub>2</sub> Conversion and the Fischer-Tropsch Process". In: *Energy and Fuels* 30.7 (July 2016), pp. 5980–5989. ISSN: 15205029. DOI: 10.1021/acs.energyfuels.6b00665.
- [95] A. Cousins, L. T. Wardhaugh, and P. H.M. Feron. *A survey of process flow sheet modifications for energy efficient CO<sub>2</sub> capture from flue gases using chemical absorption*. 2011. DOI: 10.1016/j.ijggc.2011.01.002.
- [96] Kyung Jae Lee et al. "Correlating the Reverse Water-Gas Shift Reaction with Surface Chemistry: The Influence of Reactant Gas Exposure to Ni(100)". In: *ACS Catalysis* 13.13 (July 2023), pp. 9041–9050. ISSN: 21555435. DOI: 10.1021/acscatal.3c01517.
- [97] Sandra Dermühl and Uwe Riedel. "A comparison of the most promising low-carbon hydrogen production technologies". In: *Fuel* 340 (May 2023). ISSN: 00162361. DOI: 10.1016/j.fuel.2023.127478.
- [98] Iris Burgers et al. "The Effect of Electrolyte pH and Impurities on the Stability of Electrolytic Bicarbonate Conversion". In: *ChemSusChem* (Sept. 2024). ISSN: 1864-5631. DOI: 10.1002/cssc.202401631. URL: <https://chemistry-europe.onlinelibrary.wiley.com/doi/10.1002/cssc.202401631>.
- [99] L Niel Plummer and Eurybiades Busenberg. *101 I-1040 Q Pqamon Prcn Ltd*. Tech. rep. 1982.
- [100] Mahinder Ramdin et al. "Electroreduction of CO<sub>2</sub>/CO to C<sub>2</sub>Products: Process Modeling, Downstream Separation, System Integration, and Economic Analysis". In: *Industrial and Engineering Chemistry Research* 60.49 (Dec. 2021), pp. 17862–17880. ISSN: 15205045. DOI: 10.1021/acs.iecr.1c03592.
- [101] National Institute of Standards and U.S. Department of Commerce Technology (NIST). *Hydrogen Sulfide, ch H<sub>2</sub>S chH<sub>2</sub>S, Thermophysical Properties*. 2024.
- [102] Stacy C Davis and Robert G Boundy. *Transportation Energy Data Book: Edition 40*. Tech. rep.
- [103] Chemical Engineering Magazine. *Plant Cost Index Archives*. June 2024.
- [104] Thijs Verboon, Sander Blom, and Timothy Bender. *70770-Openbaar Effecten van een productiesubsidie voor elektrolyzers*. Tech. rep. 2023.
- [105] *Hydrogen Economy Outlook Key messages*. Tech. rep. 2020.
- [106] L Eblé and M Weeda. *Evaluation of the levelised cost of hydrogen based on proposed electrolyser projects in the Netherlands Renewable Hydrogen Cost Element Evaluation Tool (RHyCEET) TNO Public*. Tech. rep. 2024. URL: [www.tno.nl](http://www.tno.nl).
- [107] EU Hydrogen Observatory. *Levelised Cost of Hydrogen Calculator*. 2024.
- [108] Wood Mackenzie. *Hydrogen Costs in 2024: What You Need to Know*. 2023.

- [109] Emiel van den Toorn. *Afnameverplichting groene waterstof*. Tech. rep. URL: [www.ce.nl](http://www.ce.nl).
- [110] Frank Radosits, Amela Ajanovic, and Simon Pratschner. “Costs and perspectives of synthetic methane and methanol production using carbon dioxide from biomass-based processes”. In: *Journal of Sustainable Development of Energy, Water and Environment Systems* 12.2 (June 2024), pp. 1–21. DOI: 10.13044/j.sdewes.d12.0484.
- [111] Ralf Peters et al. “A techno economic analysis of the power to gas route”. In: *Journal of CO2 Utilization* 34 (Dec. 2019), pp. 616–634. ISSN: 22129820. DOI: 10.1016/j.jcou.2019.07.009.
- [112] McKinsey & Company. *Global Energy Perspective 2023: Hydrogen Outlook*. Tech. rep. 2023.
- [113] Haoyu Wang. *Mechanism Design for Container Sharing under the Impact of Carbon Tax*. Tech. rep. 2023.
- [114] Enerdata. *Carbon price forecast under the EU ETS*. Tech. rep. 2030.
- [115] Yuguang C. Li et al. “CO2 Electroreduction from Carbonate Electrolyte”. In: *ACS Energy Letters* 4.6 (June 2019), pp. 1427–1431. ISSN: 23808195. DOI: 10.1021/acsenenergylett.9b00975.
- [116] Phil De Luna et al. *What would it take for renewably powered electrosynthesis to displace petrochemical processes?* 2019. DOI: 10.1126/science.aav3506.
- [117] Qi Lu and Feng Jiao. “Electrochemical CO2 reduction: Electrocatalyst, reaction mechanism, and process engineering”. In: *Nano Energy* 29 (Nov. 2016), pp. 439–456. ISSN: 22112855. DOI: 10.1016/j.nanoen.2016.04.009.
- [118] *ICIS: Independent Commodity Intelligence Services*.
- [119] U.S. Energy Information Administration (EIA). <https://www.eia.gov>.
- [120] Ratan Raj et al. “A techno-economic assessment of the liquefied natural gas (LNG) production facilities in Western Canada”. In: *Sustainable Energy Technologies and Assessments* 18 (Dec. 2016), pp. 140–152. ISSN: 22131388. DOI: 10.1016/j.seta.2016.10.005.





# Appendix

## A.1. DRI processes

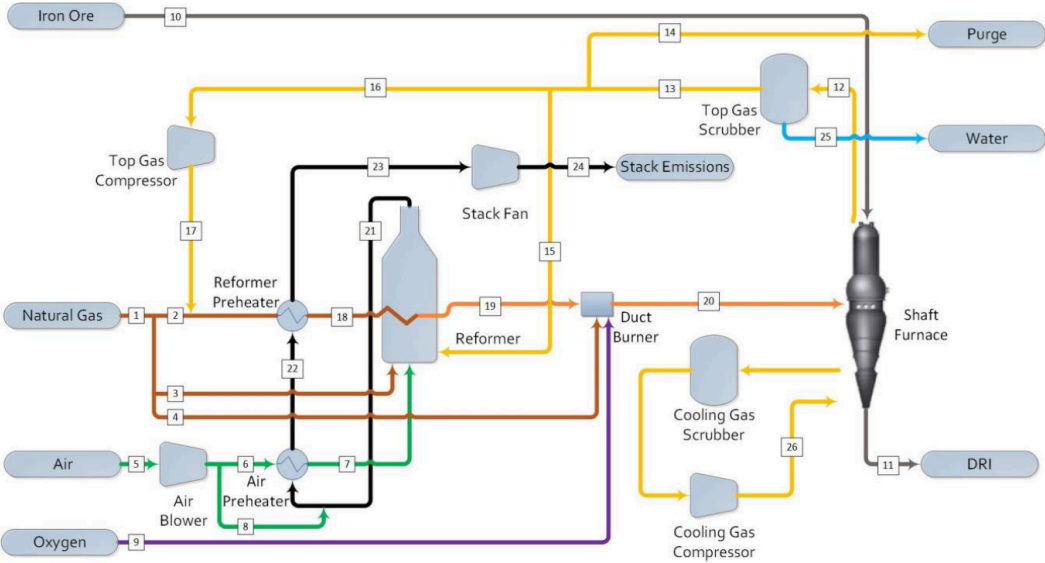


Figure A.1: Simplified process configuration for Midrex process [27].

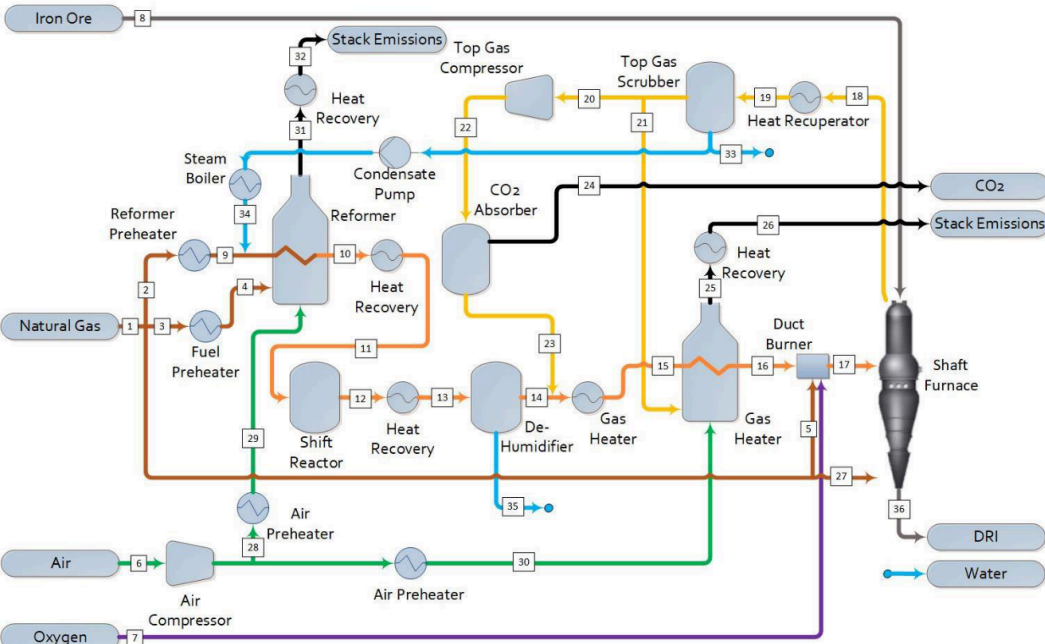


Figure A.2: Simplified process configuration for Energiron III process [27].

## A.2. Economic analysis of product pathways

With CO<sub>2</sub>RR, many different pathways can be taken to produce a wide range of products, depending mainly on the choice of catalyst in the electrolyser [74]. An overview of potential products and pathways is displayed in Figure A.3, leaving the question: which CO<sub>2</sub> reduction product should be targeted for commercialization? The answer to this question strongly depends on the supply and demand of products, electricity prices and the state of technology, among other factors. As a result, a general consensus on this topic has not been reached.

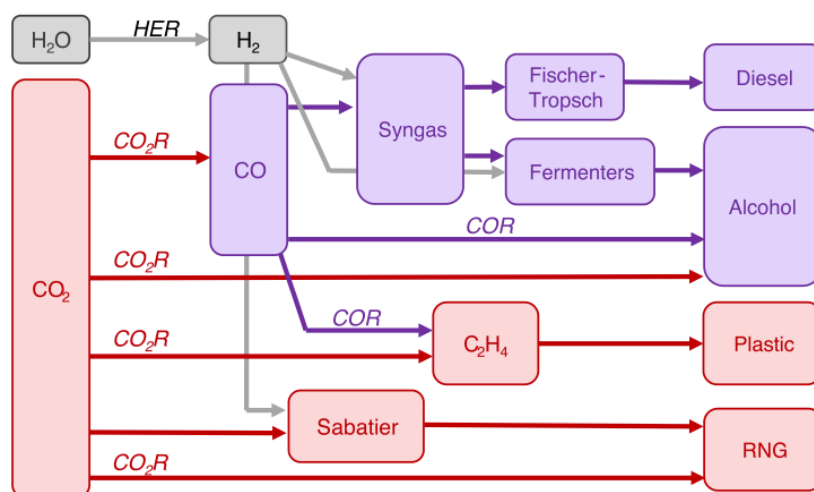


Figure A.3: Overview of products pathways for CO<sub>2</sub>RR [116].

To guide the discussion on product selection in CO<sub>2</sub>RR and to narrow the focus of this thesis, an economic assessment has been performed. Jouny et al. compiled data on the seven major products and their electron consumption, market price (\$/kg), normalized price (\$/electron), and annual global production (in Mtonne). This data, presented in Table A.1, was obtained by averaging values from various sources, including the Independent Chemical Information Service (ICIS), the U.S. Energy Information Administration (EIA), and various published works [29, 117, 118, 119].

Table A.1: CO<sub>2</sub>RR Products Data [29]

| Product     | Required Electrons | Market Price (\$/kg) | Normalized Price (\$/electron) × 10 <sup>3</sup> | Annual Global Production (Mtonne) |
|-------------|--------------------|----------------------|--|-----------------------------------|
| CO (syngas) | 2                  | 0,06                 | 0,8  | 150,0                             |
| CO          | 2                  | 0,60                 | 8,0  | 3,6                               |
| Formic Acid | 2                  | 0,74                 | 16,1   | 0,6                               |
| Methanol    | 6                  | 0,58                 | 3,1  | 110,0                             |
| Methane     | 8                  | 0,18                 | 0,4  | 250,0                             |
| Ethylene    | 12                 | 1,30                 | 3,0  | 140,0                             |
| Ethanol     | 12                 | 1,00                 | 3,8  | 77,0                              |
| n-Propanol  | 18                 | 1,43                 | 4,8  | 0,2                               |

The following requirements for potential products to ensure their economic feasibility have been established:

1. **Large Global Market Capacity:** Since the CO<sub>2</sub>RR process is scaled to industrial size with large mass flows of flue gases, production will be high. If a product has a small market capacity, the market could become flooded, leading to lower prices that would significantly decrease profitability and could invalidate the Techno-Economic Analysis (TEA).
2. **Product Suitability for On-site Use or Off-site Sale:** In the steel industry, where many feed-streams are used, integrating CO<sub>2</sub>RR technology into the steelmaking process could make the TEA more viable. Conversely, if on-site use is not feasible, the product must meet specific grade requirements for off-site selling, thereby enhancing profitability.

- 3. Large Normalized Market Price:** The product must have a large normalized market price, meaning the price per electron. This reflects the market price relative to the number of electrons (and thus energy) required by the formation reaction.
- 4. Competitiveness with Traditional Production Methods:** To adopt the CO<sub>2</sub>RR process, the new process must offer significant advantages over traditional methods, both in terms of energy use and profitability.

Formic acid and n-propanol are not suitable as products for an industrial-scale CO<sub>2</sub>RR process due to their limited market size (0,6 MT and 0,2 MT, respectively). A typical flue gas from a blast furnace in the steel industry has a mass flow on the order of magnitude of 10<sup>3</sup> tonnes/hour. As a consequence, the production would far exceed the market capacity, resulting in flooding of the market and significantly lower prices, making these products economically unattractive. Similarly, purifying CO suffers from the same small market capacity issue (3,6 MT), and the purification process is known to be costly, resulting in a 10-fold increase in price compared to syngas. While methane has the largest market size (250 MT), its abundance in natural resources has led to a low normalized market price (0,4 \$/electron), making it difficult for the CO<sub>2</sub>RR process to be competitive. Syngas emerges as a favourable product since it can be utilized on-site in steelmaking processes and offers a decent normalized price, alongside its versatility as a feedstock for chemical processes. C<sub>2</sub>+ products, most notably methanol, ethylene, and ethanol stand out as highly desirable products with significant market capacity and decent normalized market prices. These compounds find extensive industrial applications as chemical precursors, fuel additives, and energy sources. Moreover, these products can be synthesized in various FEs using copper-based catalysts [100].

### A.3. Overview of cases

This section provides a detailed overview of the cases, with design requirements highlighted in orange.

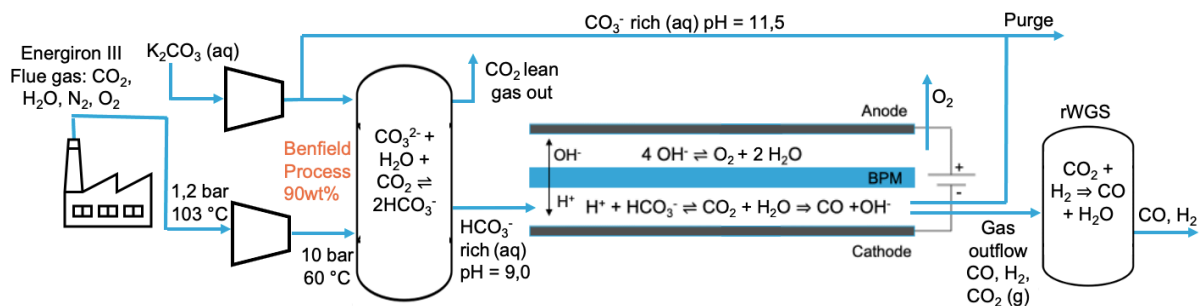


Figure A.4: Schematic overview of Case I: design for 90wt% capture in the absorption column.

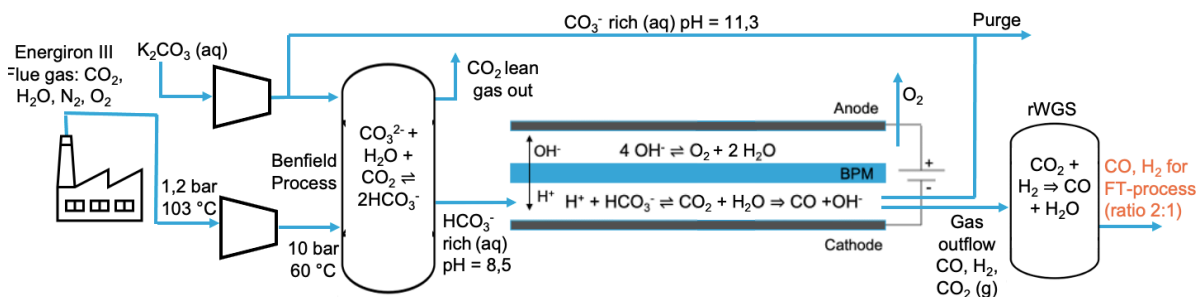


Figure A.5: Schematic overview of Case II: Design for syngas fit for FT-process.

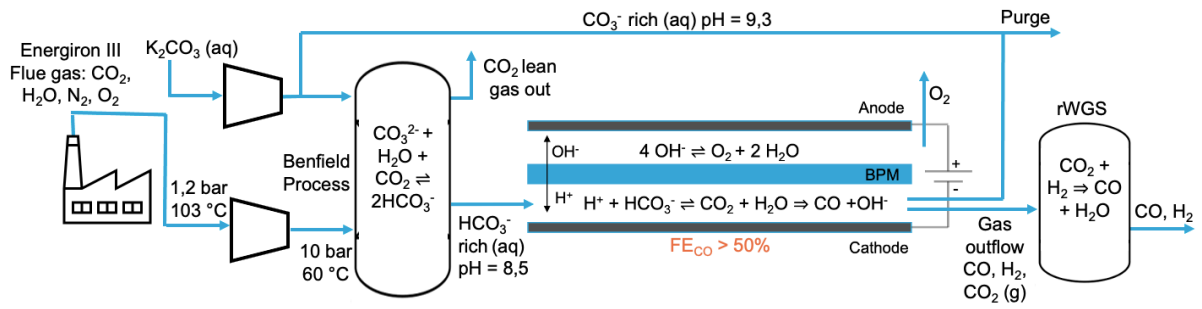


Figure A.6: Schematic overview of Case III: design for FE > 50%.

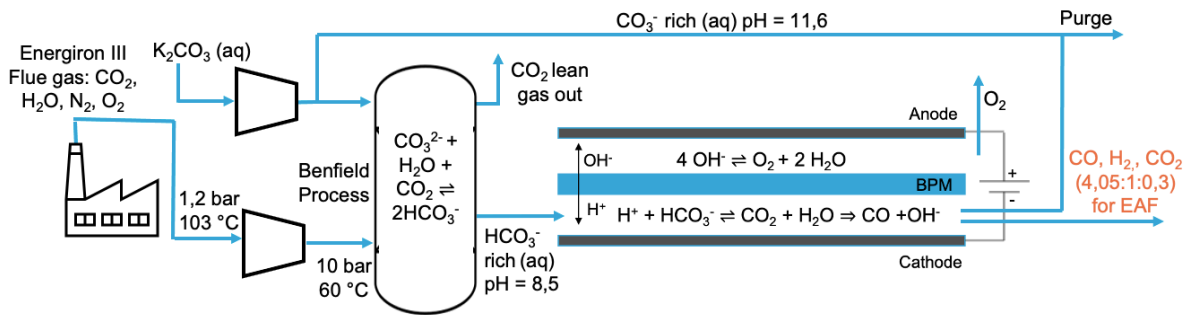


Figure A.7: schematic overview of Case IV: design syngas fit for EAF.

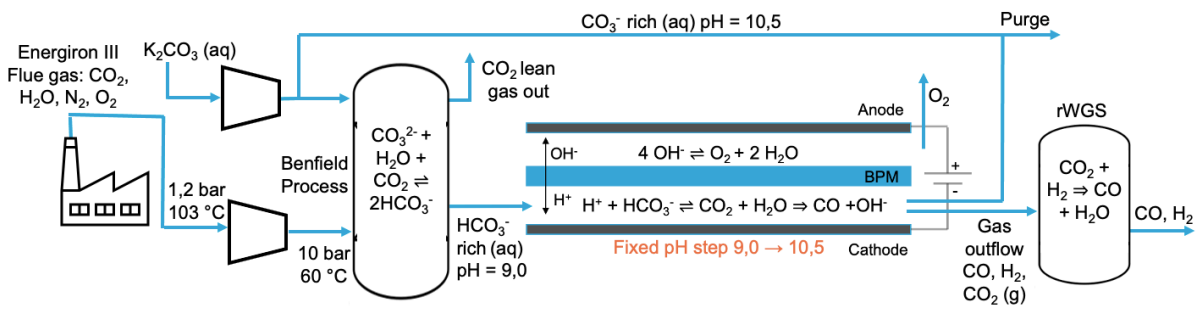


Figure A.8: Schematic overview of Case V: mid-pH step.

## A.4. Electrolyser model inputs

| Category       | Parameter                                | Description   | Units             |
|----------------|--|---|-------------------|
| <b>Inputs</b>  |  |   |                   |
| F(Abs)         | $[\text{HCO}_3^-]_{\text{in}}$           | Inlet concentration of bicarbonate feed stream      | mol/L             |
| F(Abs)         | Flow rate <sub>in</sub>                  | HCO <sub>3</sub> <sup>-</sup> feed stream flow rate | m <sup>3</sup> /s |
| F(pH)          | FE                                       | Faradaic efficiency                                 | %                 |
| F(pH)          | CO <sub>2</sub> utilization              | Fraction of CO <sub>2</sub> utilized                | %                 |
| F(pH)          | HCO <sub>3</sub> <sup>-</sup> conversion | Fraction of bicarbonate converted                   | %                 |
| Constants      | CD                                       | Current density                                     | A/m <sup>2</sup>  |
| Constants      | V  | Voltage Measured                                    | V                 |
| <b>Outputs</b> |  |   |                   |
| Produced       | CO <sub>produced</sub>                   | Amount of CO produced                               | mol/s             |
| Produced       | H <sub>2</sub> produced                  | Amount of H <sub>2</sub> produced                   | mol/s             |
| Unreacted      | CO <sub>2</sub> unreacted                | Amount of CO <sub>2</sub> unreacted                 | mol/s             |
| Area           | Area <sub>electrolyser</sub>             | Surface area of the electrolyser                    | m <sup>2</sup>    |
| Power          | P <sub>electrolyser</sub>                | Power consumption of the electrolyser               | W                 |

**Table A.2:** Overview of input and output parameters with descriptions and units.

### A.4.1. Bjerrum plot

The function `carbonate_species` calculates the concentrations of different carbonate species (CO<sub>2</sub>, HCO<sub>3</sub><sup>-</sup>, and CO<sub>3</sub><sup>2-</sup>) in a solution based on the pH and dissociation constants  $K_1$  and  $K_2$ .

```
def carbonate_species(pH, K1, K2):
    H = 10**(-pH)
    CO2 = 1 / (1 + K1/H + (K1*K2)/(H**2))
    HCO3 = (K1/H) / (1 + K1/H + (K1*K2)/(H**2))
    CO3 = (K1*K2)/(H**2) / (1 + K1/H + (K1*K2)/(H**2))
    return CO2, HCO3, CO3
```

In mathematical terms, the concentrations of the carbonate species are calculated as follows:

- $\text{H}^+ = 10^{-\text{pH}}$
- $\text{CO}_2 = \frac{1}{1 + \frac{K_1}{\text{H}^+} + \frac{K_1 K_2}{\text{H}^{+2}}}$
- $\text{HCO}_3^- = \frac{\frac{K_1}{\text{H}^+}}{1 + \frac{K_1}{\text{H}^+} + \frac{K_1 K_2}{\text{H}^{+2}}}$
- $\text{CO}_3^{2-} = \frac{\frac{K_1 K_2}{\text{H}^{+2}}}{1 + \frac{K_1}{\text{H}^+} + \frac{K_1 K_2}{\text{H}^{+2}}}$

The function returns the concentrations of CO<sub>2</sub>, HCO<sub>3</sub><sup>-</sup>, and CO<sub>3</sub><sup>2-</sup>.

Table A.3 denotes the pKa values used in the model.

| Species Transition  | pKa (1 bar, 20°C) | pKa (10 bar, 60°C) |
|---|-------------------|--------------------|
| $\text{H}_2\text{CO}_3 \rightarrow \text{HCO}_3^- + \text{H}^+$ | 6,3               | 5,9                |
| $\text{HCO}_3^- \rightarrow \text{CO}_3^{2-} + \text{H}^+$      | 10,3              | 9,9                |

**Table A.3:** pKa values for the dissociation of carbonic acid and bicarbonate under different temperature and pressure conditions.

## A.4.2. Inputs for ambient conditions (1 bar, 20°C)

| pH   | Molefrac $\text{HCO}_3^-$ | Molefrac $\text{CO}_3^{2-}$ | $\text{FE}_{\text{CO}}$ | $\text{CO}_2$ Utilization |
|------|---------------------------|-----------------------------|-------------------------|---------------------------|
| 8.5  | 0.98                      | 0.02                        | 56%                     | 36%                       |
| 9    | 0.95                      | 0.05                        | 50%                     | 56%                       |
| 9.5  | 0.86                      | 0.14                        | 31%                     | 69%                       |
| 10   | 0.67                      | 0.33                        | 18%                     | 80%                       |
| 10.5 | 0.39                      | 0.61                        | 10%                     | 85%                       |
| 11   | 0.17                      | 0.83                        | 5%                      | 90%                       |
| 11.5 | 0.06                      | 0.94                        | 3%                      | 92%                       |

**Table A.4:** Mole fractions of  $\text{HCO}_3^-$  and  $\text{CO}_3^{2-}$ ,  $\text{FE}_{\text{CO}}$ , and  $\text{CO}_2$  utilization at different pH levels.

| Steps       | Conversion of $\text{HCO}_3^-$ | $\text{FE}_{\text{CO}}$ | $\text{CO}_2$ Utilization |
|-------------|--------------------------------|-------------------------|---------------------------|
| 8.5 → 9.0   | 3%                             | 53%                     | 46%                       |
| 9.0 → 9.5   | 9%                             | 41%                     | 62%                       |
| 9.5 → 10.0  | 23%                            | 25%                     | 74%                       |
| 10.0 → 10.5 | 42%                            | 14%                     | 83%                       |
| 10.5 → 11.0 | 57%                            | 8%                      | 88%                       |
| 11.0 → 11.5 | 64%                            | 4%                      | 91%                       |

**Table A.5:** Model inputs ambient: Conversion of  $\text{HCO}_3^-$ ,  $\text{FE}_{\text{CO}}$ , and  $\text{CO}_2$  utilization across different pH steps under ambient conditions.

## A.4.3. Inputs for operating conditions (10 bar, 60°C)

Worst case

| pH   | Molefrac $\text{HCO}_3^-$ | Molefrac $\text{CO}_3^{2-}$ | $\text{FE}_{\text{CO}}$ | $\text{CO}_2$ Utilization |
|------|---------------------------|-----------------------------|-------------------------|---------------------------|
| 8.5  | 0.96                      | 0.05                        | 62%                     | 25%                       |
| 9    | 0.88                      | 0.15                        | 55%                     | 39%                       |
| 9.5  | 0.69                      | 0.36                        | 34%                     | 48%                       |
| 10   | 0.41                      | 0.64                        | 20%                     | 56%                       |
| 10.5 | 0.18                      | 0.85                        | 11%                     | 60%                       |
| 11   | 0.07                      | 0.95                        | 6%                      | 63%                       |
| 11.5 | 0.02                      | 0.98                        | 3%                      | 64%                       |

**Table A.6:** Worst case: pH, mole fractions of  $\text{HCO}_3^-$  and  $\text{CO}_3^{2-}$ ,  $\text{FE}_{\text{CO}}$ , and  $\text{CO}_2$  utilization percentages.

| Steps       | Conversion of $\text{HCO}_3^-$ | $\text{FE}_{\text{CO}}$ | $\text{CO}_2$ Utilization |
|-------------|--------------------------------|-------------------------|---------------------------|
| 8.5 → 9.0   | 8%                             | 58%                     | 32%                       |
| 9.0 → 9.5   | 21%                            | 45%                     | 44%                       |
| 9.5 → 10.0  | 40%                            | 27%                     | 52%                       |
| 10.0 → 10.5 | 56%                            | 15%                     | 58%                       |
| 10.5 → 11.0 | 64%                            | 8%                      | 61%                       |
| 11.0 → 11.5 | 67%                            | 4%                      | 64%                       |

**Table A.7:** Model inputs Worst case: Steps, Conversion of  $\text{HCO}_3^-$ ,  $\text{FE}_{\text{CO}}$ , and  $\text{CO}_2$  utilization percentages.

## Base case

| pH   | Molefrac $\text{HCO}_3^-$ | Molefrac $\text{CO}_3^{2-}$ | $\text{FE}_{\text{CO}}$ | $\text{CO}_2$ Utilization |
|------|---------------------------|-----------------------------|-------------------------|---------------------------|
| 8.5  | 0.96                      | 0.05                        | 73%                     | 29%                       |
| 9    | 0.88                      | 0.15                        | 65%                     | 45%                       |
| 9.5  | 0.69                      | 0.36                        | 40%                     | 55%                       |
| 10   | 0.41                      | 0.64                        | 23%                     | 64%                       |
| 10.5 | 0.18                      | 0.85                        | 13%                     | 68%                       |
| 11   | 0.07                      | 0.95                        | 7%                      | 72%                       |
| 11.5 | 0.02                      | 0.98                        | 4%                      | 74%                       |

**Table A.8:** Base case: pH, mole fractions of  $\text{HCO}_3^-$  and  $\text{CO}_3^{2-}$ ,  $\text{FE}_{\text{CO}}$ , and  $\text{CO}_2$  utilization percentages.

| Steps       | Conversion of $\text{HCO}_3^-$ | $\text{FE}_{\text{CO}}$ | $\text{CO}_2$ Utilization |
|-------------|--------------------------------|-------------------------|---------------------------|
| 8.5 → 9.0   | 8%                             | 69%                     | 37%                       |
| 9.0 → 9.5   | 21%                            | 53%                     | 50%                       |
| 9.5 → 10.0  | 40%                            | 32%                     | 60%                       |
| 10.0 → 10.5 | 56%                            | 18%                     | 66%                       |
| 10.5 → 11.0 | 64%                            | 10%                     | 70%                       |
| 11.0 → 11.5 | 67%                            | 5%                      | 73%                       |

**Table A.9:** Model inputs Base case: Steps, Conversion of  $\text{HCO}_3^-$ ,  $\text{FE}_{\text{CO}}$ , and  $\text{CO}_2$  utilization percentages.

## Best case

| pH   | Molefrac $\text{HCO}_3^-$ | Molefrac $\text{CO}_3^{2-}$ | $\text{FE}_{\text{CO}}$ | $\text{CO}_2$ Utilization |
|------|---------------------------|-----------------------------|-------------------------|---------------------------|
| 8.5  | 0.96                      | 0.05                        | 84%                     | 32%                       |
| 9    | 0.88                      | 0.15                        | 75%                     | 50%                       |
| 9.5  | 0.69                      | 0.36                        | 47%                     | 62%                       |
| 10   | 0.41                      | 0.64                        | 27%                     | 72%                       |
| 10.5 | 0.18                      | 0.85                        | 15%                     | 77%                       |
| 11   | 0.07                      | 0.95                        | 8%                      | 81%                       |
| 11.5 | 0.02                      | 0.98                        | 5%                      | 83%                       |

**Table A.10:** Best case: pH, mole fractions of  $\text{HCO}_3^-$  and  $\text{CO}_3^{2-}$ ,  $\text{FE}_{\text{CO}}$ , and  $\text{CO}_2$  utilization percentages.

| Steps       | Conversion of $\text{HCO}_3^-$ | $\text{FE}_{\text{CO}}$ | $\text{CO}_2$ Utilization |
|-------------|--------------------------------|-------------------------|---------------------------|
| 8.5 → 9.0   | 8%                             | 80%                     | 41%                       |
| 9.0 → 9.5   | 21%                            | 61%                     | 56%                       |
| 9.5 → 10.0  | 40%                            | 37%                     | 67%                       |
| 10.0 → 10.5 | 56%                            | 21%                     | 74%                       |
| 10.5 → 11.0 | 64%                            | 11%                     | 79%                       |
| 11.0 → 11.5 | 67%                            | 6%                      | 82%                       |

**Table A.11:** Model inputs Best case: Steps, Conversion of  $\text{HCO}_3^-$ ,  $\text{FE}_{\text{CO}}$ , and  $\text{CO}_2$  utilization percentages.

## A.5. Electrolyser model

### A.5.1. Model constants

| Contents  | Value                   | Unit               |
|---|-------------------------|--------------------|
| Avogadro's number                                       | $6.02 \times 10^{23}$   | -                  |
| Electron charge   | $1.602 \times 10^{-19}$ | C                  |
| Faraday's constant                                      | 96485                   | C/mol              |
| Electrons consumed in CO <sub>2</sub> RR reaction to CO | 2                       | electrons/molecule |
| Electrons consumed in HER                               | 2                       | electrons/molecule |
| Electrons liberated in OER                              | 4                       | electrons/molecule |
| Current Density   | 100                     | mA/cm <sup>2</sup> |

Table A.12: Table of Physical Constants and Other Values.

### A.5.2. Formulas used in electrolyser model

| Parameter                                    | Description  | Formula   | Unit           |
|--|--|---|----------------|
| HCO <sub>3</sub> <sup>-</sup> <sub>BPM</sub> | Bicarbonate ions fed to the bipolar membrane         | $[\text{HCO}_3^-]_{\text{in}} \times \text{Flow rate}$                                      | mol/s          |
| I-CO <sub>2</sub>                            | CO <sub>2</sub> generated at the BPM                 | $[\text{HCO}_3^-] \times \text{conversion factor}$  | mol/s          |
| CO <sub>CO2RR</sub>                          | Carbon monoxide produced at the cathode              | $I - \text{CO}_2 \times \text{CO}_2 \text{ utilization rate}$                               | mol/s          |
| e <sub>CO2RR</sub>                           | Electrons used in CO <sub>2</sub> reduction reaction | $\text{CO} \times \text{electrons per CO}_2\text{RR}$                                       | mol/s          |
| FE <sub>H<sub>2</sub></sub>                  | Faradaic efficiency for H <sub>2</sub> production    | $1 - \text{FE}_{\text{CO}}$   | %              |
| H <sub>2HER</sub>                            | Hydrogen produced at the cathode                     | $\text{FE}_{\text{H}_2} \times \frac{\text{electrons available}}{\text{electrons per HER}}$ | mol/s          |
| O <sub>2OER</sub>                            | Oxygen produced at the anode                         | $\frac{\text{electrons available}}{\text{electrons per OER}}$                               | mol/s          |
| I <sub>tot</sub>                             | Total electrical current                             | $\text{Number of electrons} \times N_A \times e$  | A              |
| A <sub>electrolyser</sub>                    | Required electrolyser area                           | $\frac{I_{\text{tot}}}{\text{current density}}$   | m <sup>2</sup> |
| P <sub>consumed</sub>                        | Total power consumption                              | $I_{\text{tot}} \times \text{cell potential}$   | W              |

Table A.13: Formulas used in the electrolyser model.

## A.6. ASPEN Model for absorption column

This section provides further details on the ASPEN PLUS model developed for the capture column.

### A.6.1. Component list

| Compound                       | Name                  | CAS Number |
|--------------------------------|-----------------------|------------|
| N <sub>2</sub>                 | Nitrogen              | 7727-37-9  |
| H <sub>2</sub> O               | Water                 | 7732-18-5  |
| CO <sub>2</sub>                | Carbon Dioxide        | 124-38-9   |
| KOH                            | Potassium Hydroxide   | 1310-58-3  |
| H <sub>3</sub> O <sup>+</sup>  | Hydronium Ion         | -          |
| OH <sup>-</sup>                | Hydroxide Ion         | -          |
| HCO <sub>3</sub> <sup>-</sup>  | Bicarbonate Ion       | -          |
| CO <sub>3</sub> <sup>2-</sup>  | Carbonate Ion         | -          |
| K <sup>+</sup>                 | Potassium Ion         | -          |
| K <sub>2</sub> CO <sub>3</sub> | Potassium Carbonate   | 584-08-7   |
| KHCO <sub>3</sub>              | Potassium Bicarbonate | 298-14-6   |
| O <sub>2</sub>                 | Oxygen                | 7782-44-7  |
| CO                             | Carbon Monoxide       | 630-08-0   |
| H <sub>2</sub>                 | Hydrogen              | 1333-74-0  |

**Table A.14:** Chemical compounds and their respective CAS numbers as used in ASPEN PLUS. Note: Ions do not have CAS numbers as they are derived from other compounds and are context-dependent.

### A.6.2. Reactions and reaction constants

The reactions and their associated parameters in the Benfield process are derived from the example model available in the ASPEN library for carbon capture using K<sub>2</sub>CO<sub>3</sub>. For equilibrium reactions, the built-in expression for the equilibrium constant ( $K_{eq}$ ) with T in K is used, as shown in Equation A.1.

$$\ln(K_{eq}) = A + \frac{B}{T} + C \ln(T) + DT \quad (\text{A.1})$$

| No. | Reaction   | A       | B        | C        | D |
|-----|--|---------|----------|----------|---|
| 1   | $2 \text{H}_2\text{O} \rightleftharpoons \text{OH}^- + \text{H}_3\text{O}^+$                     | 132.899 | -13445.9 | -22.4773 | 0 |
| 4   | $\text{HCO}_3^- + \text{H}_2\text{O} \rightleftharpoons \text{H}_3\text{O}^+ + \text{CO}_3^{2-}$ | 216.049 | -12431.7 | -35.4819 | 0 |

**Table A.15:** Equilibrium reactions and their corresponding parameters.

Similarly, kinetic expressions for the reactions are modeled using the form shown in Equation A.2 for the kinetic rate constant.

$$\text{Kinetic factor} = kT^n e^{-\frac{E}{RT}} \quad (\text{A.2})$$

| No. | Reaction   | k        | E [cal/mol] |
|-----|--|----------|-------------|
| 2   | $\text{CO}_2 + \text{OH}^- \rightarrow \text{HCO}_3^-$ | 4.32e+13 | 13249       |
| 3   | $\text{HCO}_3^- \rightarrow \text{CO}_2 + \text{OH}^-$ | 2.38e+17 | 29451       |

**Table A.16:** Kinetic reactions and their corresponding rate constants and activation energies.

### A.6.3. Capture fractions chart for CAPSOL process

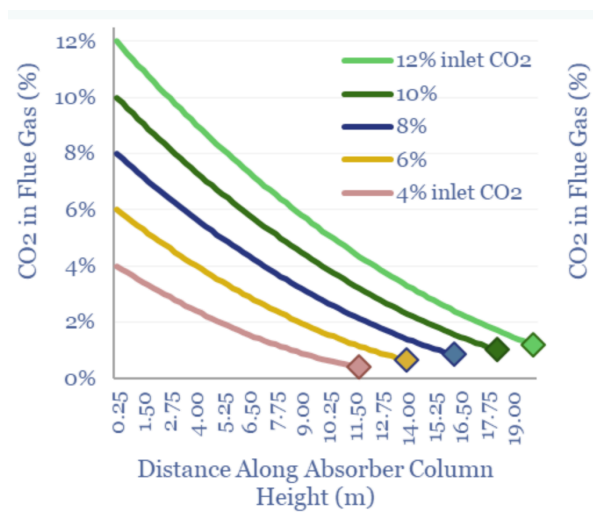


**Figure A.9:** Data on CAPSOL process: Absorption column height versus CO<sub>2</sub> fraction, used for model validation.

### A.6.4. Iteration and optimization

To optimize the electrolyser pH step, sizing, and power consumption while aligning with the performance of the capture column, an iterative process is employed. Initially, the appropriate input parameters and sensitivity variables must be set in the Excel model, as discussed in section 3.2. The next step involves adjusting either the Excel model or the ASPEN model to meet the case-specific design goals.

- **For Case I**, the gas/liquid (G/L) ratio on the absorption column inflow needs to be adjusted in ASPEN to achieve a 90% CO<sub>2</sub> capture rate.
- **For Cases II and IV**, the pH step in Excel must be adjusted to ensure the syngas outflow meets the desired syngas composition ratio.
- **For Case III**, the pH step in Excel should be modified to stop when a FE of 50% is achieved in the base case.
- **For Case V**, the pH is dictated by the design goal of the case, and the absorption column is optimized accordingly.

After these adjustments, the model must be properly sized. The Excel model is configured to maintain a power requirement of 20 MW while keeping the G/L ratio constant. Next, the absorption column is sized to approach 80% flooding. This adjustment may slightly alter the capture rate and electrolyser inflow, requiring a return to the model to verify that the power remains at 20 MW, with further adjustments made if necessary. This iterative process is repeated until all design goals are met—specifically, the case-specific objectives, the 20 MW power target, and the 80% flooding approach. The capture rate, syngas ratios, and 20 MW sizing are adjusted until the error is reduced to below 1%.

## A.7. Formulas for estimating CAPEX

### A.7.1. Electrolyser CAPEX estimation

| Unit Capital Cost (UCC) Electrolyser | Price                                     | Unit               |
|--------------------------------------|---|--------------------|
| MEA costs                            | \$896                                     | USD/m <sup>2</sup> |
| Catalyst costs                       | \$180                                     | USD/m <sup>2</sup> |
| BPM                                  | \$750                                     | USD/m <sup>2</sup> |
| <b>Total stack cost</b>              | <b>\$1,793</b>                            | USD/m <sup>2</sup> |
| CAPEX stack                          | Area × Total stack cost                   | USD                |
| Peripheral equipment factor          | 1.6 / 2 / 2.4                             | [-]                |
| CAPEX Electrolyser equipment         | CAPEX stack × Peripheral equipment factor | USD                |
| Factor UCC                           | 1.4 / 1.65 / 1.9                          | [-]                |
| <b>UCC</b>                           | CAPEX Electrolyser equipment × Factor UCC | USD                |

Table A.17: Breakdown of CAPEX for the Electrolyser in USD.

### A.7.2. Calculation of catalyst costs

| Component                           | Price per unit (USD)     | Loading              | Price per area (USD/m <sup>2</sup> ) |
|-------------------------------------|--------------------------|----------------------|--------------------------------------|
| <b>Anode</b>                        |                          |                      |                                      |
| Ni foam mesh (80 ppi, 2 mm)         | 115 \$/m <sup>2</sup>    | -                    | 115.00                               |
| <b>Cathode</b>                      |                          |                      |                                      |
| Ag catalyst for cathode             | 0.0006 \$/mg             | 1 mg/cm <sup>2</sup> | 5.50                                 |
| GDL for cathode                     | 0.006 \$/cm <sup>2</sup> | -                    | 60.00                                |
| <b>Total Cost (Anode + Cathode)</b> |                          |                      | <b>180.50</b>                        |

Table A.18: Summary of Catalyst and Material Costs [93].

## A.8. Formulas for estimating yearly OPEX

| Parameter  | Description  | Formula  | Unit     |
|------------|--|--|----------|
| Rm OPEX    | Annual raw material cost   | Flow rate raw material × price raw material                          | USD/year |
| E OPEX     | Annual electricity cost (for electrolyser)   | Electrolyser power × electricity price                               | USD/year |
| FC OPEX    | Annual fixed costs (e.g., maintenance, labour, taxes, and insurance, factory and head office overhead) | FC OPEX = FC factor × CAPEX  | USD/year |
| OPEX C     | Annual cost of consumables (e.g., catalysts, chemicals)  | Consumables rate × price per unit                                    | USD/year |
| IR Salvage | Annual value loss of the equipment   | IR = declining balance depreciation factor × CAPEX (with DBD = 0.02) | USD/year |
| DBD        | Declining balance depreciation   | $DBD = 1 - \left( \frac{IR}{CAPEX - IR} \right)^{\frac{1}{n}}$       | [-]      |
| $A_i$      | Year i annual provision for depreciation   | $A_i = (CAPEX - IR) \times (1 - DBD)^{i-1} \times DBD$               | USD/year |
| A          | Average annual provision for depreciation  | $A = Average(A_i)$   | USD/year |
| $i_m$      | Yearly average rate of return if the money was not invested in plant                                   | $i_m = \frac{Interest\ rate \times (n+1)}{2 \times 100 \times n}$    | [-]      |
| IC OPEX    | Investment cost per year   | $IC\ OPEX = \frac{CAPEX}{\sum_{i=1}^n A_i + CAPEX} \times i_m$       | USD/year |
| OPEXi      | Year i operating expenditure   | $OPEXi = RmOPEX + EOPEX + UOPEX + CmOPEX + FCOPEX + A_i + ICOPEX$    | USD/year |
| OPEX       | Average lifetime operating expenditure   | $OPEX = Average(OPEXi)$  | USD/year |

Table A.19: Operational Expenditure (OPEX) Parameters.

# B

## Appendix results

This chapter provides additional information and data visualisations for the results section.

### B.1. pH steps required for the cases

| Case                         | Condition | pH Range   |
|------------------------------|-----------|------------|
| <b>Case 1: 90 wt%</b>        | Worst     | 9,0 ↔ 11,5 |
|                              | Base      | 9,0 ↔ 11,5 |
|                              | Best      | 9,0 ↔ 11,5 |
| <b>Case 2: FT Process</b>    | Worst     | 8,5 ↔ 11,2 |
|                              | Base      | 8,5 ↔ 11,3 |
|                              | Best      | 8,5 ↔ 11,4 |
| <b>Case 3: High FE</b>       | Worst     | 8,5 ↔ 9,1  |
|                              | Base      | 8,5 ↔ 9,3  |
|                              | Best      | 8,5 ↔ 9,5  |
| <b>Case 4: Energiron III</b> | Worst     | 8,5 ↔ 11,0 |
|                              | Base      | 8,5 ↔ 11,6 |
|                              | Best      | 8,5 ↔ 12,0 |
| <b>Case 5: Mid pH</b>        | Worst     | 9,0 ↔ 10,5 |
|                              | Base      | 9,0 ↔ 10,5 |
|                              | Best      | 9,0 ↔ 10,5 |

**Table B.1:** Overview of pH Ranges for Different Cases (Rounded to 1 Decimal Place).

## B.2. Literature data for competing compounds and production methods

| Compound        | Production Method          | Production Cost (\$/kg) | LHV (MJ/kg) | LCOS (\$/MJ) | Reference |
|-----------------|----------------------------|-------------------------|-------------|--------------|-----------|
| CH <sub>4</sub> | Natural gas                | 0,50                    | 50,0        | 0,02         | [110]     |
|                 | Biomass                    | 1,50                    | 50,0        | 0,03         | [110]     |
|                 | Power to gas               | 7,00                    | 50,0        | 0,14         | [111]     |
| LNG             | Natural gas                | 1,00                    | 48,0        | 0,02         | [120]     |
| Syngas (2,5:1)  | rWGS                       | 1,09                    | 23,7        | 0,05         | [93]      |
|                 | Gas-fed CO <sub>2</sub> RR | 1,30                    | 23,7        | 0,05         | [93]      |
|                 | Bicarbonate electrolysis   | 1,92                    | 23,7        | 0,08         | [93]      |
| H <sub>2</sub>  | SMR without CCS            | 1,50                    | 119,6       | 0,01         | [112]     |
|                 | SMR with CCS               | 2,50                    | 119,6       | 0,02         | [112]     |
|                 | Electrolysis (renewable)   | 5,50                    | 119,6       | 0,05         | [112]     |
|                 | Electrolysis (grid)        | 6,50                    | 119,6       | 0,05         | [112]     |
|                 | Biomass                    | 3,50                    | 119,6       | 0,03         | [112]     |

**Table B.2:** Production costs and LCOS adjusted for LHV for various compounds and production methods.

## B.3. Additional LCOS analysis

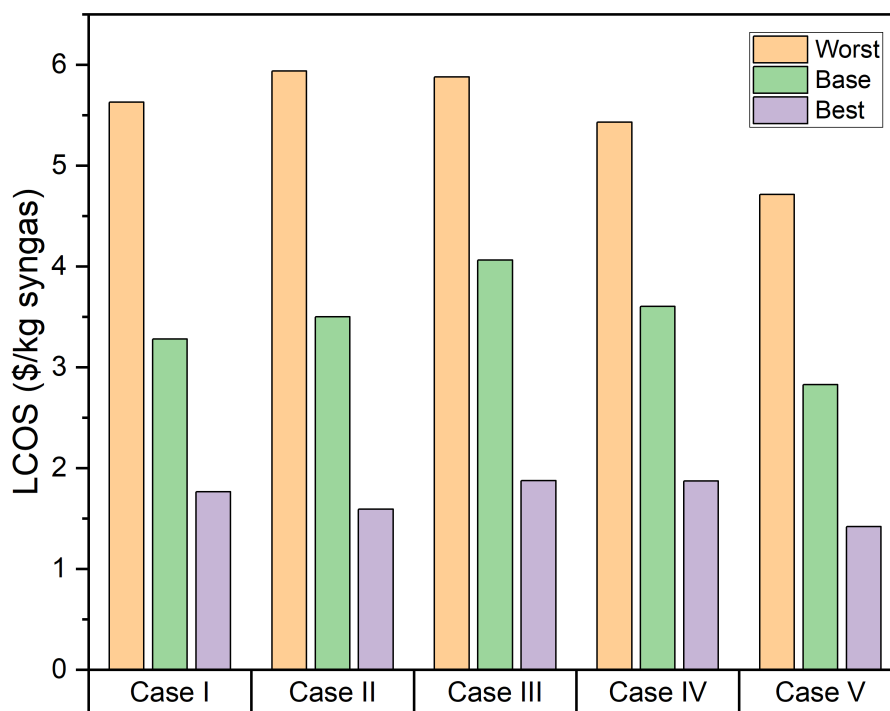


**Figure B.1:** LCOS for syngas (non-levelized for LHV).

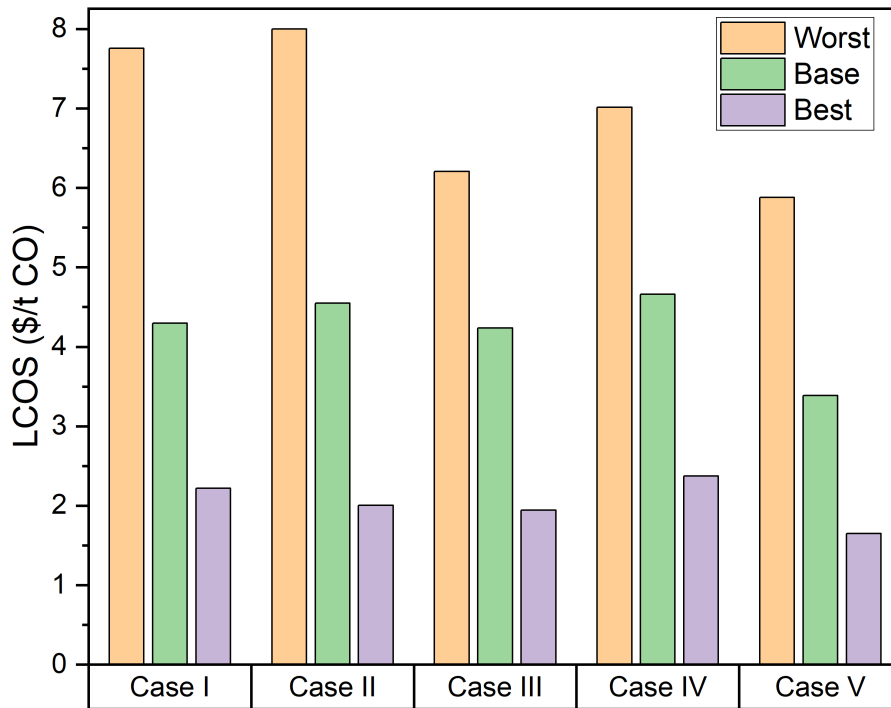


Figure B.2: OPEX per kg CO product

B.4. Sankey plots Case I and IV

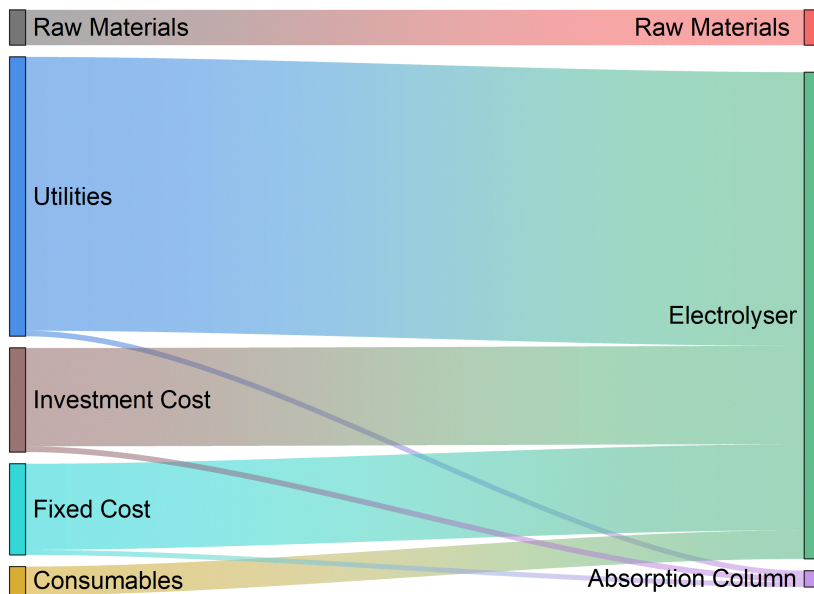
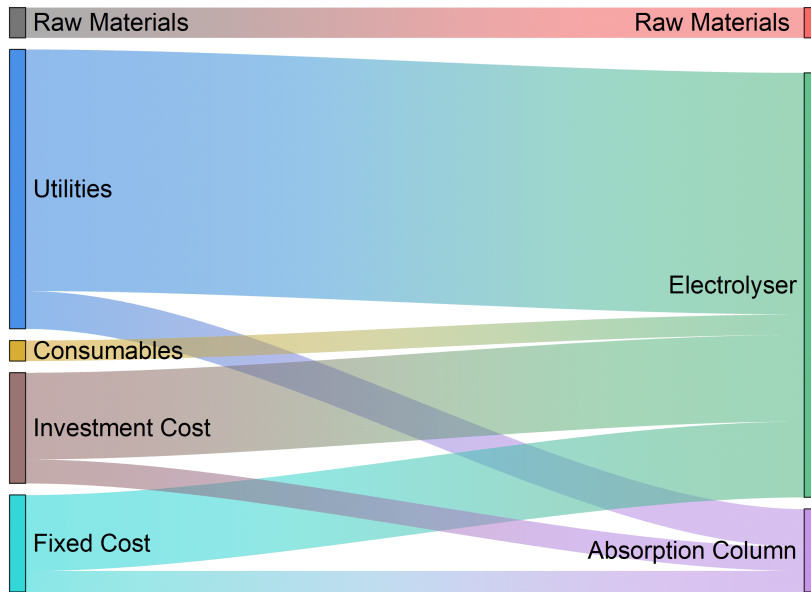
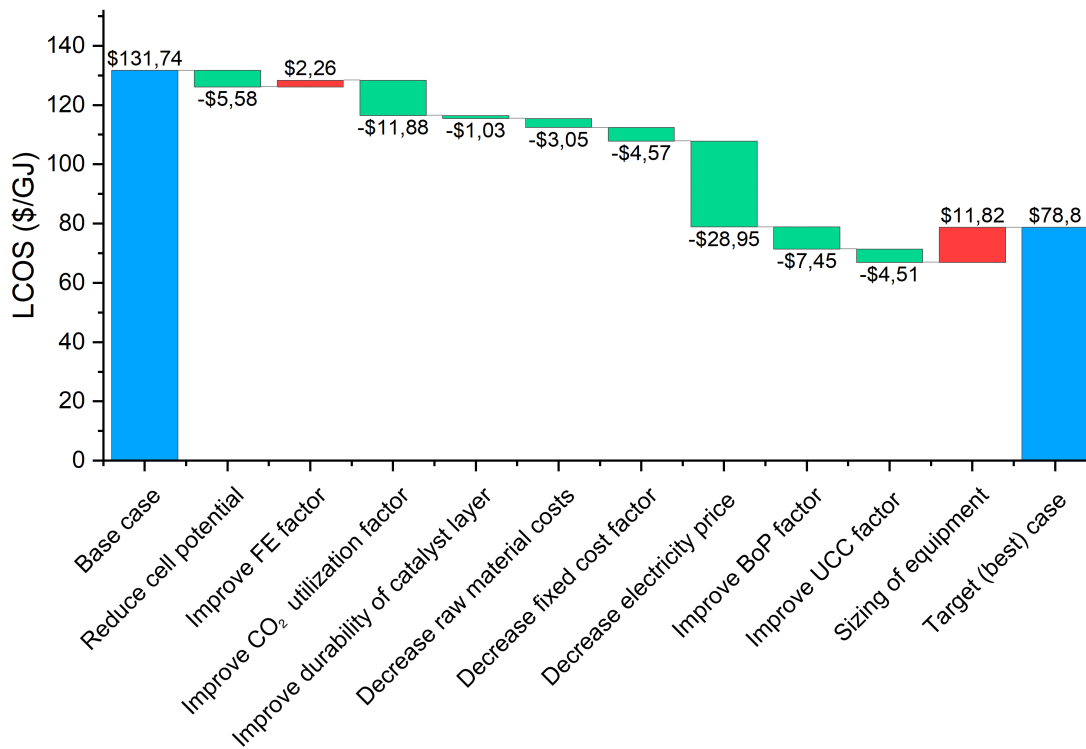


Figure B.3: Sankey diagram showing OPEX distribution for Case I (Base Scenario): pH step 9.0 ↔ 11.5. Total OPEX: \$18,8 million/year.



**Figure B.4:** Sankey diagram showing OPEX distribution for Case IV (Base Scenario): pH step 8.5 ↔ 11.5. Total OPEX: \$21,4 million/year.

### B.5. Brigdeplots Case I, III, IV and V



**Figure B.5:** Bridge plot showing LCOS<sub>LHV</sub> for case I (base → best).

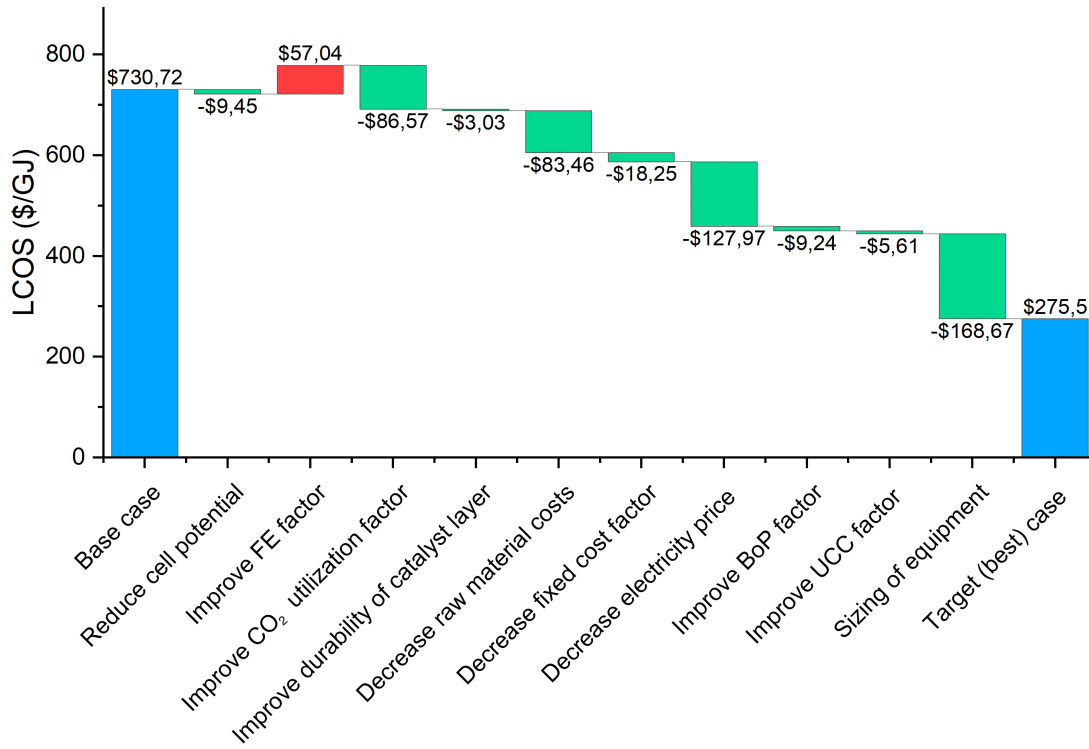


Figure B.6: Bridge plot showing  $LCOS_{LHV}$  for case III (base → best).

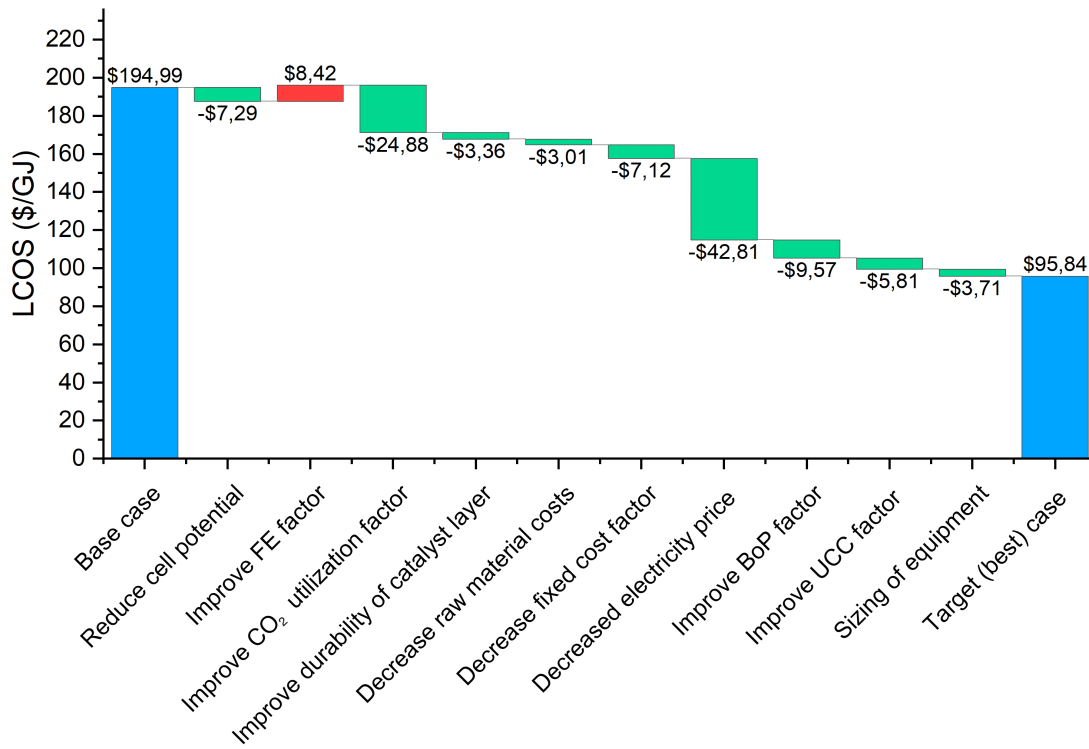


Figure B.7: Bridge plot showing  $LCOS_{LHV}$  for case IV (base → best).

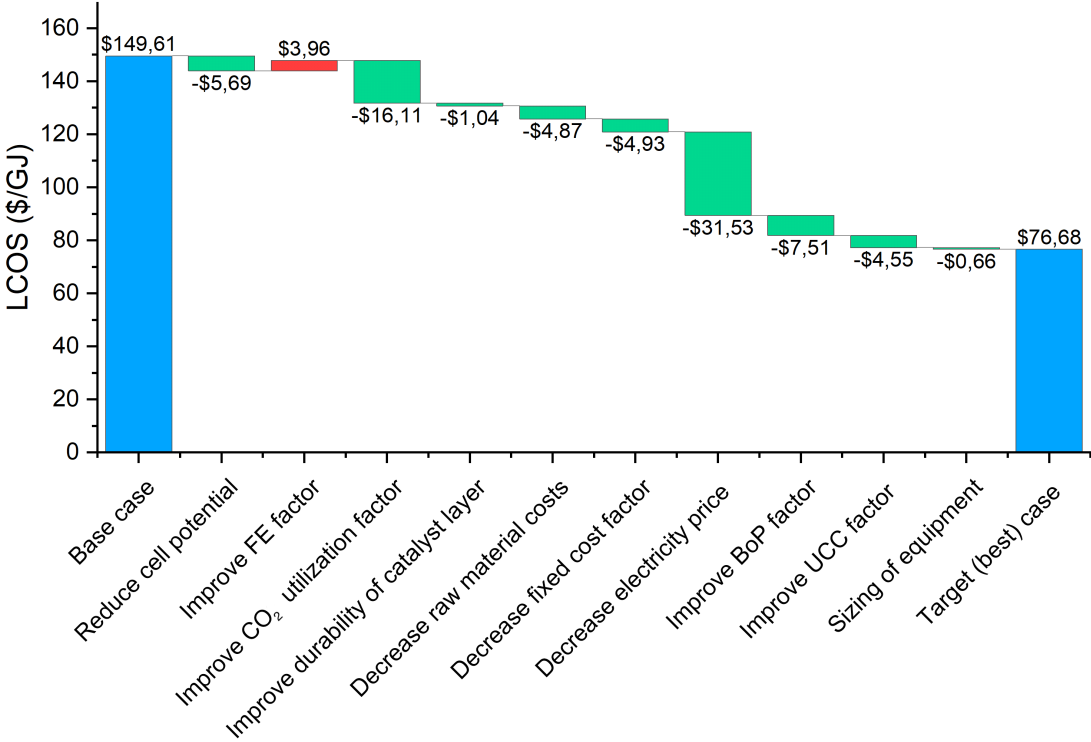


Figure B.8: Bridge plot showing LCOS<sub>LHV</sub> for case V (base → best).

### B.6. OPEX per kg CO<sub>2</sub> for 50%/50% solar wind mix

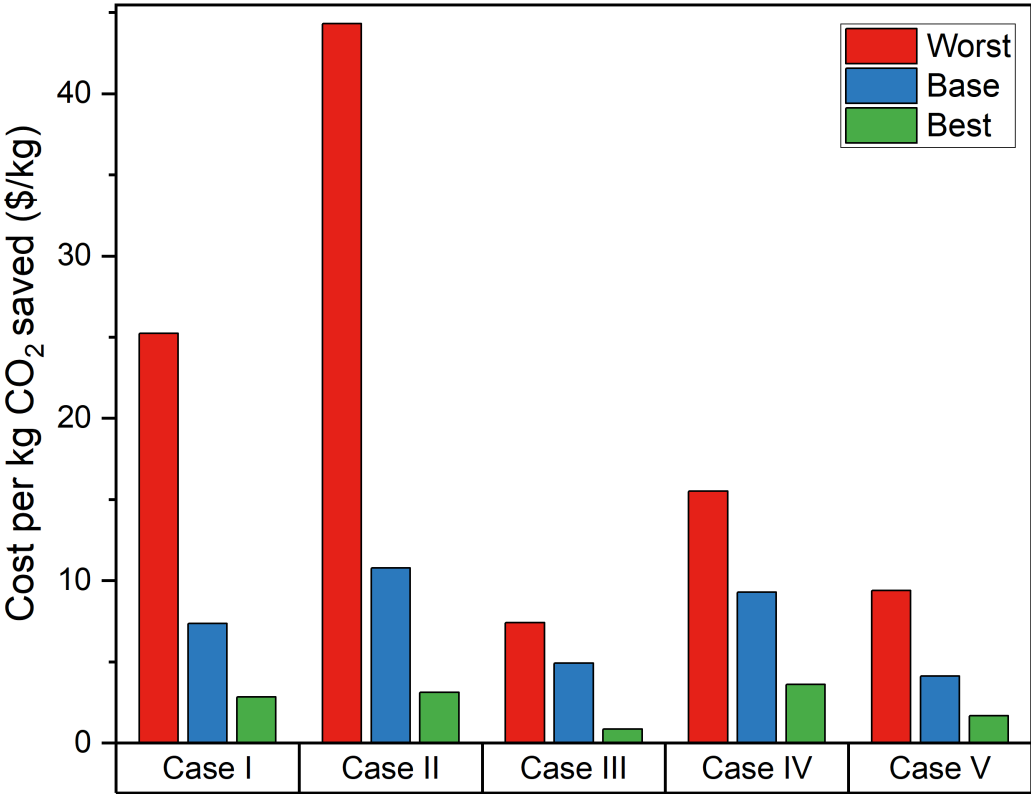


Figure B.9: OPEX per kg CO<sub>2</sub> not emitted (energy source: 50%/50% wind solar mix).

### B.7. CAPEX per t CO produced

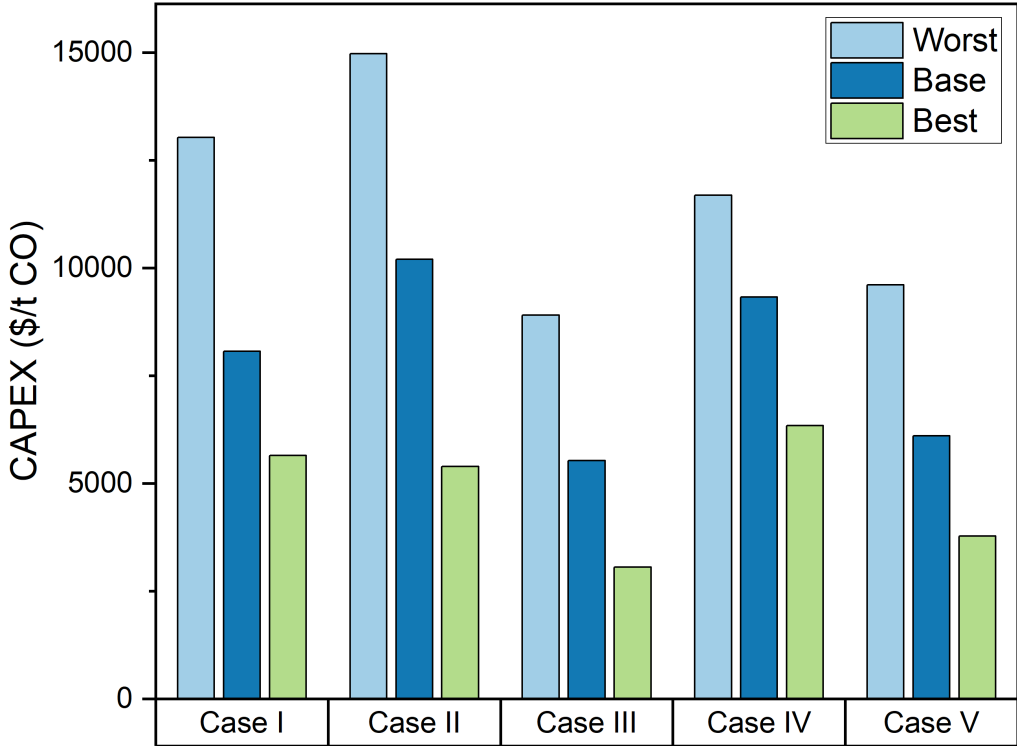


Figure B.10: CAPEX per ton of CO product per year for the five cases.

### B.8. CAPEX distribution among equipment

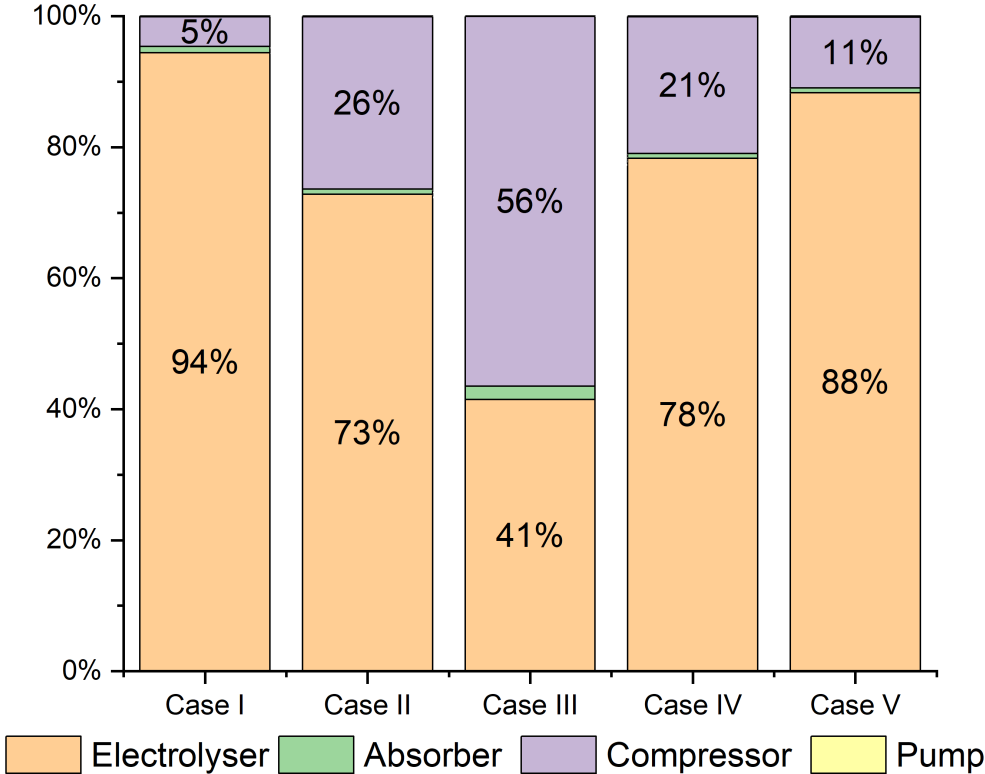
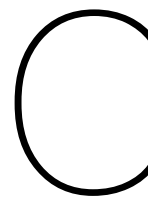


Figure B.11: CAPEX distribution among equipment presented as a 100% stacked bar chart for the base case scenario. The fraction of CAPEX allocated to the pump is negligible.



# Python code

## C.1. Python code for Bjerrum plot

Listing C.1: Python code for Bjerrum calculations and mole fractions at specified pH values.

```
1 # Define constants for the second set of pKa values
2 K1_alt = 10**-5.85 # Alternative pKa1 value
3 K2_alt = 10**-9.85 # Alternative pKa2 value
4
5 # pH range
6 pH = np.linspace(0, 14, 100)
7
8 # Functions to calculate the species concentrations
9 def carbonate_species(pH, K1, K2):
10     H = 10**-pH
11     CO2 = 1 / (1 + K1/H + (K1*K2)/(H**2))
12     HCO3 = (K1/H) / (1 + K1/H + (K1*K2)/(H**2))
13     CO3 = (K1*K2)/(H**2) / (1 + K1/H + (K1*K2)/(H**2))
14     return CO2, HCO3, CO3
15
16 # Carbonate system plot for the first set of pKa values
17 CO2, HCO3, CO3 = carbonate_species(pH, K1, K2)
18 plt.figure(figsize=(10, 6))
19 plt.plot(pH, CO2, label='$CO_2$ (1 bar, 20°C)', linewidth=2)
20 plt.plot(pH, HCO3, label='$HCO_3^-$ (1 bar, 20°C)', linewidth=2)
21 plt.plot(pH, CO3, label='$CO_3^{2-}$ (1 bar, 20°C)', linewidth=2)
22 plt.axvline(x=-np.log10(K1), color='grey', linestyle='--')
23 plt.axvline(x=-np.log10(K2), color='grey', linestyle='--')
24 plt.text(-np.log10(K1), 0.8, 'pK1', rotation=90, verticalalignment='center')
25 plt.text(-np.log10(K2), 0.8, 'pK2', rotation=90, verticalalignment='center')
26
27 # Carbonate system plot for the second set of pKa values
28 CO2_alt, HCO3_alt, CO3_alt = carbonate_species(pH, K1_alt, K2_alt)
29 plt.plot(pH, CO2_alt, label='$CO_2$ (10 bar, 60°C)', linestyle='--', linewidth=2)
30 plt.plot(pH, HCO3_alt, label='$HCO_3^-$ (10 bar, 60°C)', linestyle='--', linewidth=2)
31 plt.plot(pH, CO3_alt, label='$CO_3^{2-}$ (10 bar, 60°C)', linestyle='--', linewidth=2)
32 plt.axvline(x=-np.log10(K1_alt), color='grey', linestyle=':')
33 plt.axvline(x=-np.log10(K2_alt), color='grey', linestyle=':')
34 plt.text(-np.log10(K1_alt), 0.7, 'pK1_alt', rotation=90, verticalalignment='center')
35 plt.text(-np.log10(K2_alt), 0.7, 'pK2_alt', rotation=90, verticalalignment='center')
36
37 plt.xlabel('pH')
38 plt.ylabel('Concentration')
39 plt.title('DIC speciation')
40 plt.legend(loc='best')
41 plt.show()
42
43 # Readout of the mole fractions at specified pH values
44 specified_pH = [8.5, 9, 9.5, 10, 10.5, 11, 11.3, 11.5]
45 print("Carbonate system mole fractions at specified pH values (original pKa):")
46 for pH_value in specified_pH:
```

```
47     CO2, HCO3, CO3 = carbonate_species(pH_value, K1, K2)
48     print(f"At pH_{pH_value}: CO2={CO2:.4f}, HCO3-={HCO3:.4f}, CO3^2-={CO3:.4f}")
49
50 print("\nCarbonate system mole fractions at specified pH values (alternative pKa):")
51 for pH_value in specified_pH:
52     CO2_alt, HCO3_alt, CO3_alt = carbonate_species(pH_value, K1_alt, K2_alt)
53     print(f"At pH_{pH_value}: CO2={CO2_alt:.4f}, HCO3-={HCO3_alt:.4f}, CO3^2-={CO3_alt:.4f}")
```